Computer aided design of stable and efficient OLEDs

Dissertation

zur Erlangung des Grades

”Doktor der Naturwissenschaften”

im Promotionsfach Chemie

am Fachbereich (09) Chemie, Pharmazie und Geowissenschaften

der Johannes-Gutenberg-Universität Mainz

Leanne Paterson

geb. in Rutherglen, Glasgow, Scotland

Max Planck Institute for Polymer Research

Mainz, 25 April 2021

Erstgutachter:

Prof. Dr. Kurt Kremer

Max-Planck-Institut für Polymerforschung Mainz

Zweitgutachter:

Prof. Dr. Gregor Diezemann

Johannes-Gutenberg-Universität Mainz

Einreichungsdatum Doktorarbeit: Februar 2021

Datum der mündlichen Prüfung: 12th April 2021

Leanne Paterson

PhD Thesis: Computer aided design of stable and efficient OLEDs
Submitted to the Department of Chemistry of Johannes-Gutenberg-Universität Mainz
Work carried out in the Theory group at the Max-Planck Institute for Polymer Research, Mainz

Statutory declaration

"I hereby declare that I wrote the dissertation submitted without any unauthorized external assistance and used only sources acknowledged in the work. All textual passages which are appropriated verbatim or paraphrased from published and unpublished texts as well as all information obtained from oral sources are duly indicated and listed in accordance with bibliographical rules. In carrying out this research, I complied with the rules of standard scientific practice as formulated in the statutes of Johannes Gutenberg-University Mainz to insure standard scientific practice."

Leanne Paterson

Mainz, 25 April 2021

Acknowledgments

I would firstly like to thank Prof. Kurt Kremer for supervising my PhD work and for giving me the opportunity to join the theory group at the Max-Planck Institute for Polymer Research (MPIP), in Mainz. It has been a privilege to be part of such an extraordinary team and I have gained invaluable experience, both scientific and personal. With that, a special thanks goes to the members of the theory group, all of whom I have had the pleasure of meeting and getting to know. I am particularly happy to have had the chance to share an office with Dr. Joseph Rudzinski, Dr. Nancy Forero-Martinez, and Benjamin Pampel, and for our friendly discussions over the last few years. I would also like to take this chance to thank Doris Kirsch and Irene Thelo-Becker for all of their help during my time at the MPIP.

My sincere gratitude goes to my direct supervisor Dr. Denis Andrienko, for all of the advice and guidance throughout my PhD. I am truly grateful, as having a friendly and supportive supervisor makes even the most challenging tasks possible. I appreciate all of our discussions and the continued encouragement, which were crucial in helping me to develop new skills and carry out various research projects. I have enjoyed my time in the organic electronics simulations group and I would like to thank all of the group members, past and present. From the various conferences we attended, to our group meetings and occasional dinner, it has been wonderful to get to know everyone and I will always treasure my time in the group.

Additionally, thank you to Prof. Gregor Diezemann, as my secondary supervisor from the chemistry department of Johannes-Gutenberg-Universität Mainz. I would also like to thank Dr. Christoph Scherer for helping with the German translation of my thesis abstract. Also, many thanks to Dr. Falk May from Merck KGaA Darmstadt, for the helpful discussions and advice for our publications, from the industrial perspective.

Finally, I would like to include some personal acknowledgments, as I would not be where I am today without the love, support and encouragement of my family. Firstly, my greatest thanks is to my mum and dad for always encouraging me to do my best, their confidence in me meant that nothing was ever too ambitious, even my dream to be a scientist, since the age of five. Thank you to my grandma, for always believing in me, including the gift of my first chemistry set many years ago. I would also like to thank my sister, Arlene, for supporting me and always being there. Many thanks to all of my family back home in Scotland. A heartfelt thanks also goes to my partner Alex, who helped make this possible, and I will always be grateful to the family I now have in Germany.

With my most sincere appreciation, thank you!

Abstract

Organic light emitting diodes (OLEDs) are carbon-based compounds with structures designed for photo- or electro-luminescence, creating a unique alternative to traditional display technologies. Tailored device architecture can offer properties such as flexibility and transparency, presenting unparalleled application possibilities. Therefore, the commercial advancement of OLEDs is highly anticipated, and continued research is vital for improving device efficiency and lifetime. The performance of an OLED relies on an intricate balance between stability, efficiency, operational driving voltage, and colour coordinate, with the aim of optimising these parameters by employing appropriate material design. Multiscale simulation techniques can aid with the rational design of these materials, in order to overcome existing shortcomings. For example, extensive research has focused on the emissive layer and the obstacles surrounding blue OLEDs, in particular, the trade-off between stability and efficiency, while preserving blue emission. To this aim, the novel concept of unicoloured phosphor-sensitised fluorescence (UPSF) has demonstrated the ability to overcome these limitations, by achieving a stable and efficient blue OLED. In order to quantify the potential of such a novel approach and OLED design, computational input is an essential component, making it possible to gain a better fundamental understanding, while highlighting key areas for further device improvements. More generally, due to the vast number of contending organic materials and with experimental pre-screening being notoriously time-consuming, a complementary *in-silico* approach can be considerably beneficial. The ultimate goal of OLED simulations is the prediction of device properties from chemical composition, prior to synthesis. However, various challenges must be overcome to bring this to a realisation. Computer aided design is becoming an essential component for future OLED developments, and with the field shifting towards machine learning based approaches, *in-silico* pre-screening is the future of material design.[*]

[*]Adapted and reprinted from,[1] Computer Aided Design of Stable and Efficient OLEDs; Paterson, L.; May, F.; Andrienko, D.; J. Appl. Phys. 2020, 128 (16), 160901. doi: 10.1063/5.0022870.1 with the permission of AIP Publishing

Zusammenfassung

Organische Leuchtdioden (OLEDs) sind Verbindungen auf Kohlenstoffbasis mit Strukturen, die für die Photo- oder Elektrolumineszenz ausgelegt sind und eine einzigartige Alternative zu herkömmlichen Anzeigetechnologien darstellen. Eine maßgeschneiderte Gerätearchitektur bietet Eigenschaften wie Flexibilität und Transparenz und bietet beispiellose Anwendungsmöglichkeiten. Daher wird die kommerzielle Weiterentwicklung von OLEDs mit Spannung erwartet, und kontinuierliche Forschung ist für die Verbesserung der Geräteeffizienz und -lebensdauer von entscheidender Bedeutung. Die Leistung einer OLED beruht auf einem komplexen Gleichgewicht zwischen Stabilität, Effizienz, Betriebsspannung und Farbkoordinate, mit dem Ziel diese Parameter durch ein geeignetes Materialdesign zu optimieren. Multiskalensimulationstechniken können beim rationalen Design dieser Materialien helfen, um vorhandene Unzulänglichkeiten zu überwinden. Zum Beispiel haben sich umfangreiche Forschungen auf die Emissionsschicht und die Hindernisse rund um blaue OLEDs konzentriert, wie insbesondere der Kompromiss zwischen Stabilität und Effizienz unter Beibehaltung der blauen Emission. Zu diesem Zweck hat das neuartige Konzept der einfarbigen phosphorsensibilisierten Fluoreszenz (UPSF) die Fähigkeit gezeigt, diese Einschränkungen zu überwinden, um eine stabile und effiziente blaue OLED zu erreichen. Um das Potenzial eines solchen neuartigen Ansatzes und OLED-Designs zu quantifizieren, ist die rechnergestützte Modellierung eine wesentliche Komponente, die ein besseres grundlegendes Verständnis ermöglicht und gleichzeitig Schlüsselbereiche für weitere Geräteverbesserungen hervorhebt. Allgemein kann ein komplementärer *In-Silico*-Ansatz aufgrund der großen Anzahl konkurrierender organischer Materialien und des bekanntermaßen zeitaufwändigen experimentellen Vorscreenings erheblich vorteilhaft sein. Das letztendliche Ziel von OLED Computersimulationen ist die Vorhersage der Geräteeigenschaften anhand der chemischen Zusammensetzung bereits vor der Synthese. Um dies zu verwirklichen, müssen jedoch verschiedene Herausforderungen bewältigt werden. Computergestütztes Design wird zu einem der wesentlichen Bestandteile der zukünftigen OLED-Entwicklung werden. Angesichts der Verlagerung des Feldes hin zu Ansätzen des maschinellen Lernens ist das *In-Silico*-Vorscreening die Zukunft des Materialdesigns.

Associated Publications

[1]. Leanne Paterson, Anirban Mondal, Paul Heimel, Robert Lovrincic, Falk May, Christian Lennartz, and Denis Andrienko;
Perspectives of Unicolored Phosphor-Sensitized Fluorescence;
Advanced Electronic Materials, 5, 1900646 (2019);
DOI: 10.1002/aelm.201900646

[2]. Leanne Paterson, Falk May, and Denis Andrienko;
Computer aided design of stable and efficient OLEDs;
Journal of Applied Physics 128, 160901 (2020);
DOI: 10.1063/5.0022870
Reprinted with the permission of AIP Publishing

[3]. Andrei Stankevych, Alexander Vakhnin, Denis Andrienko, Leanne Paterson, Ivan I. Fishchuk, Heinz Bässler, Anna Köhler, and Andrey Kadashchuk;
Density of States of OLED Hosts from Thermally Stimulated Luminescence;
Submitted to Physical Review Applied (2020)

[4]. Anirban Mondal*, Leanne Paterson*, Jaeyoung Cho, Kun-Han Lin, Bas van der Zee, Gert-Jan A. H. Wetzelaer, Andrei Stankevych, Alexander Vakhnin, Jang-Joo Kim, Andrey Kadashchuk, Paul W. M. Blom, Falk May, and Denis Andrienko;
*these authors contributed equally to the work
Physical properties of OLED host materials;
Submitted to Chemical Physics Reviews (2021)

Contents

1 What is an OLED?

A cornerstone of modern technology is the advancement of electronic devices and their applications; relying on everyday functionality, reliability, and efficiency. As they are advancing at an unprecedented rate, it is imperative that the technology behind them follows the same trend. Electronic devices are not solely restricted to metallic conductivity, with organic electronics gaining momentum in recent years. As the name would suggest, these devices make use of organic materials: carbon-based polymers or small molecule systems with the desirable semi-conductive properties. The conjugated molecular structure consists of a hydrocarbon framework, often containing heteroatoms such as oxygen and nitrogen. The umbrella of organic electronics includes devices such as organic light emitting diodes (OLED), organic field effect transistors (OFET) and organic solar cells.

1.1 Organic Semiconductor properties

There are two distinct classes of organic semiconductors: small molecular weight materials, and polymers. The properties for both are largely similar, including their conjugated π-electrons and charge carrier transport abilities.

1.1.1 π orbitals

The neighbouring sp^2 hybridised carbon atoms in these molecules form a hybrid bond, known as the σ bond, which is formed by the p_x and p_y orbitals, making up the backbone of the molecule. While a π bond is formed by the overlap of p_z orbitals of neighbouring carbons, as shown in Figure 1.1, for a simple π conjugated system.

The π bond is significantly weaker than the σ bond, meaning that the electrons are more delocalised. The result of this, is that electrons occupying the shared delocalised π orbitals can move between neighbouring orbitals, effectively moving from one bond to the next.[2] In polymer systems, the intramolecular movement of electrons is vital. While in small molecule

systems, it is the intermolecular electron hopping between different molecules, here, the overlap of π orbitals between neighbouring molecules makes electron transport possible.

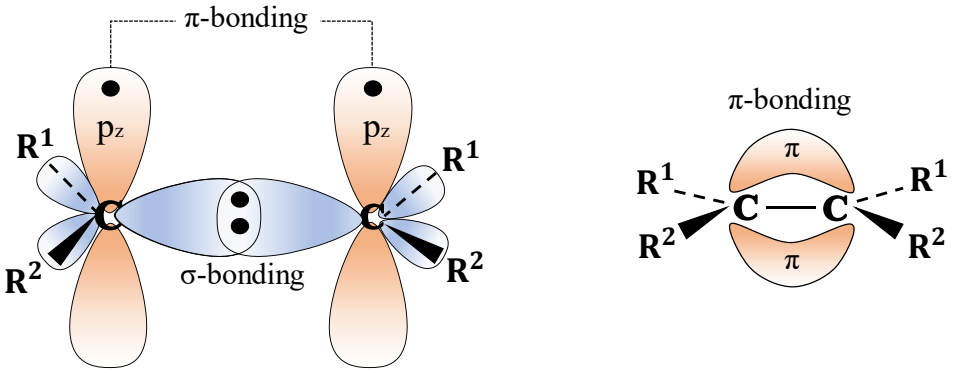

Figure 1.1 Simple π conjugated system: the central carbon atoms with sp^2 hybridised orbitals (blue) and the p_z orbital (orange), show the σ and π bonds (left). The p_z orbitals of neighbouring carbons overlap to form the π bonds resulting in electrons delocalising over the bond (right).

1.1.2 Charge transport

Inorganic semiconductor crystals, such as silicon, with highly delocalised electronic states due to strong covalent bonding, have strong electronic interactions between the atomic orbitals. As a result, band-like transport of the charge carriers occurs, with high transport mobility. On the other hand, in amorphous organic semiconductors, the weak van der Waals intermolecular interactions and localised energy states, result in a 'hopping' transport from one molecule to another. The weak electronic coupling associated with this transport is due to the small π orbital overlap between neighbouring molecules, electrons are thus highly localised on one molecule and the transport between molecular sites is described by a series of hops. The hopping mechanism is thermally-activated and can be described in terms of the energetic landscape, polaronic effects and electronic coupling elements, by the Marcus rate equation, discussed in depth in Chapter 2.3 for Charge Transport simulations.

1.1.3 Luminescent properties

One of the pivotal discoveries in the field was the electroluminescence of certain organic materials in 1953.[3–5] Which in turn brought about the fabrication of the first OLED in 1987.[6]

As a sub-category of organic semiconductors, OLEDs are carbon-based compounds with structures tailored for photo- or electro-luminescence. The luminescent properties arise from electronic excitations, followed by relaxation and photon emission.

When in the ground state, the bonding orbitals in the molecule are occupied by electron pairs with antiparallel spin, up to and including the highest occupied molecular orbital (HOMO). An excited state is formed when an electron is promoted from the HUMO to the lowest unoccupied molecular orbital (LUMO), by absorbing energy. Additionally, as the HOMO is defined as the delocalised π orbital, while the antibonding π* orbital is the LUMO, electron transfer occurs between the LUMO levels. When an electron is excited to a higher energy level, the spin of the electron can have the same orientation as it had in the ground state, maintaining the antiparallel arrangement, known as a singlet excited state. Or it can change its spin orientation, to become parallel to the other unpaired electron, known as a triplet state. The electronic configurations for each spin state are shown in Figure 1.2.

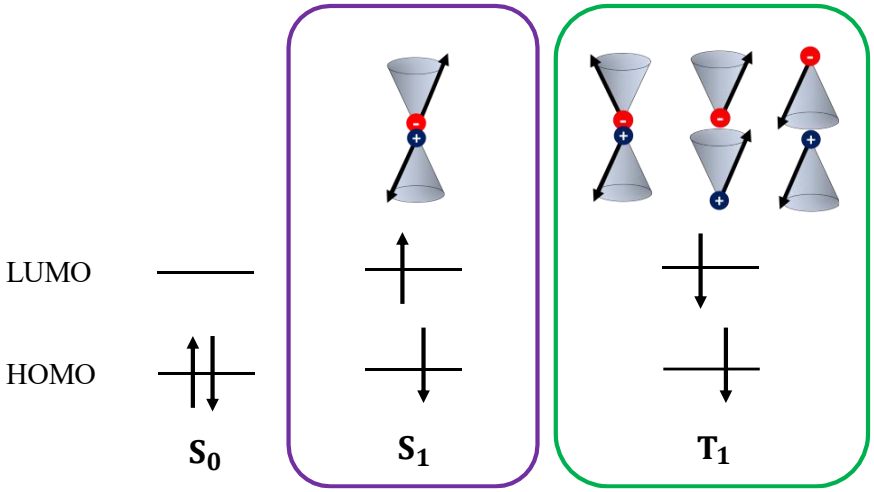

Figure 1.2 Electronic configuration for the ground state (S_0), the first singlet excited state (S_1) and the first triplet excited state (T_1). The arrows represent the electron spin.[1]

Localised energy states, resulting in well-defined singlet and triplet spin states within the organic semiconductor, aid with the luminescent properties.[7] The excitation of the molecule involves the promotion of an electron from the singlet ground state (S_0) to the first excited singlet state (S_1), or the first triplet excited state (T_1) if there is strong spin-orbit coupling.

Excitation occurs with a 25% probability to the S_1 state, as there is only one possible configuration (maintaining antiparallel spin), or a 75% probability to the T_1 state, with three potential parallel spin combinations. Choosing specific emitters, where emission is only possible from the decay S_1 to S_0, results in rapid (~ns) radiative decay, known as fluorescent emission. Here, the triplet excited state decays non-radiatively, resulting in a 75% efficiency loss. On the other hand, when radiative decay is only possible from the T_1 to S_0 transition, the result is slow (~µs) phosphorescent emission. In this case an intersystem crossing mechanism, involving a (spin-flip) transition from the S_1 to T_1 state is possible, followed by phosphorescent emission, such that all excitations can be efficiently utilised. For phosphorescent emission to be possible, organo-metallic complexes, containing heavy metals such as Iridium (Ir), are used. The inclusion of this heavy metal atom allows for spin-orbit coupling, resulting in easier electron spin flipping when moving from the S_1 to T_1 state, which would otherwise be a forbidden transition.

1.2 Small Molecules vs. Polymers

The luminescent characteristic of OLEDs can be brought to fruition by effectively utilising a thin layer(s) of a polymeric or small molecule based organic material(s), to achieve a desirable wavelength of emission. The choice between small molecules and polymers largely depends on the application and the method of device fabrication.

The conventional small molecule OLED (SM-OLED) has a multilayer device structure, as shown in Figure 1.3. This complex design achieves an overall high stability and efficiency, due to each layer's tailored functionality. A single layer is typically comprised of one or more type(s) of molecule, for a designated task, e.g., a specific type of emitter for the emissive layer. A polymer OLED (PLED), on the other hand, has a simpler device structure, owed to the fact that PLEDs can incorporate various functions into one molecule by polymerisation. PLEDs can have various functional units within one polymer, matching the functions of a multilayer SM-OLED, such as an electron transporting unit, hole transporting unit and the emitter unit. Similarly, the various emission colours can be controlled and subsequently adjusted with the use of specific monomer units. However, this simplistic device design comes at a cost, and as such, PLEDs typically have reduced performance, in terms of efficiency and stability.

1.2.1 Device fabrication

A significant difference between SM-OLEDs and PLEDs is their processability. SM-OLEDs are typically processed by vacuum deposition, with molecules deposited onto a solid surface, while PLEDs are solution processible and can be utilised in an inkjet style printing process.

Currently, commercial OLED displays are largely manufactured by vacuum thermal evaporation,[8] also known as vacuum deposition. Although this is an expensive production method, it ensures a high degree of purity and controlled fabrication,[9] which in turn results in a higher efficiency and longer lifetime of the OLED device. Vacuum deposition involves evaporating and condensing the material onto a solid substrate, layer by layer. The advantage of this is that multilayer fabrication, including the layer thickness, can be easily controlled. The major disadvantage is the high fabrication cost and potential inefficient use of materials, due to the use of mask patterning. Additionally, the scalability of vacuum deposition is difficult, especially for the fabrication of large-area displays.

On the other hand, solution processed films using polymeric OLED materials, do have a lower cost of fabrication and increased scalability for large-area displays. Unfortunately, solution processible methods, allow for increased opportunities of contamination by water or oxygen, for example, which can have a detrimental effect on the OLED performance.[8,10] Single layer PLEDs[11] between two electrodes have been shown to have low efficiency and low stability, due to low charge-carrier mobilities and high charge-injection barriers. When considering the fabrication of a multilayer PLED, the main obstacle is with achieving distinct layers. Solution-based methods, such as spin coating introduces the problem of partial or total dissolving of the lower layer upon application of the next. To address this, research efforts have involved the development of solution-based methods to achieve multilayer polymer devices, by utilising a cross-linking process between each layer deposition.[12–14] By establishing layers insoluble to one another, a multi-layer structure is achievable, allowing for charge transport and block layers to potentially increase device efficiency. However, as PLEDs continue to have limited device lifetime, ongoing research efforts are required to make them commercially viable in the long term.

Furthermore, there exists a sub-class of SM-OLEDs, the solution processible small molecules. Recently drawing more and more attention, as they combine the advantage of small molecule properties and low-cost processability.[15] Although the solution processible SM-OLEDs offer a

promising alternative to the traditional SM-OLEDs, they face similar challenges to PLEDs, namely low efficiency and difficulty achieving a multi-layered structure. To address some of these challenges, recent research efforts have focused on chemically tailoring small molecules for balanced charge injection and transport, solubility properties and morphology.[15] Including the interest in bipolar molecules, containing both electron and hole transporting groups.[16] Similar to PLEDs, solution processible SM-OLEDs require continued research efforts to be compatible with typical SM-OLEDs. Therefore, when comparing both SM-OLEDs and PLEDs:

- For small to medium sized display applications, SM-OLEDs and the vacuum evaporation techniques they entail, are the favourable choice for high performing devices.
- For large displays, the advancement of printable SM-OLEDs and/or efficient PLEDs, is essential for competitive cost-effective mass production of OLED devices.

1.3 Multilayer OLED structure*

A typical small molecule multi-layer OLED structure sandwiched between two electrodes, is illustrated in Figure 1.3, showing each layer with the corresponding function.

Upon the application of an external potential, electrons and holes are injected from the cathode and anode, respectively. Electron and hole injection and transport layers then facilitate the movement of the charge carriers to the emissive layer, where they recombine to form excitons and consequently a photon of the desirable wavelength is emitted. A blocking layer, in combination with, or additional to the transport layer for each carrier can also be utilised, to assist in the accumulation of carriers in the emissive layer, by preventing electron transport to the anode and hole transport to the cathode.

The path of exciton formation and decay resulting in photon emission, as well as the emission colour, depends on the organic molecules and molecular packing. It is crucial to utilise the individual strengths of organic materials for their designated task. As a result, extensive

*Adapted and reprinted from,[1] Computer Aided Design of Stable and Efficient OLEDs; Paterson, L.; May, F.; Andrienko, D.; J. Appl. Phys. 2020, 128 (16), 160901. doi: 10.1063/5.0022870.1 with the permission of AIP Publishing

research efforts have focused on each of the individual layers and the organic constituents. The 'one by one' layer approach is more practical, as the chemical properties of the molecules can be tuned for specific OLED characteristics.

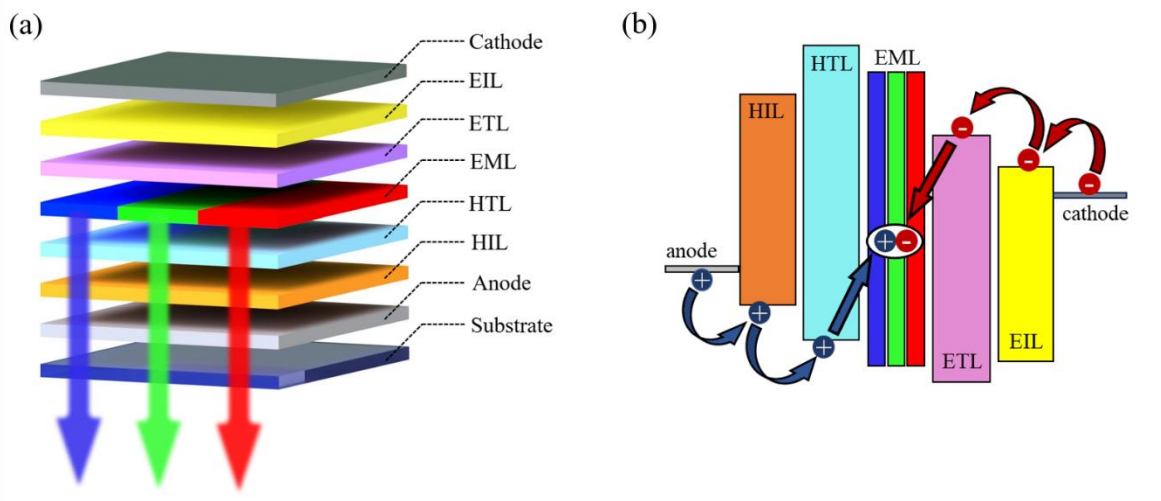

Figure 1.3 (a) Basic OLED structure and (b) schematic representation of flow of electrons and holes from electrodes to the emissive layer: electrons are injected at the cathode, to the electron injection layer (EIL) and transported via the electron transport layer (ETL), holes are injected from the anode, to the hole injection layer (HIL) and transported through the hole transport layer (HTL). Both then combine in the emissive layer (EML) to form an exciton and emit a photon of specific wavelength.[1]

The functionality of the layer, which is determined by molecular architecture, electronic properties, and charge carrier mobilities, relies on the choice of organic material. Charge transporting and emissive layers have to be designed in such a way as to maximise their function and stability. Already by utilising an electron/hole injection and transport layer, the device performance has been dramatically improved.[4,17–19] Therefore, tremendous research efforts have involved tailoring of electron injection and transport layers, hole injection and transport layers, and the various emitters for the emissive layer. Additionally, potential degradation mechanisms[20–23] and reactions within the OLED device[23] have been investigated, in order to target areas for stability improvements. All of which are necessary in the path towards high performing and long-lived OLEDs.

1.3.1 Cathode and Electron Injection layer (EIL)

The injection of electrons to the organic layers has a significant impact on the efficiency of the OLED. Lowering the energetic barrier between the cathode and the LUMO of the adjacent organic layer, facilitates the injection of electrons. However, low work function metal alloy cathodes, such as Mg:Al[24] are susceptible to atmospheric conditions.[25] Therefore, for increased stability, cathode bilayer structures, such as MgAg/Ag[26,27] and LiF/Al[25,28,29] have been frequently used. Numerous other studies have investigated n-type metal oxide semiconductors[30] and alkali metal containing interlayers.[31,32]

1.3.2 Electron Transport layer (ETL)

The electron transport layer facilitates the movement of electrons towards the emissive layer and, therefore, is a vital component of the device, confirmed by the extensive research on ETL materials.[18,33] Since balancing electron and hole injection and transport to the emissive layer is crucial for OLED performance, the challenge revolves around finding suitable and stable materials with high charge carrier mobilities. Within electron or hole transporting materials, the presence of energy traps can have a detrimental impact on the charge carrier mobilities. For large energy gap materials, this is due to the fact that either the electron affinity or ionisation energy lies in a trap region, such that unipolarity prevails. Specifically, when considering the ETL, a shallow electron affinity results in trap limited electron transport and low electron mobility. It has been shown that there is in fact an energy window, within which there lie materials for trap-free ambipolar transport, resulting in higher mobilities.[34] This is an ionisation energy below 6eV for hole transport and an electron affinity above 3.6eV, such that for appropriate material design, ideally, this energy window should be targeted.

Additionally, for optimal emission, the ETL should block holes and excitons from escaping the emissive layer. Therefore, the ETL layer should have a small injection barrier for electrons from the EIL or cathode, a HOMO level low enough to effectively block holes from the emissive layer, and a high triplet energy level for the case of triplet excitons (with high diffusion lengths). Considering one material among many various options, Alq_3 has been extensively studied for electron transport (as well as hole transport and emissive layers), spanning from the first OLED fabrication.[24] However, as it has a low triplet energy level,[35] it cannot be used with an emissive layer creating triplet excitons, unless coupled with an

interlayer. For example, the use of a hole and exciton blocking layer, such as BCP in combination with Alq_3 has been demonstrated to increase efficiency.[26,27,36,37] A further option is improving the thermal stability of materials with high electron mobility, such as BPhen, demonstrated with the use of alkali metal n-dopants.[38] Another alternative is the use of triazine based electron transporters, where substituents can be used to tune the electron mobility and LUMO energy for adjusted injection.

1.3.3 Hole injection layer (HIL)

Inserted between the typically used transparent indium-tin-oxide (ITO) anode and the hole transport layer (HTL), the hole injection layer eases hole migration at each of the interfaces. Materials for the HIL should have an ionisation energy level situated between that of the preceding and succeeding layers. This is slightly easier for hole injection, in comparison to electron injection, due to the typically lower injection barrier. Nevertheless, it has been shown that the stepwise injection from anode to HIL to HTL can improve performance; such an instance has been shown with the use of an organic interlayer,[39] such as MTDATA or 2-TNATA.[40]

1.3.4 Hole transport layer (HTL)

For a HTL to be effective, the material should fulfil certain properties. It should have good hole mobility and an appropriate HOMO level to ensure a low energetic barrier from the HIL for hole transport, and a suitable LUMO level to act as an electron blocking layer. Similar to the ETL, the HTL materials also need sufficient triplet energies to confine the exciton within the emissive layer. The most widely used HTL materials are arylamines, such as NPB, due to their high hole mobility and suitable HOMO level. However, due to its low glass transition temperature, NPB itself has low thermal stability, which can lead to device degradation. The vast research in recent years[41] has focused on finding more stable NPB derivatives or alternatives with similar or improved performance.[42–44]

1.3.5 Emissive layer (EML)

Red, green and blue emitters, are essential for full colour displays. The goal is to achieve an emission layer of each colour with high luminous properties, high efficiency, and high stability. Independent of the emission path, in order to maximize outcoupling efficiency, the transition dipole moment of the emitter should be aligned horizontally with respect to the substrate plane.[45] Here, computer simulations of the evaporation process can help in predicting how emitter-host interactions can be employed in rational compound design.[46] The various emissive paths are shown in Figure 1.4, outlining the energy levels and radiative or non-radiative decay for each type of emitter, or combinations.

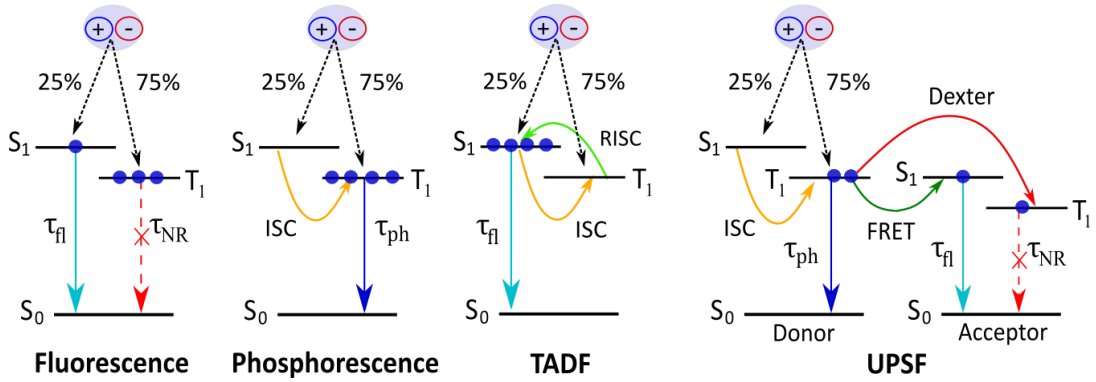

Figure 1.4 Various emissive paths: Fluorescence (fl) with 25% efficiency, only emits from the first singlet state. Phosphorescence (Ph), with intersystem crossing (ISC) allows for complete emission from the first triplet state. Thermally activated delayed fluorescence (TADF) makes use of reverse intersystem crossing (RISC) to emit from the first singlet state, more efficiently. Unicoloured phosphor-sensitised fluorescence (UPSF), with a phosphorescent donor emitting from the first triplet state and energy transfer occurring via FRET or Dexter to the singlet or triplet of a fluorescent acceptor. For UPSF, radiative decay can occur from the singlet of the acceptor but the acceptor triplet is a non-radiative (NR) decay pathway.[1]

First generation fluorescent emitting OLEDs typically have high stability but low efficiency. This is due to an unfavourable spin transition between singlet and triplet states, with rapid radiative decay (~ns) only readily occurring from the S_1 state, resulting in around a 25%

efficiency of the emitter. Increasing the overall efficiency in fluorescent emitters is possible using triplet–triplet annihilation, which is often facilitated by anthracene-based hosts.

Second generation OLEDs or phosphorescent emitters, comprised of organometallic complexes, have higher efficiency but lower stability. Here, radiative decay is possible from the T_1 state, resulting in slow (~μs) phosphorescent emission. The presence of a heavy metal atom, such as iridium or platinum, with an appropriate ligand design, results in spin–orbit coupling. This allows for the transition between S_1 and T_1 states, known as intersystem crossing (ISC), which significantly increases the efficiency. The downfall being, that these heavy metal complexes are particularly susceptible to environmental factors, which can lead to device degradation. The phosphorescent long-lived excited triplet state, typically in the order of microseconds (compared to nanoseconds of the fluorescent S_1 state), also leads to degradation, and as such, these emitters have low stability.

Third generation OLEDs that use thermally activated delayed fluorescence (TADF) emitters, harvest the triplet excitons lost in conventional fluorescent emitters by making use of a thermally activated process called reverse inter-system crossing (RISC). Choosing a sufficiently low energy gap between the T_1 and S_1 levels allows for RISC and can result in highly efficient and stable emitters.

Finally, a sensitising approach is possible, combining a donor and acceptor molecule, with the aim of overcoming the individual limitations. One such example is the use of a phosphorescent donor and a fluorescent acceptor. An application of this mechanism is discussed in Chapter 3, with a unicoloured phosphor-sensitised fluorescence (UPSF) approach, for a blue OLED. In this approach, phosphorescence occurs on the donor molecule, and energy transfer from donor to acceptor is possible via (i) short-range Dexter, followed by non-radiative decay (resulting in an efficiency loss), or (ii) long-range Förster resonance energy transfer (FRET) to achieve fluorescence from the acceptor.

In its entirety, the emissive layer consists of the chosen type(s) of emitter(s), typically dispersed within a charge transporting host material, to increase efficiency. Usually this combats adverse factors, such as triplet-triplet annihilation in phosphorescent emitters for example.

Currently there are stable and efficient red and green emitters available, with extensive research focusing on both. Due to high efficiency, phosphorescent emitters have dominated the field, in the search for red[26,36,47–51] and green.[37,52,52–55] Various charge transporting host materials have

been the subject of investigation to understand the relationship between host and device performance, targeting hosts to combat potential efficiency losses. For a similar purpose, double emissive layers have also been studied.[56,57] Additionally, red[58–60] and green[61–65] TADF emitters have been shown to be an efficient, low cost alternative to the expensive precious heavy metals found in phosphorescent emitters.

On the other hand, blue emitters are particularly problematic, due to higher triplet energy and long triplet lifetimes, leading to the lowest stability. This remains one of the largest hurdles for commercial OLED applications to date. Immense efforts have centred around finding solutions to limit device degradation in phosphorescent emitters or utilising hybrid emissive technology in an attempt to overcome it. The short operational lifetime of blue phosphorescent emitters has resulted in studies of degradation mechanisms.[66–69] Once understood, these limitations can be addressed, potentially increasing stability. Specifically, this has included targeting adverse factors such as: (1) chemical degradation,[66] (2) triplet-polaron quenching* (TPQ),[67,68,71–73] and (3) triplet-triplet annihilation† (TTA).[74–76] Additionally, simulations have been used to investigate host materials for efficient charge transport, within blue phosphorescent emitters,[77] providing a link between electronic structure and molecular packing, to the rational design of effective host materials with high charge carrier mobilities. Blue TADF emitters[78–83] and combinations of TADF with conventional fluorescent[84,85] or phosphorescent emitters,[84,86] have also been investigated. This includes the impact of emitter-host interaction[81,82] and methods of lowering the singlet-triplet energy gap,[83] potentially enhancing performance. However, at present, with triplet lifetimes similar to that of phosphorescent emitters, the low stability problem remains for blue TADF based systems.

A phosphor-sensitised fluorescence approach[87–91] offers an alternative to conventional phosphorescent and TADF emitters, for various emitting wavelengths, in an effort to overcome their individual shortcomings, by coupling both fluorescent and phosphorescent emitters. By utilising a phosphorescent donor and a fluorescent acceptor, distributed within a host, it is possible to obtain a dual emitting system, that is both stable and efficient. A unicoloured phosphor-sensitised fluorescence (UPSF) approach, with matching donor and acceptor

* TPQ: triplet energy state and polaron interaction results in demotion to the singlet ground state and a higher energy polaron capable of organic molecule decomposition.[70]
† TTA: combining the energy of two separate triplet excited states, bring one molecule to the singlet ground state and the other to higher energy triplet state, leading to potential degradation.

emission colour, was recently proposed for blue OLEDs.[92,93] The complementary simulation study is discussed in chapter 3.

1.4 Types of OLED and device architecture

1.4.1 Top or bottom emitting

The standard bottom emitting OLED structure, as shown in Figure 1.3 (a), emits light through the transparent substrate and bottom anode, usually indium tin oxide (ITO), while the top cathode is a highly reflective metal surface. As ITO is deposited using a sputter deposition process, with highly energetic particles, such that any underlying organic layers would be the subject of degradation. It is for that reason that ITO is used as the bottom (first) layer, deposited prior to the organic layers.

Top-emitting OLEDs emit light away from the substrate, in the opposite direction, this is required when the display is built on an opaque substrate. A highly reflective bottom anode is used, the deposited organic layers are then followed by a semi-transparent top cathode for outcoupling.[94,95] The top cathode may also be used with an organic capping layer on top, in order to control interference and tune spectral characteristics for improved light outcoupling.[96] Together the bottom and top contacts form an optical cavity, increasing the aperture ratio of the display. The microcavity effect creates a strong dependence of the emitted light on the device structure and the viewing angle,[95] such that different cavity lengths, adjusted with layer thickness and design, can be utilised to alter and purify the emission colour.[94]

Additionally, there exists inverted OLED structures, fabricated in the reverse order. Here the cathode is placed on the substrate, followed by electron injection and transport layers, next the emissive layer, then the hole transport and injection layers and finally the top anode. Inverted OLED structures are useful if the bottom contact is directly connected to the drain electrode of a n-type thin-film transistor, for electron injection. An advantage of this device architecture is that device lifetime is improved, as the more environmentally sensitive electron injection layer, is protected by upper organic layers (opposite to conventional OLED design). For top emission, this structure requires an anode that is transparent and conductive, to allow for uniform light emission and effective hole injection. The main challenge is the deposition of this top anode,

ideally a material such as ITO, which, however, can damage the underlying organic layers, as previously stated. Therefore one approach involves the use of a protective layer, which has been investigated in order to withstand any damaging effects of sputtering of the ITO layer, while remaining transparent and facilitating hole injection.[97]

On the other hand, for bottom inverted emission, the top anode is usually an air-stable metal, which increases the overall device stability. The drawback, however, is that they require high operating voltages due to the large injection barrier between the bottom cathode and electron injection layer. Therefore, the bottom cathode has to be modified. This has been done with the use of metal oxides, such as ZnO and a further n-doped interlayer before the electron injection layer, which has been proven to be effective.[98]

1.4.2 Tandem device

A tandem OLED or a stacked OLED structure, utilises two or more electroluminescent layers, connected by a charge generation layer. They have been demonstrated to improve device performance, largely due to the interconnecting (p-n junction) layer between the emissive layers.[99] Such device structures can be used to obtain full-colour OLED pixels, for example with the use of vertical stacking of red, green and blue emitting units.[100] This approach utilises three independent electrodes, such that the various colours and colour mixing can be easily controlled. The advantage of this is that with vertically stacked pixels the pixel density of the display can be significantly increased, resulting in higher brightness and improved image quality. Typically, the red, green and blue pixels are in a side-by-side arrangement, therefore only one third of the display contributes to the emission.[100] The stacked arrangement is a promising alternative to the conventional pixel arrangement, but requires further investigation before commercial application, due to its complex nature.

1.4.3 Flexibility

Flexible displays, which are foldable or rollable, are a unique property to certain OLED devices, making use of a flexible organic substrate. The fabrication of a fully flexible OLED using polyethylene terephthalate (PET) as the substrate was shown to have flexible properties, while remining mechanically robust.[101] However, the material stress in the multilayer structure

and the potential it has to ultimately lower the device performance, remains to be fully understood. Therefore, certain research efforts have focused on this specifically,[101–104] investigating the stress reduction in the ITO anode and how the thermal stress or bending may deform or delaminate the OLED layers. Careful choice of an extra encapsulation layer and focusing on structural design may aid with these limitations. With further advancement, flexible OLED displays present unparalleled application possibilities.

1.4.4 Transparency

A transparent OLED contains only transparent constituents and has the ability to emit from both directions. Both the top and bottom contacts are optically transparent to allow for light transmission when the device is switched on. When the device is switched off, transparent OLEDs can achieve around 85% transparency,[105] meaning that they can be used in applications such as window or windscreen displays. The main difference between transparent and conventional bottom emitting OLEDs, is the replacement of the top metal electrode by a transparent substitute. As previously mentioned, ITO is the perfect candidate for a transparent and conductive electrode, however the top layer deposition can damage the underlying organic layers. Therefore, efforts have been made to utilise a semi-transparent thin metallic film and an upper deposited organic capping layer to improve its light emitting performance,[106,107] similar to that of top emitting OLEDs.[96]

1.4.5 Passive Matrix OLED

A passive matrix OLED (PMOLED), makes use of rows of anode, followed by organic layers and then rows of cathode arranged perpendicular to the underlying anode rows. Device control is achieved at the intersection points of the anode and cathode, which represents the individual pixels. Each row of the display can therefore be independently controlled, determining which OLED will be activated and generate light. They typically consume more power than other types of OLED, due to the external circuitry they require,[108] but less than that of comparable LCDs. Due to the fact that they do contain a storage capacitor and each pixel is mostly switched off, they require larger operational voltages, which in turn lowers the lifetime of the device.

Therefore, PMOLEDs are best suited for small screen alphanumeric or icon displays, like those found in MP3 players, car radio displays and wearable fitness trackers.

1.4.6 Active-Matrix OLED

Active-matrix OLED (AMOLED) displays are the most recognised OLED displays, used in various applications, such as smartphones, tablets, laptops and televisions. They are more expensive than PMOLEDs, but they offer a more advanced design and higher image quality. An AMOLED utilises full layers of cathode and anode. The anode is placed above an array of thin film transistors (TFT), forming the circuitry which regulates the on/off state of each pixel. Allowing for a near instantaneous switching of the individual OLED emitters between images, thereby improving the quality. Additionally, this results in improved device efficiency as the use of a TFT array allows for lower power consumption, compared to PMOLEDs. AMOLEDs enable the use of OLEDs in large display applications, with increased resolution and improved image quality. Such technology can utilise the various device architectures, such as top emission, transparent and flexible designs, making AMOLEDs the current favourable choice for OLED display applications.

1.5 Applications

Extensive research efforts have progressed rapidly in recent years, pushing OLEDs into the initial phase of commercial production. With display applications being an essential component of many modern electronic devices, the unique properties of OLEDs have propelled them into the industry. The mechanically flexible, transparent and lightweight properties, create a whole host of new emissive technologies and applications in this rapidly expanding market. Therefore, the advancement of these devices is highly anticipated. In comparison to rigid inorganic LEDs, OLEDs offer a unique flexible substitute, with possibilities including curved, foldable and wearable displays. Additionally, as they are self-emissive and do not require a backlight, a better contrast ratio is achieved and an overall improved image quality, compared with LCD (liquid crystal display) technology.

OLED displays offer an alternative to other display technologies, bringing their own unique properties. AMOLEDs for example, offer vivid colours, a slim design and lower power

consumption on mobile devices. It is therefore understandable why they are used in smart phones (illustrated in Figure 1.5) and other devices, with Samsung showcasing this new screen technology in their recent generation smart phones.[109]

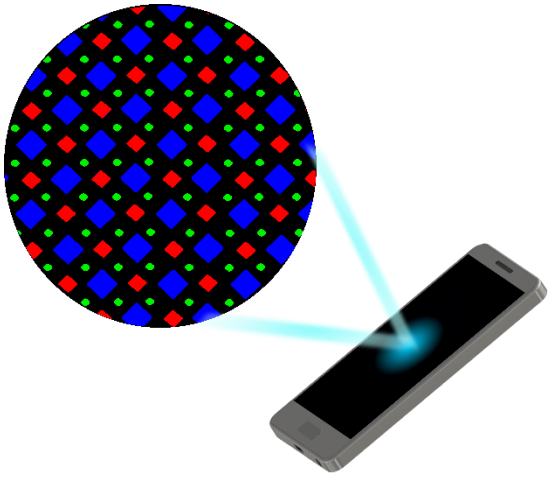

Figure 1.5 An application of an OLED display in a mobile phone, showing a magnified subpixel arrangement, the blue, red and green pixels are shown. Blue having the lowest efficiency of all three emitters, is the largest in size. This is an example of a diamond sub pixel arrangement, maximising the packing and subsequently the number of pixels in the display.

The flexible AMOLED technology has also already reached the market, with a prime example being the Samsung galaxy fold, featuring a foldable display.[110] LG also produces flexible OLEDs for wearable devices and smartphones, found for example in the Apple smart-watch.[111] Additionally, LG produces commercial OLED TV panels, as the world leading OLED TV producer, while also suppling OLED display panels to other notable electronic companies. LG promote the OLED technology through the 'infinite contrast' ratio, 'perfect black' (no back-light required), vivid colours, no colour distortion from any viewing angle, and a slim light-weight design.[112] Further to this, transparent OLED display prototypes have been demonstrated by both Samsung and LG in recent years, but mass production and future developments remain to be established. OLED applications also include the automotive industry, with OSRAM stating that OLED is the future of car lighting, including indicators, tail lights and interior lights.[113] Flexible OLEDs for vehicle lighting have been presented by the company, promoting a high level of homogeneity and efficiency, incorporated in a lightweight and flat design.[114]

Additionally, white OLEDs are a competitor to traditional light sources, such as incandescent bulbs, fluorescent tubes, or inorganic LEDs. White OLEDs potentially offer all of the aforementioned OLED characteristics, including ultrathin, lightweight, flexible and transparent properties. Generally, a combination of emitters is used to obtain the white light, for example within a tandem device. OLED flat light sources offer applications such as panel displays, which can be implemented within wall coverings, ceiling lighting or as light partitions. In 2012, OSRAM presented a glass panel transparent OLED at industrial maturity,[115] paving the way for future developments.

1.6 Current challenges

While they do offer an enticing substitute, OLEDs remain in their commercial infancy with respect to their inorganic counterpart, so continued research is essential in improving device efficiency and stability for commercial advancement. The performance and lifetime of these devices remain to be the bottleneck of the technology. As discussed, this is particularly true for blue emitting OLEDs, with the lowest efficiency and lifetime among all of the emitters, highlighting a key challenge which has to be addressed. The inefficiency of blue emitters can already be substantiated by looking at a subpixel arrangement for mobile phone application, in Figure 1.5, with the size of the sub pixel reflecting its efficiency, blue being the least efficient are the largest pixels, while green, the most efficient are the smallest.

Various factors affect the performance of an OLED and typically there is never an ‘ideal’ solution to obtain an optimised device, such that a compromise between stability, efficiency and colour coordinate, is inevitable. With appropriate material design, it is possible to achieve devices which balance these individual limitations. This has been demonstrated for an emissive layer, with the novel concept of UPSF, discussed in chapter 3, where a phosphorescent donor and fluorescent acceptor achieved a trade-off between stability and efficiency, while preserving the sky-blue emission colour. Maximising device performance has previously focused solely on improving the stability of the organic materials used. However, due to the advent of the new 5G standard for mobile applications, the focus has shifted more towards increasing efficiency and also reducing the driving voltage of each layer.

2 How can OLEDs be simulated?

Simulations can, not only be advantageous, but are an essential tool in the design of future OLEDs. In the search for increased device lifetime and efficiency, multiscale simulations can provide insight into material design, by predicting solid-state electronic properties, such as ionisation energy, electron affinity and electron and hole mobility. With many potential candidates for each layer and many potential emissive paths, it is crucial that simulations provide information, which otherwise would not be accessible.

Currently, there are well established methods for helping to optimise the stacked OLED architecture, by modelling light outcoupling and the balancing of hole and electron transport.[116,117] The next step is now to incorporate molecular details and achieve a mechanism of evaluating OLED chemical design.[118,119] The goal is to predict physical properties and relate these to chemical composition, also known as the forward problem, this would allow for pre-screening and an overall better insight. This extraction of properties from molecular structure alone is, of course, non-trivial and computational pre-screening is not yet accurate enough for this task exclusively.[120] However, a collective experimental and *in-silico* approach can be beneficial, due to the fact that there are a vast number of potential candidates and experimental pre-screening is notoriously time-consuming. The simulations of organic semiconductors, including OLEDs, require a broad range of length and time scales, in order to accurately predict device characteristics from a molecular structure. Therefore, a multiscale approach is essential, with the inclusion of atomistic descriptions, realistic molecular morphologies and charge transport simulations, to obtain a link between molecular and device scale properties.

This includes quantum chemistry calculations for investigating isolated molecules, ground state geometries (charged and neutral), ionisation energies and electron affinities. The subject of morphology is then addressed by molecular dynamics (MD) simulations, with classical force fields describing atomistic interactions within the molecule and polarisable force fields accounting for environmental contributions. This is followed by the progression to charge transport simulations, whereby it is possible to extract macroscopic observables, such as charge

carrier mobilities, achieved by solving the master equation, for the stochastic time evolution of the system. By doing so, device properties can be simulated, such as current-voltage characteristics and charge-current density distributions. A typical multiscale workflow is outlined in Figure 2.1.

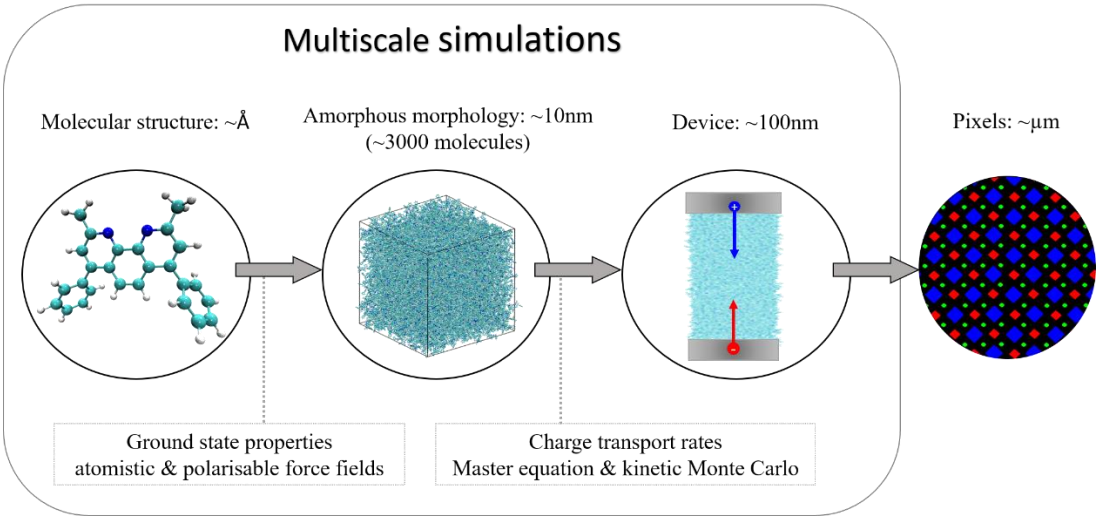

Figure 2.1 OLED modelling multiscale simulation workflow: starting from the first principles calculations of an isolated molecule, combined with atomistic force fields to generate the amorphous morphology, with the use of molecular dynamics. Polarisable force fields are used to account for the environmental effects on the density of states. Site energies, reorganisation energies, and electronic coupling elements are computed, followed by the charge transfer rates. Kinetic Monte Carlo is used to solve the master equation, to study charge dynamics (e.g., carrier mobilities), giving macroscopic device characteristics. Device properties are crucial as they make up the subpixel arrangement for display application.

2.1 Quantum Chemistry

Accurate atomistic properties can be obtained by quantum chemical calculations. The computationally demanding first principles methods can provide insight into electronic structure and the ground state geometry of isolated molecules.[121] The aim of quantum chemistry is to solve the Schrödinger equation,[122] which in the time-independent from is given by:

$$\hat{H}|\Psi\rangle = E|\Psi\rangle \tag{2.1}$$

Where $\hat{H}$ is the Hamiltonian, defining the characteristics of the system, E is the energy and Ψ is the wavefunction. When considering a non-relativistic description of a system containing electrons (N_e) and nuclei (N_n), the corresponding Hamiltonian is:

$$\hat{H} = \sum_{i=1}^{N_n} \frac{\hat{P}_{ni}^2}{2M_i} + \sum_{i=1}^{N_e} \frac{\hat{P}_{ei}^2}{2m_e} + \frac{1}{2} \sum_{\substack{i,j=1 \\ i \neq j}}^{N_n} k \frac{Z_i Z_j}{|R_i - R_j|} + \frac{1}{2} \sum_{\substack{i,j=1 \\ i \neq j}}^{N_e} k \frac{1}{|r_i - r_j|} - \sum_{i=1}^{N_n} \sum_{j=1}^{N_e} k \frac{Z_i}{|R_i - r_j|} \quad (2.2)$$

Here, the first terms account for the kinetic energies of the nuclei and electrons, with the i-th nucleus and i-th electron momenta given by $\hat{P}_{ni}$ and $\hat{P}_{ei}$, respectively. Their mass is given by M_i, for the nucleus and m_e for electrons (constant for all electrons). The further three terms then include the constant $k = e^2/4\pi\varepsilon_0$ to account for Coulomb interactions (e is the elementary electric charge and ε_0 is the vacuum permittivity). The Coulomb terms then have the interactions: nuclear-nuclear (at positions R_i and R_j, with atomic numbers Z_i and Z_j), electron-electron (at positions r_i and r_j) and nuclear-electron (at positions R_i and r_j, with nuclei atomic number Z_i). These interactions and thus correlated motions, make the wavefunction of the Schrödinger equation dependent on the positions of all nuclei and electrons $\Psi(R_1, \dots, R_{N_n}; r_1, \dots, r_{N_e})$. A consequence of this is that solving the Schrödinger equation is impossible without applying certain approximations, thereby introducing methods from first principles.

2.1.1 Born-Oppenheimer approximation

In order to simplify the Schrödinger equation, approximations must be employed, one such example is that of the Born-Oppenheimer (or adiabatic) approximation.[123] Whereby the fast motion of electrons, compared with the slow-moving nuclei, allows for separate treatment of the two. This decoupling of electronic and nuclear motion, provides fixed positions of the nuclei and simplifies the Hamiltonian.

$$\hat{H}_{el} = \sum_{i=1}^{N_e} \frac{\hat{P}_{ei}^2}{2m_e} + \frac{1}{2} \sum_{\substack{i,j=1 \\ i \neq j}}^{N_e} k \frac{1}{|r_i - r_j|} - \sum_{i=1}^{N_n} \sum_{j=1}^{N_e} k \frac{Z_i}{|R_i - r_j|} \quad (2.3)$$

With the kinetic term for constant nuclear positions, as well as the attractive electron-nuclear potential energy, now both removed. Giving rise to the electronic Schrödinger equation, with the eigenvalue of electronic energy.[124] The nuclear coordinates can then be used to calculate the electronic energy, providing the potential energy surface (PES), from which the concepts of equilibrium and transition state geometries are defined.

2.1.2 Hartree-Fock

Upon invoking the Born-Oppenheimer approximation, with the removal of nuclear-electron correlation, the electronic wavefunction describes the probabilistic electron positions. However, the challenge of treating the correlations amongst electrons of a many-electron system remains. An initial step to target this can be to assume that the energy of a many-electron system can be simplified to the sum of the one electron contributions, then the corresponding one-electron Hamiltonian becomes separable.* The result of this is that individual electrons are found in a static mean-field, created by the other electrons. The many-electron eigenfunctions can be written as a product of (N) one-electron eigenfunctions,[124] giving a 'Hartree-product' wavefunction:

$$\Psi_{HP} = \psi_1\psi_2 \dots \psi_N \tag{2.4}$$

It is then the goal to find orbitals which minimise $\langle\Psi_{HP}|H|\Psi_{HP}\rangle$,[124] which is done in an iterative self-consistent manner, originally proposed by Hartree (1928).[125] This involves an initial guess of the wavefunctions (for occupied molecular orbitals), followed by the construction of the operators to achieve newly estimated wavefunctions, iterated until reaching the converged orbitals. The aforementioned Hartree-Fock (HF) theory is then constructed by an extension of this original self-consistent field (SCF) approach, to account for exchange effects on the Coulomb repulsion, implemented by Fock.[126] Which now obeys the Pauli principle, with the wave function expressed by a Slater determinant[127] of one-electron orbitals. The one-electron Fock operator (f_i) then takes into account the coulomb and exchange contributions, with the introduction of a HF potential ($V_i^{HF} = 2J_i – K_i$) and is defined for each electron (in atomic units) as:

* Due to the one-electron kinetic energy and nuclear attraction terms being the only contributions

$$f_i = -\frac{1}{2}\nabla_i^2 - \sum_j^{N_n} \frac{Z_j}{r_{ij}} + V_i^{HF} \quad (2.5)$$

The practical computational development, permitting the calculation of HF theory was achieved in 1951 by Roothaan,[128] utilising matrix algebraic equations to represent molecular orbitals as basis sets. The Roothaan approach of HF theory is used to optimise electron orbitals in a SCF manner, to obtain the energy minimum for a single Slater determinant wavefunction from the chosen basis set.[124] However, as the fundamental mean-field approximation of electron correlation remains and all but exchange effects are excluded, HF theory has significant chemical limitations. Certain techniques have been employed to correct for this, by estimating the electron correlation energy, these represent post-HF methods and include configuration interaction (CI)[129] methods,* Møller and Plesset's use of perturbation theory (MPn methods) [130] and coupled-cluster (CC)[131] methods. That being said, these methods also incur increased scaling behaviour and as such, can become computationally demanding.

2.1.3 Density Functional Theory

The challenges facing wave-function based methods have been presented by HF theory, the alternative to these methods involves working with the total electron density, thereby introducing density functional theory (DFT). The basis of DFT is that the electron density can be used to evaluate the molecular energy. This is possible for a known density, from which the nuclear positions† and the number of electrons (N_e) in the system can be found, such that the Hamiltonian operator can be generated, ultimately determining the wavefunction.

Hohenberg-Kohn Theorem

The fundamental theorems of DFT reside with Hohenberg and Kohn (1964),[132] establishing two critical conditions by which the method can be brought to a realisation. The first of which, the 'existence' theorem, states that there does in fact exist a method of generating the Hamiltonian from the ground state electron density of the system (although, not providing a method in which to obtain the density). Considering a system of interacting electrons, the

* Full CI with an infinite basis set giving the 'exact' solution to the electronic Schrödinger equation, but is computationally demanding and has practical restrictions

† As the nuclei are represented as point charges, the positions are represented by the local maxima of the electron density[124]

electron density integration would provide N_e. Therefore, only the additional electron interactions with an 'external potential' (i.e., nuclei attraction) has to be determined, in order to construct the Hamiltonian. The first theorem then affirms the existence of a non-degenerate ground-state electron density which can determine this external potential, thus providing the Hamiltonian (used to determine the ground-state and excited-state wavefunctions).[124] The non-degeneracy then introduces the second 'variational' theorem, in which the density obeys a variational principle, such that the density that minimises the energy (true ground-state energy) is then the true ground-state density.

Kohn-Sham SCF method

However, the outlined Hohenberg-Kohn Theorems, do not simplify the challenges facing HF methods. In that, the Schrödinger equation remains to be solved, from the determined Hamiltonian and wavefunction. The electron-electron interaction term of the Hamiltonian, being the source of this complexity. An initial step to simplify this matter, was with the consideration of a non-interacting system of electrons, proposed by Kohn and Sham (1965).[133,134] The many-body problem then becomes a set of one-electron equations, analogous to that of HF theory. The separation lies with the innovative approach of Kohn-Sham, using a hypothetical system of non-interacting electrons and a real system to obtain matching ground-state densities. The density ($\rho(r)$) providing the essential components of the Hamiltonian, i.e., the positions and atomic numbers of the nuclei, with these quantities being indistinguishable between the real or hypothetical system. The electron density expressed in terms of single electron wavefunctions is then given as, $\rho(r) = \sum_{i=1}^{N_e} \langle \psi_i | \psi_i \rangle$. The energy functional $E[\rho(r)]$ is then divided into several contributions:

$$E[\rho(r)] = T_{NI}[\rho(r)] + V_{ne}[\rho(r)] + V_{ee}[\rho(r)] + E_{XC}[\rho(r)] \tag{2.6}$$

Including the kinetic energy of non-interacting electrons T_{NI}, the nuclear-electron attraction V_{ne} and the electron-electron repulsion V_{ee}. The final term (with unknown functional form) is the exchange-correlation energy E_{XC}, which also includes the correction of kinetic energy (due to the difference of a real and hypothetical system) and a correction to the electron-electron interaction energy.

By following the course of finding the orbitals which minimise the energy, satisfying the pseudo eigenvalue equations $h_i^{KS}\psi_i = \varepsilon_i\psi_i$, the Kohn-sham operator (h_i^{KS}) can be defined as:[124]

$$h_i^{KS} = -\frac{1}{2}\nabla_i^2 - \sum_j^{N_n}\frac{Z_j}{|r_i - r_j|} + \int\frac{\rho(r')}{|r_i - r'|}dr' + V_{xc} \quad (2.7)$$

Where V_{xc} is a functional derivative ($V_{xc} = \delta E_{XC}/\delta\rho$). The separable non-interacting Hamiltonian can then be defined as the sum of the Kohn-Sham operators, with the orbitals (ψ) used to find the density, forming the Slater determinant eigenfunction, written as:

$$\sum_{i=1}^{N} h_i^{KS}\ |\psi_1\psi_2 ...\psi_N\rangle = \sum_{i=1}^{N}\varepsilon_i\,|\psi_1\psi_2 ...\psi_N\rangle \quad (2.8)$$

The Kohn-Sham equations are solved in an iterative SCF process, similar to that for HF theory.

Exchange-correlation functionals

The main challenge is to approximate the exchange-correlation energy (E_{XC}), as a function of the density. This functional dependence can be expressed in terms of an interaction between electron density and exchange correlation energy (ε_{xc}) density:

$$E_{XC}[\rho(r)] = \int\rho(r)\varepsilon_{xc}[\rho(r)]dr \quad (2.9)$$

One such method is the local density approximation (LDA), where a 'local' character of the density is assumed, such that at a certain position the exchange correlation energy can be exclusively found from the density (single-valued). Further to this, to account for local changes in the density, an extension of the LDA is required, known as the generalised gradient approximation (GGA), developed by Becke[135] (usually abbreviated to 'B'). Functionals which include the density and the gradient of the density are the so called gradient corrected functionals.[124] The full correlation energy can be computed, by a GGA correlation functional, developed by Lee, Yang and Parr (LYP).[136] A combination of the two methods can then be utilised providing, for example the BLYP functional.[135,136]

Additionally, the 'adiabatic connection method' (ACM),[137] used to connect the non-interacting system to the real system, can be used to derive hybrid functionals. By combining HF exact

exchange for the non-interacting system, using KS orbitals and using DFT methods such as the GGA for the density. A common example of a hybrid functional is B3LYP[135,136,138] (where the 3 represents the 3-parameter functional expression used). Here the LSDA (local spin density approximation), KS-orbital HF and GGA are used to compute the exchange energy, while for the correlation energy the LSDA is used with the LYP full correlation functional.

2.1.4 QM description for charge transport parameters

Quantum mechanical (QM) descriptions provide insight at the atomic scale, thereby determining properties such as electronic structure and ground state or excited state geometries. This in turn allows for energy calculations upon addition or removal of an electron (leading to a structural rearrangement), providing ionisation energy (IE_0) and electron affinity (EA_0) values for a molecule in the gas phase. DFT calculations are used to obtain the IE_0 and EA_0 of the molecule, by computing the energy of the charged molecule in the charged geometry E_{cC} and the energy of the neutral molecule in the neutral geometry E_{nN}. The IE_0 and EA_0 values can then be calculated as:

$$E_{IE}^{int} = E_{cC}^{h} - E_{nN} \tag{2.10}$$

$$E_{EA}^{int} = E_{cC}^{e} - E_{nN} \tag{2.11}$$

With the cationic state (h) representing the loss of an electron for the IE_0 and the anionic state (e) representing an electron addition for the EA_0. These internal molecular energies E^{int} and the constituent charge and neutral geometries/states are discussed in further detail in section 2.3, for charge transport simulation parameters, namely, the site energies, reorganisation energies and electronic coupling elements.

2.2 Molecular Dynamics

Although QM descriptions can be effectively utilised for accurate energy calculations of charged and neutral geometries, they come at a high computational cost. Therefore, these computational demanding first principles calculations are an inefficient and often unfeasible approach for realistic morphology sizes, required for charge transport simulations of amorphous organic materials. As such, an additional method has to be considered, that of

molecular dynamics (MD) simulations, to further understand molecular assemblies and microscopic interactions.[139] In order to study large bulk like systems, a simulation box exhibiting periodic boundary conditions (pbc) can be used to account for finite size effects (systematic errors due to small system size).

MD simulations involves the propagation of atoms through time, when acted upon by interatomic forces, taking the system from one state to the next with each time step. Essentially allowing the time evolution of a system to be studied, based on the classical mechanics of Newton's equations of motion. Using Newton's second law, the atomic masses (m_i) and centre of mass positions (r_i) can be used to describe the interatomic forces (F_i) such that $F_i = m_i \ddot{r}_i$. The forces acting on the atoms are then calculated according to a potential energy (U), based on all atomic positions:

$$F_i = -\frac{\partial}{\partial_{r_i}} U(r_1, \dots, r_N) \tag{2.12}$$

With the potential describing the interatomic interactions, in terms of bonded (intramolecular) or non-bonded (intermolecular) interactions.

2.2.1 Classical force fields

The comprehensive description of the potential (U) defines a force field, where all interactions are considered, including all bonded and non-bonded contributions. Atom types are specified based on these contributions, such that bonds, angles, torsions and long-range interactions can be described. Here, an atom type is specified, which not only refers to the element type, but also the chemical environment and interactions with surrounding atoms. For example, there can be more than one type of carbon atom within a molecule: one carbon may only be surrounded by other carbons or hydrogens, while a second carbon atom may have a direct bond to a heteroatom. This difference impacts the atomic interactions, both short and long ranged, therefore it has to be explicitly categorised. With a clear definition of atomic types, the bonded and non-bonded interactions can then be described.

Bonded interactions

Short range intramolecular interactions, or bonded interactions are constructed from four basic concepts: (a) the bond itself, (b) the angle, (c) the dihedral and (d) the improper, as shown in Figure 2.2.

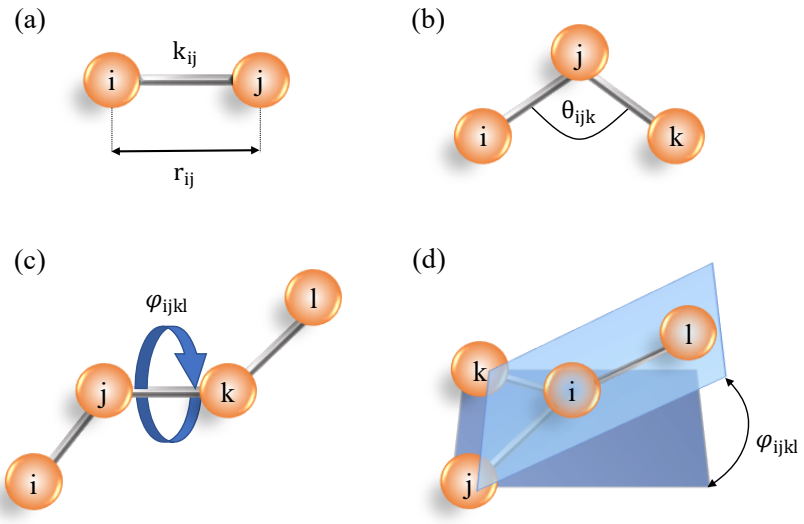

Figure 2.2 MD bonded interactions: (a) stretching or contracting of the bond between atoms i and j, (b) bending of the angle between there atomic coordinates (i, j, k), (c) torsional dihedral angle around the j-k bond and (d) torsional improper angle.

The bonded interactions, consisting of the bonds, bonding angles and torsion angles (which describe three connected bonds, giving the improper and dihedrals) is commonly given by:

$$\begin{aligned} U_{bonded}(r_1, \ldots, r_N) = & \frac{1}{2} \sum_{bonds} k_{ij}^{r} \left(r_{ij} - r_{eq}\right)^2 \\ & + \frac{1}{2} \sum_{\substack{bond \\ angles}} k_{ijk}^{\theta} \left(\theta_{ijk} - \theta_{eq}\right)^2 \\ & + \frac{1}{2} \sum_{\substack{torsion \\ angles}} \sum_{m} k_{ijkl}^{\varphi,m} \left(1 + \cos\left(m\varphi_{ijkl} - \gamma_m\right)\right) \end{aligned} \tag{2.13}$$

The first term represents the stretching or contraction of a bond between two atoms (i and j), with separation $r_{ij} = |r_i - r_j|$, within a molecular framework. The equilibrium separation (r_{eq}) can,

for example be defined by a harmonic approximation.[140] The second term, defines the bending of the bond angles θ_{ijk}, between the connected bonds of three atomic coordinates (i, j and k), with equilibrium value θ_{eq}. The final term is the torsion angles φ_{ijkl}, between four atomic coordinates (i, j, k and l). The torsional potential usually requires expansion in periodic functions of order (m = 1, 2, …). Equation (2.13) represents a simplified version of the bonded interactions, as it is also possible to include cross-terms.

Force fields specify the various parameters required to understand the bonding within the system. Experimental results or DFT calculations of a single molecule are typically used to parametrise force fields. By scanning the different degrees of freedom, it is possible to make necessary adjustments to the parameters, in order to obtain a good energetic agreement to the DFT results.[2] It is also possible to include constraints to the molecular geometry, for MD simulations. This can include fixed bond lengths, implemented because of the high vibrational frequency of bond length alterations. Constraints can also include planar adjustments to the angles, in order to keep a molecular geometry flat, which may be required for specific organic molecules.

Non-bonded interactions

The long-range, non-bonded contribution of the potential ($U_{non\text{-}bonded}$) is typically spilt into 1-body, 2-body and 3-body terms, given by:

$$U_{non-bonded}(r_1, \dots, r_N) = \sum_i u(r_i) + \sum_i \sum_{j>i} v(r_i, r_j) + \cdots \tag{2.14}$$

The first term, $u(r_i)$ represents an externally applied potential or boundary effects. However, this term can usually be neglected for bulk and fully periodic systems. The most significant constituent is the pair potential $v(r_i, r_j) = v(r_{ij})$, based on the atomic distance (r) between pairs i and j, with the Lennard Jones (LJ) potential being the most commonly used form:[140]

$$v^{LJ}(r_{ij}) = 4\varepsilon \left[\left(\frac{\sigma}{r_{ij}} \right)^{12} - \left(\frac{\sigma}{r_{ij}} \right)^{6} \right] \tag{2.15}$$

Here, ε defines the depth of the potential well and σ is the distance at which the potential is zero. The LJ potential describes the pair interaction in terms of short-range Pauli repulsion

expressed by the r^{-12} dependence on distance, and long-range Van der Waals attraction expressed by the r^{-6} dependence.

Furthermore, when electrostatics are to be considered, an additional long-range contribution to the non-bonded interaction is included, known as the Coulomb potential. When considering these long-range interactions of molecular charges, which would require integrals over two charge densities, approximations have to be made to lower computational cost. To this aim, partial (fractional) charges q_i and q_j, centred on atoms i and j can be effectively utilised to model the Coulomb interaction.

$$v^{\mathrm{Coulomb}}(r_{ij}) = \frac{q_i q_j}{4\pi\varepsilon_0 r_{ij}} \tag{2.16}$$

Where the partial charges are separated by a distance of r_{ij} and ε_0 is the vacuum permittivity. The total non-bonded contribution to the potential is then constructed from the Pauli repulsion, Van der Waals attraction and Coulomb potential. Noting that, for systems with periodic boundary conditions, the long-range interactions can become troublesome, such that charges and image charges (mirrored charges in periodic boxes), also interact. This requires increasingly complex Coulomb interactions to be evaluated and more accurate methods have to be employed.

2.2.2 Ensembles

Molecular dynamic simulations involve the time evolution of a molecular system, in steps of possible system states. The states in which the system can be found, are a result of its kinetic and thermodynamic properties. A specification of the possible system states is therefore required, introducing the use of an ensemble within MD simulations. An example would be: using a fixed number of particles (N), within a fixed volume (V), with fixed total energy (E), defining the **NVE** ensemble, where these fixed values are maintained for all possible (evolving) states. As the energy is always conserved within the NVE ensemble with the progression of time, such that it cannot exchange energy with the surrounding environment, it defines a micro-canonical ensemble. Additionally, there is a canonical ensemble which represents the possible states of the system in thermal equilibrium with the environment, with a fixed temperature (T), a fixed number of particles and a fixed volume, this is then the **NVT** ensemble. When considering thermodynamic equilibrium with the environment, the grand-canonical ensemble

is important, within this regime, there is a constant chemical potential (μ), a constant temperature and volume, usually called the **μVT** ensemble. Finally, the consideration of pressure is essential for chemical reactions taking place under constant pressure (P). This can be defined by the isothermal–isobaric ensemble, with constant temperature, pressure and number of particles, also called the **NPT** ensemble.

Thermostats and Barostats

Newton's equations of motion correspond to the NVE ensemble, such that energy is conserved. However, when considering chemically relevant systems, in order to represent experimental conditions of constant temperature and/or pressure, the various other ensembles are necessary. Therefore, to obtain the correct dynamics and control aspects of the simulation, the typical equations are used in combination with a thermostat, to maintain the temperature, and/or barostat to maintain the pressure.

A thermostat is used to model the constant temperature constraint of the various applicable ensembles. Allowing energy exchange between the system and the environment, using a heat bath or energy reservoir. The temperature (T) is related to the velocity (v_i) of N particles, given by:

$$\frac{k_B T}{2}(3N - n_c) = \sum_{i=1}^{N} \frac{1}{2} m_i |v_i|^2 \tag{2.17}$$

Where k_B is the Boltzmann constant, 3N is the 3-dimenisonal degrees of freedom (x, y, z), n_c is the number of constrained degrees of freedom, and m_i is the mass of particle i. As the velocity of the particles are known at each MD step, it is therefore possible to adjust the velocity in order to control the temperature, with equation (2.17). However, controlling the temperature by altering the velocities of all particles at each time step, does not allow for statistical temperature fluctuations and so does not represent a thermodynamic ensemble. Therefore, this formulism has to be accurately adapted.

The Berendsen thermostat[141] uses weaker velocity scaling, by coupling the kinetics to an external heat bath with a given temperature (T_0). The re-scaling of the velocities then corrects the temperature deviations, between the current and the desired temperature (T_0). The kinetic energy fluctuations are still supressed by the Berendsen thermostat and so, it does not generate a canonically-distributed trajectory, although it is, possibly, sufficient for smaller system sizes

of a few hundred particles. The Andersen thermostat[142] rescales the velocities with random velocity updates of randomly chosen particles, based on Boltzmann statistics, but also has limitations in terms of canonical velocity trajectory predictions.[2] The correct sampling of a canonical ensemble, is achieved by the, computationally more demanding, Nosé-Hoover temperature coupling thermostat.[143,144] Treating the heat bath as an integral part of the system, defined as a reservoir, the current temperature and desired temperature are then coupled. An approach to combine efficiency and accurate dynamics is often employed, for example the combination of the Berendsen and Nosé-Hoover thermostats, which brought the development of the velocity rescaling thermostat,[145] to allow for kinetic energy fluctuations.

The NPT ensemble requires a barostat to allow fluctuations of the box volume, thereby obtaining a constant pressure. Using Berendsen pressure coupling approach, the particle coordinates and simulation box vectors are rescaled at each MD step. Similar to the Berendsen thermostat, the pressure coupling approach does not accurately describe the thermodynamic ensemble, therefore it is primarily used to achieve an equilibrated system.

2.2.3 Polarisable force fields

Polarisation or induction, is defined as the adjustment of a molecular charge distribution, in relation to a change in the environmental charge distribution.[2] As standard force fields, with static and typically atom-centred charges cannot account for the effects of electronic polarisation, such as (molecular) geometric and energetic alterations, a further approach is required. Polarisable forces fields can incorporate appropriate variations in charge distribution with the use of distributed polarizabilities and higher multipoles (e.g., quadrupole moments). Offering a perturbative mechanism[121] for inclusion of electrostatic, induction, and van der Waals interactions.[146]

In contrast to standard force fields, with experimentally parametrised effective charges and Lennard-Jones parameters, polarisable force fields can be parametrised from first principles. The advantage of this being that no experimental input is initially required, such that pre-screening of new potential candidates for organic semiconductor applications (prior to synthesis) is possible. However, in large systems the increased complexity of interactions makes this a computationally demanding approach, as a self-consistent solution of coupled non-linear equations is required for the evaluation of induced dipoles.[121] For that reason, they

are typically used in combination with standard force fields for large systems. Polarisable force fields are used to compute the site energies required for charge transport simulations (the various site energy contributions are discussed in section 2.3.3) and standard force fields are used to calculate the structural properties of large-scale morphologies.

2.3 Charge Transport simulations

Charge transport in disordered organic semiconductors is described as a series of hops between different molecular sites (charge localised states). The rate of this hopping depends on various factors, attributed to the orientation and position of the molecules. These factors include site energies, reorganisation energies and electronic coupling elements, between neighbouring molecules. In order to effectively utilise these parameters to obtain valuable quantities, such as charge carrier mobilities, the master equation has to be solved. The master equation describes the movement of the system from one physical state to another, i.e., the stochastic progression of the system through time, by successive hops. It presents an analytical approach of solving the Schrödinger equation. Before proceeding to solving the master equation, carried out with the use of kinetic Monte Carlo (KMC), each of the charge transport parameters have to be outlined. All of the charge transport simulations described here, are carried out using the Versatile Object oriented Toolkit for Coarse-graining Applications (VOTCA) software package,[147,148] including the use of a newly developed KMC code (developed within the scope of this work).

2.3.1 Atomistic morphology to hopping sites

With the atomistic morphology generated from first principles, using polarisable force fields and the electronic properties of isolated molecules, a system for charge transport simulations can be obtained. This firstly requires conversion of the atomistic morphology into sites available for charge carrier hopping. Such sites are defined in terms of conjugated segments and rigid fragments. A small molecule, typically used for SM-OLEDs, can consist of various rigid fragments, i.e., planar π-conjugated components, which make up the molecule as a whole. For clarity, an example is shown in Figure 2.3, for the commonly used OLED small molecule, tris-(8-hydroxyquinoline) aluminium (Alq_3). The three shaded circles highlight each of the

rigid fragments in this molecule, surrounding the central metal atom. The conjugated segment is then defined as the entire molecule, as a charge carrier can delocalise over each of the three ligands. The delocalising, resulting in one conjugated segment, means there is one site available for charge carrier hopping on this molecule. The hopping site is then taken as the centre of mass position of the molecule and a mapping procedure is carrier out in order to ensure any discrepancies between molecular dynamics and the first-principle ground state geometry are rectified.

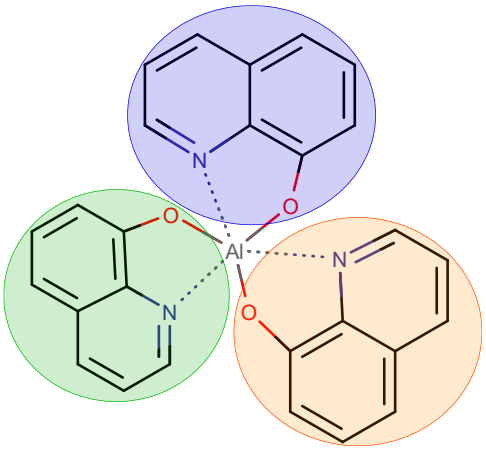

Figure 2.3 Molecular structure of Alq_3 [Tris-(8-hydroxyquinoline)aluminium] illustrating the three rigid fragment ligands (blue, orange and green shaded circles), with the central Al atom.[147,148]

2.3.2 Neighbour list

With hopping sites determined, a neighbour list can be constructed, this is defined as a set of neighbouring molecules within a specific rigid fragment, centre of mass cut-off to one another. This ensures that a nearest neighbour approach is adopted, such that the two rigid fragments with short separation can become charge transport neighbours, even with large conjugated segment centre of mass distances. The nearest neighbour intermolecular separation is an important factor for charge transfer simulations, with the electronic coupling elements decreasing exponentially with increasing separation. Therefore, molecules with large intermolecular separation distances can be excluded from the neighbour list, due to the highly improbable occurrence of charge transfer. Additionally, a well-defined neighbour list, which

includes only the necessary pairs of molecules to focus on, reduces the computational cost for the remainder of the charge transfer simulations.

2.3.3 Site energies

The neighbour list and hopping sites can then be used in combination to calculate the site energies, which typically has a Gaussian distribution. The site energy difference between two hopping sites is characterised as the driving force for charge transfer, due to its exponential dependence with the charge transfer rate, as shown in equation (2.27). The site energy for a given hopping site (i) is defined in terms of the internal molecular energy (E_i^{int}), electrostatic energy (E_i^{el}), induction (polarisation) energy (E_i^{pol}) and an applied external electric field (E_i^{ext}), by equation (2.18). The contribution due to an applied external electric field ($\vec{F}$) is given by, $E_i^{ext} = q\vec{F} \cdot \vec{r}_i$, with q being the charge (+/-) and r being the centre of mass of the molecule (i).

$$E_i = E_i^{int} + E_i^{el} + E_i^{pol} + E_i^{ext} \tag{2.18}$$

The site energy difference between two hopping sites i and j, is then specified by equation (2.19).

$$\Delta E_{ij} = E_i - E_j \tag{2.19}$$

Internal molecular energy

The internal molecular energy of each site, corresponding to the adiabatic ionisation energy (hole transfer) or electron affinity (electron transfer) of an isolated molecule, is calculated using first principles (Section 2.1). This is achieved by using the energy difference between a charged molecule (lowercase c) in a charged geometry (uppercase C) and a neutral molecule (lowercase n) in the neutral geometry (uppercase N), $E^{int} = U^{cC} - U^{nN}$. The internal molecular energy difference between two neighbouring sites (i and j) is outlined in equation (2.20). This corresponds to the difference between the potential energy surface (PES) minima of the two molecules in the electron transfer reaction, ($\Delta E_{ij}^{int} = \Delta U_i - \Delta U_j$) as shown in Figure 2.4.

$$\Delta E_{ij}^{int} = (U_i^{cC} - U_i^{nN}) - (U_j^{cC} - U_j^{nN}) \tag{2.20}$$

Electrostatic interaction

As it is computationally too expensive to evaluate all pair-wise interactions in the system, it is typically calculated as a sum of partial charges or multipoles for all molecules, using a spherical/cylindrical cut-off or by using Ewald summation (without a cut-off).[2]

Ewald summation

Long-range electrostatic interaction between partial charges or higher distributed multipoles,[149] can be computed by summation techniques, for example Ewald summation.[150,151] Which involves splitting the interaction into two constituent parts, in real space (short range) and in the quickly converging reciprocal space (long-range). When considering systems with a large number of particles, an efficient adaption of the Ewald method is used. The reason for this being, that the Ewald method scales with the number of particles (N), as N^2. The more efficient approach, the so-called particle mesh Ewald (PME),[152,153] consists of the evaluation of a discrete lattice or mesh, with the use of fast Fourier transform (FFT). This leads to a substantial reduction in computational cost, with a scaling of N log N, based on a well-chosen mesh size.

Distributed multipoles

Considering the interaction in terms of (molecule centred) multipoles, between two molecules (A and B), the interaction energy is expressed as:

$$U_{AB}^{(el)} = \sum_{a=1}^{A} \sum_{b=1}^{B} \hat{Q}_t^a \cdot T_{tu}^{ab} \cdot \hat{Q}_u^b \qquad (2.21)$$

The spherical multipole moment is given by Q_t^a and Q_u^b located on molecules A and B respectively, with the implicit sum over expansion sites, indices a and b using the Einstein summation convention. Additionally, the interaction between each multipole-moment component $t = l_1 k_1$ on site a and $U = l_2 k_2$ on site b, is specified by the multipole interaction tensor T_{tu}^{ab}. The multipoles can be derived from (1) the Distributed Multipole Analysis (DMA)[154,155] approach, working with the quantum-mechanical density matrix or (2) a least-squares charge fitting approach to reproduce electrostatic potential, for example using SCF density on a regularly spaced grid[121]

with the CHELPG (charges from electrostatic potentials, grid-based)[156] method or by using Merz-Kollmann method.[157,158]

Induction energy

The site energy contribution due to induction (polarisation) effects, can be calculated using the Thole model.[159] Utilising a set of molecular distributed multipoles (as previously discussed for electrostatic interaction, equation (2.21)) and polarizabilities. The addition of induction effects, introduces an induced moment (ΔQ_t^a), into the consideration of multipole moments, and as induction stabilises the charges, there is a positive correction to the molecular interaction energy, given by:

$$U_{AB}^{(pol)} = \frac{1}{2}\sum_{a=1}^{A}\sum_{b=1\ (b>a)}^{B}\left[\Delta Q_t^a\, T_{tu}^{ab}\, Q_u^b + \Delta Q_t^b\, T_{tu}^{ab}\, Q_u^a\right] \tag{2.22}$$

The interaction tensor is given by T_{tu}^{ab}, the permanent multipoles are given as Q_u^b and Q_u^a for molecules A and B respectively, similarly, the induced moments are specified by ΔQ_t^a and ΔQ_t^b. The induced contribution is then obtained self-consistently by:

$$\Delta Q_t^a = -\sum_{a=1}^{A}\sum_{b=1\ (b\neq a)}^{B}\alpha_{tt'}^{aa'}\, T_{t'u}^{a'b}\,(Q_u^b + \Delta Q_u^b) \tag{2.23}$$

Thole model

The semi-empirical Thole model can be used to obtain the polarizabilities, i.e., the polarizability tensor ($\alpha_{tt'}^{aa'}$), from fitting parameters for atomistic polarizabilities.[160,161] It is modified from dipole-dipole interactions, by making use of smeared charge densities. This is necessary due to the divergent behaviour of the interaction energy, for short atomic distances. The smearing of the charge density can prevent this, by essentially mimicking the nature of the QM wavefunction.[148] An exponentially decaying function can be used for the smearing of the charge density as implemented in VOTCA,[148,162]

$$\rho(u) = \frac{3a}{4\pi}\exp\left(-au^3\right) \tag{2.24}$$

With u representing the distance between two sites (a and b), such that $u = R/(\alpha_a \alpha_b)^{1/6}$ and a is the smearing exponent.

2.3.4 Reorganisation energies

When a molecule charges or discharges there is an energetic response, as such there is a reorganisation energy which takes into account the geometric rearrangement. Considering a charge moving from molecule i (donor) to molecule j (acceptor), there is an intramolecular contribution (λ_{ij}^{int}), due to the internal reorganisation of the two molecules, and an intermolecular or outersphere contribution (λ_{ij}^{out}), due to the relaxation of the surrounding environment.[147,163]

Intramolecular contribution

The internal contribution considers the alteration of the nuclei and core electrons in the charging and discharging pair. The neutral and charge states and geometries, U_i^{nN} (donor) and U_j^{cC} (acceptor) are included in the intramolecular reorganisation energy. Additionally, for the reorganisation energy there are a further two contributions to consider. With the internal energies of the neutral molecule in charged geometry, U_i^{nC} (for the donor) and charged molecule in the neutral geometry, U_j^{cN} (for the acceptor), also now included. The internal reorganisation energy, due to the discharging of site i (λ_i^{cn}) and charging of site j (λ_j^{nc}) is shown in equation (2.25).

$$\lambda_{ij}^{int} = \lambda_i^{cn} + \lambda_j^{nc} = (U_i^{nC} - U_i^{nN}) + (U_j^{cN} - U_j^{cC}) \tag{2.25}$$

This is also depicted in Figure 2.4, showing the four points which are relevant to the intramolecular contribution. The various charge states and geometries are calculated using DFT.

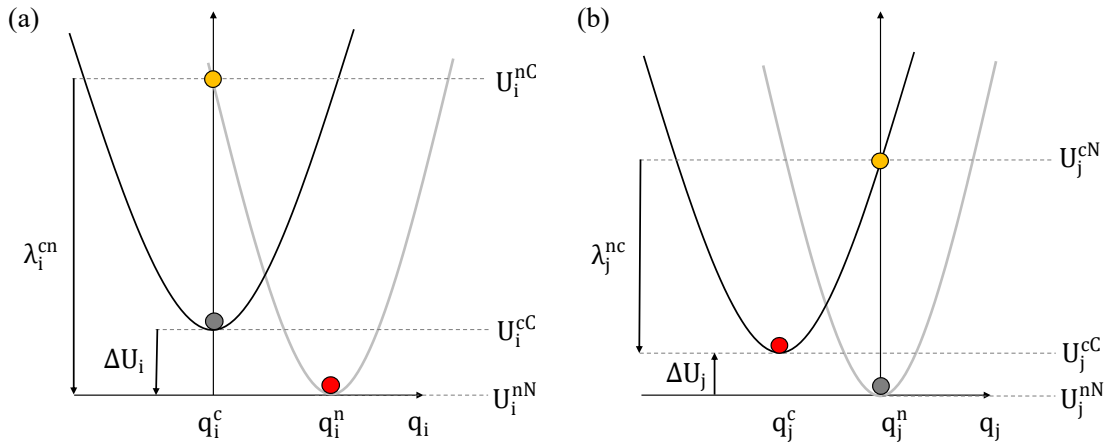

Figure 2.4 Potential energy surface (PES): for a (a) donor and (b) acceptor molecule in charged and neutral states. A change in the charge state (grey to yellow) is followed by relaxation of nuclear coordinates (yellow to red). For the intramolecular contribution to the reorganisation energy, the yellow and red points are relevant. For the difference in internal molecular energy for the contribution to the site energy (minima), it is the energy difference of the grey and red points. Figure reproduced from the VOTCA-CTP (charge-transport) manual.[147,148]

Outersphere contribution

The external contribution to the reorganisation energy, known as the outersphere contribution, takes into account the changes to the environment surrounding the charge transfer molecules. This describes the reorientation and polarisable adjustment of the surrounding molecules, due to changes in the electric potential. The outersphere contribution is particularly important for strongly polarisable environments.[118,147] If this contribution should be included, it can be calculated using the atomistic partial charges of neutral and charged molecules with a specified cut-off radius, using the electric displacement fields of the charge transfer complex,[147] based on the assumption that charge transfer occurs faster than the nuclear rearrangement of the environment, but slower than the electronic polarisation. Or by making the simplified approximation of spherical charge distributions on the two molecules with integration over the outer volume.

2.3.5 Electronic coupling elements

The electronic coupling element or electronic transfer integral element (J_{ij}), relies on accurate descriptions of the diabatic states localised on molecule i (ϕ_i) and j (ϕ_j) (monomers), as well as the Hamiltonian ($\hat{H}$) of the dimer formed by the charge transfer complex, according to:

$$J_{ij} = \langle \phi_i \left| \hat{H} \right| \phi_j \rangle \tag{2.26}$$

The diabatic states are typically taken as the HOMO of the monomer in the case of hole transport and the LUMO when considering electron transport, within a frozen-core approximation. The electronic couplings are highly dependent on the overlap of the orbitals participating in the charge transfer reaction, consequently, also on the molecular orientation and positions of the two molecules. As the couplings have a significant impact on the charge transfer rate (equation (2.27)), similar to site energy differences, they must be computed accurately. As such, the calculations can be extensive, as couplings are calculated explicitly for each individual pair. In an effort to balance computational cost and model reliability, there are several methods of calculating the transfer integrals including:

1. Semi-empirical methods, which avoids the explicit evaluation of the Hamiltonian, utilising parametrised models to lower computational cost (but also accuracy). The ZINDO (Zerner's Intermediate Neglect of Differential Overlap) method[164–166] is an example, involving parametrisation using first principles calculations and then estimation of the overlap integrals. By generating the orbitals from only a single isolated molecule calculation, it is possible to obtain the overlap integrals for each pair.[164]
2. DFT (or other electronic structure) methods, involving the projection of monomer frontier orbitals onto the explicitly calculated dimer Hamiltonian. This requires self-consistent calculations on each individual monomer and the corresponding pairs (dimers) and is therefore computationally demanding, but is required when semi-empirical methods fail. An example is the DIPRO (dimer projection) method.[167]

2.3.6 Charge transfer rates

Marcus rates

The rates for charge transfer reactions then combine all results of the previous steps, to include neighbouring sites (i and j), their site energy difference $\Delta E_{ij} = E_i - E_j$, reorganisation energy λ_{ij} and electronic couplings (J_{ij}). These key parameters are crucial for an accurate description of charge dynamics linked to the atomic morphology, achieved by using the Marcus rate equation.[168–171] This semiclassical rate, within the high temperature limit of classical charge theory,[168,171] is a thermally-activated mode of non-adiabatic charge transfer.* This expression is derived from the importance of environmental coupling, using linear response theory to describe a heat bath coupled to electronic tunneling.[172] This quantum mechanical tunnelling moves the electron from one molecule to the other, at sufficiently high temperatures, when the nuclear vibrations (also described as bath fluctuations) bring the corresponding energy levels into resonance. The rate for a charge to hop from site i to site j (ω_{ij}) is given by:

$$\omega_{ij} = \frac{2\pi}{\hbar} \frac{J_{ij}^2}{\sqrt{4\pi\lambda_{ij} k_B T}} \exp\left[-\frac{(\Delta E_{ij} - \lambda_{ij})^2}{4\lambda_{ij} k_B T}\right] \tag{2.27}$$

Additional to the key parameters outline above, the equation also includes the reduced Planck constant ($2\pi/\hbar$) and the thermal energy ($k_B T$). For the charge transport simulations described hereafter, the rate is calculated using the Marcus rate equation (2.27).

Additionally noting that Marcus rates are only valid for limited (high) temperature variations, there is a further calculation method, using the Weiss-Dorsey rates.[172–176] This is useful for a wider range of temperature regimes, specifically using the low temperature approximations, where nuclear tunnelling becomes the dominant pathway[172] and Marcus rates would not applicable.

* Valid for weak electronic coupling. Weakly coupled states are localised and strongly dependent on nuclear coordinates; the positions of which can lead to electronic transitions.

Miller-Abraham rates

An additional method of computing the rates is using the Miller-Abraham expression,[177] simpler than the Marcus expression, it neglects vital components of charge dynamics, including the reorganisation energy. The expression for these rates is shown in equation (2.28).

$$\omega_{ij} = \omega_0 \exp\left(-\frac{2r_{ij}}{r_{loc}}\right)\begin{cases}\exp\left(-\frac{\Delta E_{ij}}{kT}\right), & \Delta E_{ij} > 0 \\ 1, & \Delta E_{ij} \leq 0\end{cases} \quad (2.28)$$

Here the rate is specified in terms of the hopping attempt frequency ω_0 , an electronic coupling factor, which includes the distance between the two molecules r_{ij} and the localisation length of the charge r_{loc},[2] as well as the site energy difference, in this case $\Delta E_{ij} = (E_j - E_i)$. The first exponential term accounts for a simplified dependence of electronic coupling on separation distance, without inclusion of molecular orientation and the impact it has on the electronic coupling.[178] The second term includes a Boltzmann factor with a positive energy difference between the two hopping sites, or equals 1 for a hop downward in energy. This simplified rate expression can be utilised within the Gaussian disorder model.[179]

2.3.7 Gaussian Disorder Model

In the Gaussian disorder model (GDM), a simple lattice arrangement of sites is assumed, with (typically) uncorrelated site energies following a Gaussian density of states, due to random molecular orientations.[2] The width of the energetic distribution is known as the energetic disorder. Instead of Marcus rates, the GDM makes use of the Miller-Abrahams rate equation (2.28). Despite this simpler approach, with certain improvements (including correlated and extended correlated) GDMs have been able to explain certain aspects of charge carrier mobility (μ), such as the experimentally observed dependencies of carrier density and external electric field (F),[180–182] observed by the Poole-Frenkel dependence ($\ln \mu \propto \sqrt{F}$).[183] However, as GDMs cannot account for the atomistic scale spatial correlations, this method has a characteristic flaw in comparison to off-lattice models.

2.3.8 Master equation

With the hopping sites and charge transfer rates at hand, a method of simulating hopping transport is required. This is achieved by a stochastic description, known as a (continuous time) Markov process, which fulfils the requirement of memory-less charge transport, such that each new hopping event depends only on the current state of the system and is independent of its history. Having discrete states, such that the system can be in state α or state β, allows for the dynamics of the system to be described by the master equation:[184]

$$\frac{dP_\alpha}{dt} = \sum_\beta \left[W_{\alpha\beta} P_\alpha - W_{\beta\alpha} P_\beta \right] \tag{2.29}$$

This expresses the probability of finding the system in a particular state (P_α) at a given time (t) as well as a transition probability ($W_{\alpha\beta}$) which describes the rate of moving from state α to β and vice versa.

Considering transport of a single charge in a given system, a state is then represented as an occupied site, i.e., the site on which the charge carrier sits. The equivalent equation can then be written in terms of the site occupation probabilities (p_i) and the charge transfer rates (ω_{ij}) between two sites, i and j:

$$\frac{dp_i}{dt} = \sum_j \left[\omega_{ij} p_i - \omega_{ji} p_j \right] \tag{2.30}$$

For charge transport simulations, the rates in equation (2.30) are the calculated Marcus hopping rates. Used in combination with the molecular centre of mass positions, to give the hopping sites and nearest neighbours to give each potential transition ($i \rightarrow j$), described in section 2.3.2. The unknown occupation probabilities, then have to be determined. For a single charge carrier expressed by the first order linear differential master equation (2.30), it is possible to use an analytic approach for certain cases, however this has several limitations and systems with a large number of molecular sites already become problematic. Therefore, a method of solving the master equation, which can account for large system sizes is required (typically, this is in the order of several thousand molecules for charge transfer simulations).

Additionally, when multiple charge carriers are treated, which is a valuable consideration for realistic systems, the master equation becomes much more complex. In this case, there is not only one occupied site, but several, resulting in non-linear differential equations and requiring

more complicated algorithms in order to solve them. With regard to including multiple charge carriers and the correlation between the occupation probabilities of the various sites, a kinetic Monte Carlo algorithm is considered.

2.3.9 Kinetic Monte Carlo

Kinetic Monte Carlo (KMC)[185–190] is one way of solving the master equation and providing the time evolution of the system, giving a randomly generated trajectory of charge carrier movement. The task of KMC is to accurately move from one state of the system to another, generating a sequence of events with the correct probabilities.[184] The premise of this approach is that there are infrequent events or occasional transitions from one site to another, amid large static periods (no carrier hopping). This can ensure that the method utilises a Markov chain, with transitions independent from previous events. The KMC algorithm discussed in this section considers multiple charge carriers, with accurate computation of their charge transfer using the Marcus hopping rates, also ensuring no doubly occupied hopping sites, followed by the extraction of their trajectory for charge carrier mobilities. KMC thereby implements the stochastic propagation through time, with respect to the selection of these charge transfer events and their computed rates.

Firstly, considering a system with N hopping sites (centre of mass positions), followed by the random injection of a charge carrier (electron/hole) to site i. The occupied site (i) is now an 'enabled' site, such that it can contribute to the charge transfer description. This site has a certain number of nearest neighbours (m), as specified in the neighbour list (Section 2.3.2), which, as a pair, can take part in a charge transfer reaction, with rate specified by the Marcus rate equation. The number of neighbours is known as the coordination number of the site. An escape rate (ω_i) can then be defined as the sum of all hopping rates (ω_{ij}) moving away from site i:[2]

$$\omega_i = \sum_{J=1}^{m} \omega_{ij} \tag{2.31}$$

The hopping event probability is proportional to the escape rate, such that the event is chosen with a weighted proportionality to the other events. As an example, the occupied site i has four neighbours, and four corresponding hopping rates (ω_{ij}, ω_{ik}, ω_{il}, ω_{im}). In order to make a

random choice of which site this carrier will hop to, each hopping rate has to be weighted proportionally to the escape rate, as depicted in Figure 2.5.

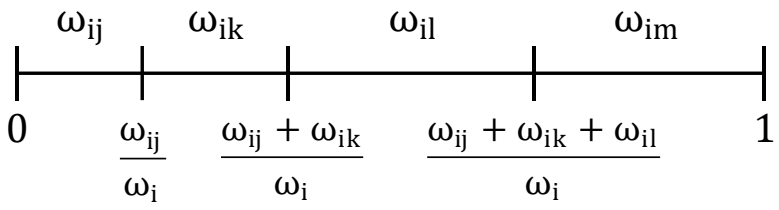

Figure 2.5 Proportional probabilities for selection of a hopping event from site i, with four possible events, with rates (ω_{ij}, ω_{ik}, ω_{il}, ω_{im}). The proportion of each hopping event corresponds to its rate, within the interval of (0,1], ω_i represents the escape rate of site i, from equation (2.31).

A random number is then generated in the interval of (0,1] and where this number lies on the scale of Figure 2.5, determines which destination site is chosen. As only one charge carrier is currently present, this choice will be an allowed event and therefore, it results in a hop from site i to the chosen neighbouring site. After a hop, site i is then 'disabled' and the newly occupied site becomes 'enabled'.

Multiple charge carriers

When considering multiple charge carriers within the system, the possibility of two charge carriers occupying one site has to be accounted for. To address this, one option would be to include coulomb interaction, repelling like charges. However, this approach is computationally expensive as it requires recomputing the Marcus rates at every KMC step, due to the variation of site energy differences as a result of changing site occupations, discussed further in Chapter 5. A second simpler approach uses the exclusion principle,[*] which simply states that no two like charges will occupy the same site at the same time. This is an adequate choice for the treatment of double occupation as two electrons (or holes) occupying the same site is virtually impossible, due to the strong columbic repulsion they would experience. If a site is occupied and a hopping event attempts to doubly occupy this site, this will be a so-called 'forbidden'

[*] referenced to an adapted Pauli exclusion principle, despite the fact that electronic spin is not considered here

event, otherwise, when the site is free the hop is allowed. By making use of this exclusion, the KMC algorithm then has to enable or disable events, based on the recognition of an allowed or forbidden event.

To bring this to a realisation, a variable step size method (VSSM)[184,190] can be effectively utilised for KMC for increased computational efficiency, specifically true for charge transport with multiple charge carriers. Here, an example of a two-level VSSM algorithm allows for a more practical approach, with the separation of hopping sites and possible hopping events from these sites. The VSSM approach allows for easier control of disabling and enabling events, as well as efficient updating of the cumulative rates, without having to recalculate all rates in the system.

A site is termed 'enabled' when it is occupied by a charge carrier, as previously described for one carrier. Consequently, the hopping events from this site are all enabled until there is a failed hopping attempt, due to the fact that the destination site is already occupied, this 'disables' the event and removes its rate from the hierarchal accumulation of rates. A depiction of a two-level VSSM tree is shown in Figure 2.6. A head node at the top of the tree, contains information about the entire system, the cumulative rates of all enabled hopping sites and enabled hopping events. The first level is constructed from the hopping sites, such that the number of nodes on this level equals the number of sites in the entire system. The first level nodes each have a cumulative rate made up of their subordinate hopping event rates. The second level, under the corresponding hopping site, contains all events hopping away from this site. As an example, the first level may be site i, the second level will be events for the hops i→j, i→k, i→l and so on. The random choice of which carrier will hop and subsequently, the destination to which it will hop, are done in the same manner as Figure 2.5, using proportional probabilities based on the rates. First a charge carrier is randomly chosen (e.g., carrier on site i), based on its occupied site escape rate (ω_i), equation (2.31), i.e., the sum of all hopping events from the site. The probability (P_i) of this carrier escaping site i and hopping to another site is then given by:

$$P_i = \frac{\omega_i}{\sum_n \omega_n} \tag{2.32}$$

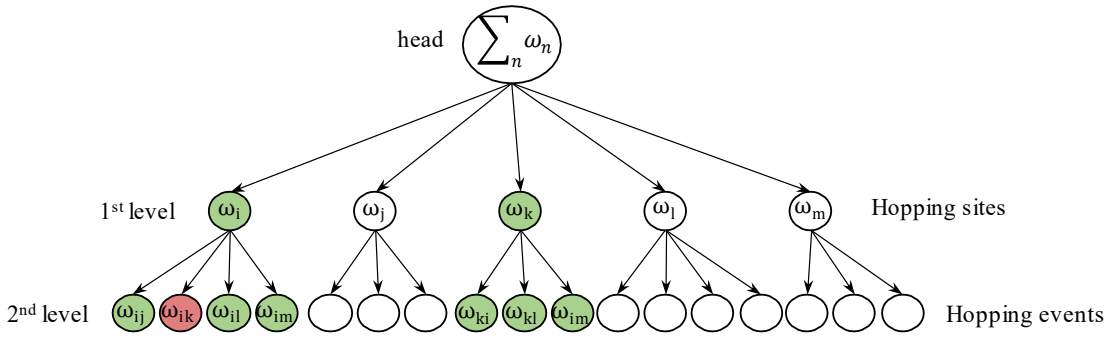

Figure 2.6 Representation of the VSSM hierarchical construction. The head of the tree contains all cumulative rates of all 'enabled' sites (n) and their corresponding 'enabled' events. The first level under the head, is constructed from all hopping sites in the system, 'enabled' when occupied by a charge carrier (green), they contain the cumulative rates (e.g., (ω_i)) of all 'enabled' events from this site (green). The second level corresponds to events (hops) from each site to a neighbour, with a given rate e.g., ω_{ij}. After a forbidden event has occurred (e.g., hop attempt i→k), the event becomes 'disabled' (red) and its rate is removed from the cumulative rate (ω_i) for the site and consequently the head cumulative rate.

Where n is the total number of occupied sites and ω_n is their escape rates. Once the carrier on a site is selected, the second choice of which destination is then randomly selected, based on the individual hopping rates, with a probability of hop, for example i→j given by ω_{ij}/ω_i. If this chosen hop is possible, it is carried out, thereby disabling the initial site 'i' (and disabling all events from this site) and enabling the new site 'j' (and enabling all events from this site). Contrarily, if the chosen destination is already occupied by a carrier, then this site becomes a forbidden event and the carrier stays on the initial site, only disabling the attempted event. After this, with the newly updated cumulative rate, based on new enabled/disabled events or a newly enabled site, the procedure continues and the next time update takes the system into the proceeding events. With each KMC step there is a time increment (Δt), defined as the interval when no charge transfer occurs, i.e., the time in which the system remains static. This is related to the cumulative rate of the whole system ($\sum_n \omega_n$), and generated by choosing a random number (r) from a uniform distribution within the interval (0,1]. Δt is calculated according to equation (2.33).

$$\Delta t = -\frac{1}{\sum_n \omega_n} \ln(r) \tag{2.33}$$

For clarity, the algorithm for the two-level VSSM KMC for multiple charge carriers, implementing the exclusion principle for double occupation of sites is shown in Figure 2.7.

Firstly, a known system morphology with the necessary parameters: hopping sites, neighbour list and Marcus rates, is required as the input. 'N' charge carriers are then injected randomly onto 'n' hopping sites and the time is updated according to their escape rates, with equation (2.33). A carrier on site i is then randomly chosen, with the probability according to equation (2.32). This is followed by the random selection of the destination, with probability relative to the escape rate of the site. If the hop is allowed, as show in 5(a) case 1 of Figure 2.7, then the carrier hops to its destination site, disabling its initial site and enabling the new site. If the hop is forbidden as in 5(b) case 2 of Figure 2.7, the carrier remains on the initial site and disables this event. In the instance of case 6(a) or 6(b), the algorithm returns to the time update, with the newly enabled or disabled site or event and proceeds in this manner, until the stop condition is met. The stop condition for this algorithm can be a specified number of KMC steps, or a specific runtime, this generally depends on the input used.

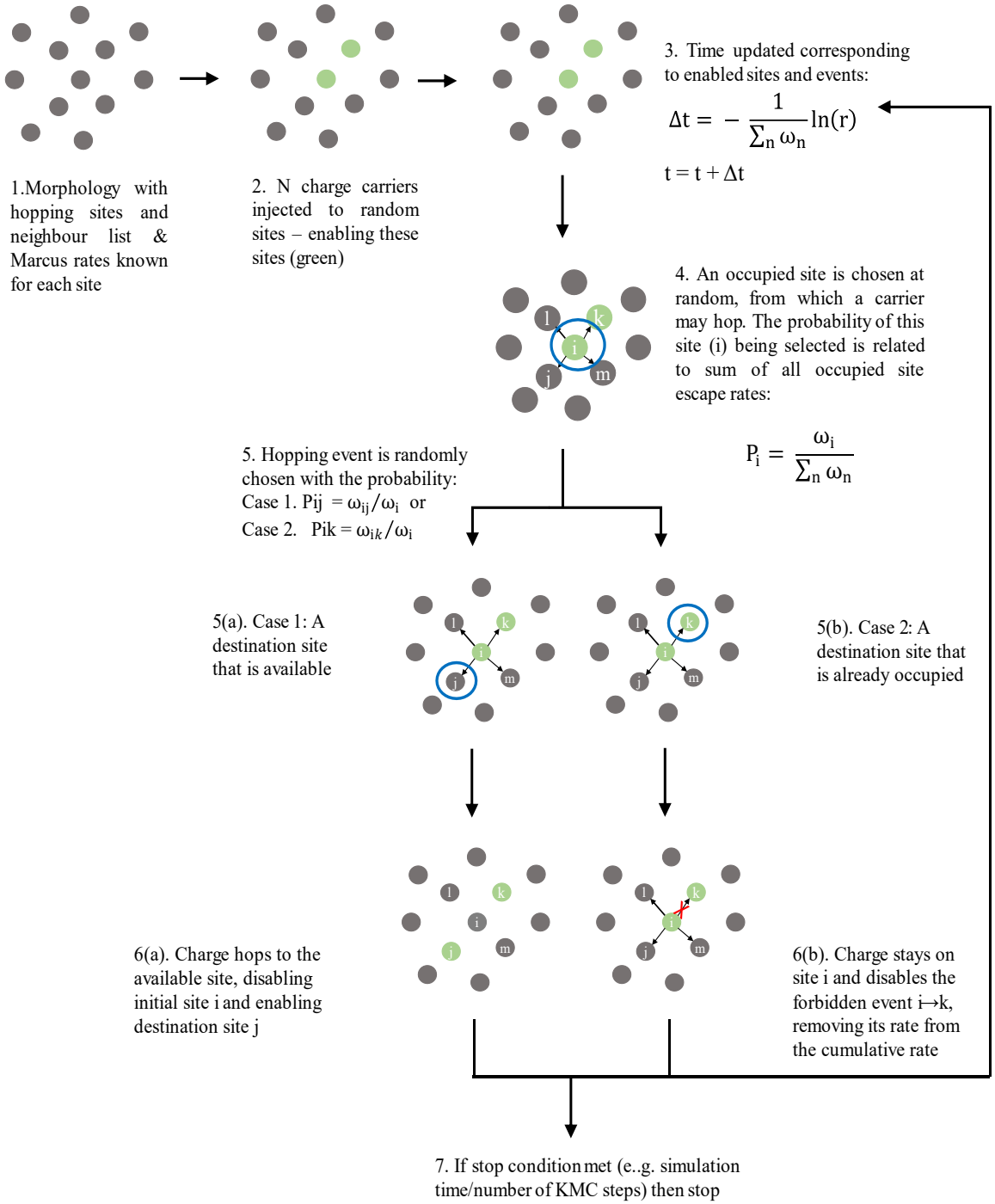

Figure 2.7 Workflow for the two-level VSSM KMC algorithm for multiple charge carriers, implementing the exclusion principle for forbidden double occupation of sites.

2.3.10 Charge carrier mobility

Carrier mobility is an essential result of the charge transport simulations, as it can be directly compared to experimentally obtained mobility values, using for example, time of flight (TOF) or space charge limited current measurements (SCLC). For simulations, the mobility is achieved after solving the master equation, by the implementation of the KMC algorithm. This can be obtained by using the trajectory of the carriers, generated by KMC to directly calculate the mobility tensor from the carrier velocity and magnitude of applied electric field. After an adequate KMC simulation time (for equilibration), corresponding to the energetic disorder of the system,[*] the converged charge carrier mobility can be obtained. The average carrier velocity $\langle\vec{v}\rangle$ is calculated as the displacement vector ($\Delta\vec{r}$) over simulation time (t) and the mobility (μ) is calculated using the average velocity with respect to the applied electric field ($\vec{F}$), according to:

$$\langle\vec{v}\rangle = \frac{\Delta\vec{r}}{t} = \mu\vec{F} \tag{2.34}$$

2.3.11 Finite size effects

System size plays an important role in the description of certain macroscopic properties of amorphous organic materials, such that mobility values become system-size dependent.[†] Charge transport simulated by small system sizes (with several thousand molecules) with large energetic disorder, will most probably exhibit dispersive transport at low temperatures.[192–194] These systems are in the order of several nanometres in dimension, compared with the micrometre systems studied experimentally. The variation in system size, accounted for by computational cost, means that the transport is dispersive in the small simulated system and non-dispersive in the large experimental system. The consequence being that simulated charge mobilities can vary significantly from experimental achieved mobilities, in an example of finite size effects.

[*] Systems with large energetic disorder require longer KMC simulation times for the mobility to converge

[†] The variation with thin-film thickness has also been shown experimentally[191]

In order to combat this, there is an empirical correction, involving a temperature extrapolation procedure,[194] providing a method of extracting non-dispersive mobilities from small systems with dispersive transport. Here, the system has to be simulated at high enough temperatures, where transport moves from the dispersive regime into the non-dispersive. This transition temperature (T_{ND}) can be calculated knowing the number of hopping sites in the system (N) and the site energy distribution (σ), using equation (2.35).*

$$\left(\frac{\sigma}{k_B T}\right)^2 = -5.7 + 1.05 \ln N \tag{2.35}$$

With the transition temperature known, KMC simulations are then run with higher temperatures (in a very broad range, e.g. 1000K-50000K), achieving non-dispersive (temperature dependent) mobilities with the following equation:[195]

$$\mu(t) = \frac{\mu_0}{T^{3/2}} \exp\left[-\left(\frac{a}{T}\right)^2 - \left(\frac{b}{T}\right)\right] \tag{2.36}$$

The material constants, μ_0, a and b, are typically extracted as fitting parameters, upon the fit of equation (2.36) with the obtained mobilities at the chosen temperatures. The fitting procedure then allows for the extrapolation from this high temperature regime to experimentally relevant temperatures (in and around room temperature). In doing so, non-dispersive mobility values can be extracted, for example at 300K and directly compared to experimental results.

* The derivation and full discussion of dispersive to non-dispersive mobilities can be found here[194]

3 Unicoloured phosphor-sensitised fluorescence*

Achieving a blue OLED, which is both efficient and stable, has proven to be problematic. The challenge originating with the limitations of the blue emitter: if operational lifetime is prioritised, stable fluorescent emitters can be used. Their efficiency, however, is limited by unfavourable spin statistics. To improve efficiency, phosphorescent emitters can be used. Their large coupling between the exciton spin and the orbital angular momentum allows for radiative decay from the triplet state to the ground state. Additional to this, the spin-orbit coupling allows for intersystem crossing to occur, such that the singlet excited state can also populate the triplet state, helping to achieve almost 100% internal quantum efficiency. The drawback of this highly efficient system is the long lifetime of the triplet state, typically in the order of several microseconds (much longer than the nanoseconds fluorescence lifetime), which leads to degradation of the organic material.[197] Since stability is highly important, in order to achieve a long-lived consumer product, fluorescent emitters are the chosen source of blue OLEDs. But, with battery life on portable devices being the cost of this inefficiency, it is vital that the blue OLEDs become more efficient.

Thermally activated delayed fluorescence (TADF)[198–203] is one of the existing approaches targeting the OLED efficiency, where a reverse intersystem crossing, from triplet to singlet, is achieved. Combination of TADF and conventional fluorescence emitters, in a sensitising approach is also a possibility.[204,205] However, the decay times of TADF systems are similar to that of a phosphorescent only system,[206,207] meaning that a short-lived OLED is inevitable.

A phosphor-sensitised fluorescence approach,[208–212] offers an alternative to TADF OLEDs, by utilising a donor-acceptor concept with a phosphorescent donor and a fluorescent acceptor. In

* Adapted from the publication: Perspectives of Unicoloured Phosphor-Sensitized Fluorescence L. Paterson, A. Mondal, P. Heimel, R. Lovrincic, F. May, C. Lennartz, D. Andrienko; Adv. Electron. Mater. **2019**, 5 (12), 1900646 DOI: 10.1002/aelm.201900646[196]

addition to phosphorescence and fluorescence, energy transfer can occur between the donor and acceptor molecules, either via short-range Dexter or long-range Förster resonance energy transfer (FRET). FRET takes place from the donor triplet to the acceptor singlet, allowing for fluorescence.[213] This approach leads to shorter radiative decay times, in comparison to phosphorescent only emitters, as recently demonstrated by Kim et al,[214] where a significant reduction of radiative decay time was shown for a green phosphorescent emitting donor and yellow fluorescent emitting acceptor.

Classic sensitisation for an efficient fluorescent blue OLED would require a sensitising donor emitting in the UV spectral range and red-shifted (with respect to the donor) acceptor emission. This approach is not suitable for devices, as high exciton energies would result in very fast device degradation. On the other hand, if the fluorescent acceptor and phosphorescent sensitiser have matching emission spectra, the excitation energy required to pump the acceptor emission can be reduced. However, various practical design challenges have prevented the development of a unicoloured sensitised emitting system, until now. As the donor emission and acceptor absorption overlap is significantly reduced in a unicoloured system, compared to a non-unicoloured system, a result of large reorganisation energies of the organic emitters upon excitation (Stokes shift), the spectral overlap of the unicoloured system is then limited by the Stokes shift of the acceptor.

These challenges have been resolved in a recent study by Heimel et al., where a unicoloured phosphor-sensitised fluorescence (UPSF) approach, for an efficient and stable blue OLED was investigated.[215,216] The donor, acceptor and host molecules and a depiction of the processes, with radiative decay times and singlet and triplet energy levels, are shown in Figure 3.1. The sky-blue emission colour is preserved, by matching the emission of donor and acceptor. The experimental results demonstrated a clear reduction in radiative decay, moving from a phosphorescent only system (1.60 µs) to a system with the inclusion of fluorescent acceptors (0.49 µs). Which in turn lead to a three-fold increase in device lifetime, from 26h to 76h, all of which is shown in the experimental evidence section 3.1.

The drawback of the sensitising approach is the Dexter energy transfer, from the triplet of the donor to the triplet of the acceptor, by which a loss in efficiency arises. As the acceptor molecule is not of TADF-type, there is no reverse-intersystem-crossing (RISC) present. Therefore, Dexter triplet-triplet energy transfer results in quenching, since the transferred triplet state cannot decay radiatively, neither directly from the acceptor triplet, nor through a

RISC-process with subsequent delayed fluorescence. Unfortunately, with increasing acceptor concentration, the probability of Dexter transfer increases. As a result, the photoluminescence quantum yield (PLQY) is shown to be directly linked to the concentration of the acceptor, with a decrease from 100% (no acceptors) to 63% (1.5 volume % acceptor molecules) shown experimentally. Therefore, the UPSF OLED has to be designed in such a manner as to (i) optimise the acceptor concentration for increased lifetime and (ii) target donor-acceptor combinations with slow Dexter and fast FRET rates, for increased efficiency.

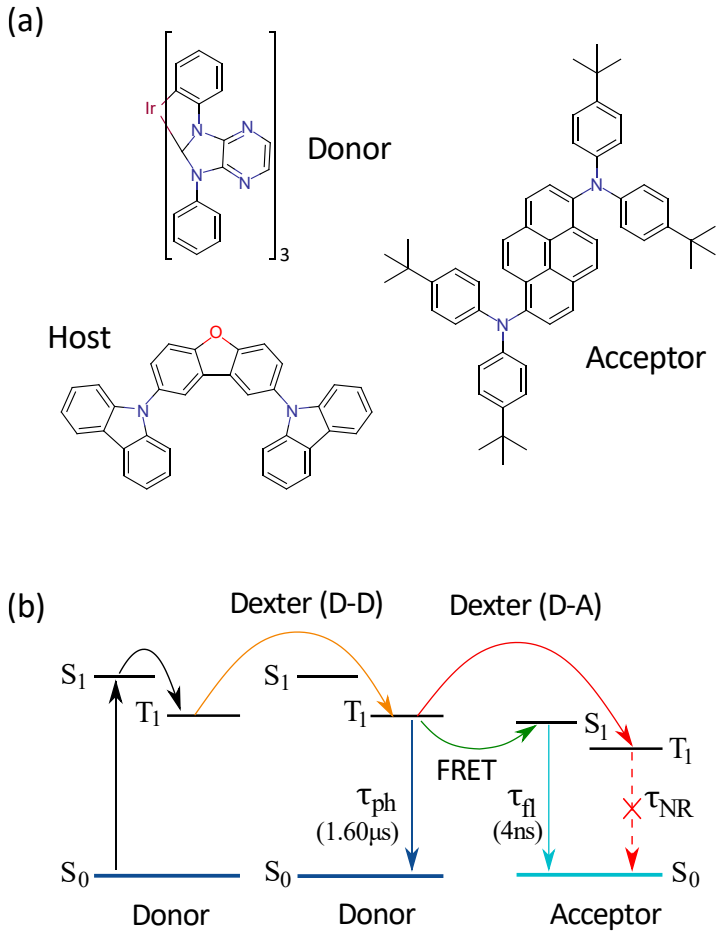

Figure 3.1 (a) Molecular structure of the donor, acceptor and host, used to bring the UPSF concept to a realisation (b) Energy level diagram of the UPSF system. Essential energy transfer, radiative (experimental decay times shown) and non-radiative decay: Initial excitation of the donor, donor to donor transfer (D-D), phosphorescent decay from the donor triplet (Ph), FRET from the triplet of the donor to the singlet of the acceptor, followed by fluorescent decay (fl) and Dexter energy transfer from the triplet of the donor to the triplet of the acceptor, followed by non-radiative decay (NR).[196]

To provide further insight into this novel concept and quantify its potential, it is necessary to develop a multiscale model of a UPSF OLED. Beginning with atomistic morphologies and progressing to the parametrisation of each rate of all of the essential processes involved and solving the respective master equation with the help of a kinetic Monte Carlo algorithm. The rates of the individual energy transfer processes are adjusted according to the experimentally measured photoluminescence quantum yield (PLQY), phosphorescent-fluorescent emission ratios, time resolved photoluminescence (TRPL) spectra, and radiative decay times. Once developed, the multiscale model can then be utilised to expand on the scope of experiment, by examining further acceptor concentrations, as well as the FRET and Dexter energy transfer rates. Simulations can then highlight the fundamental efficiency and decay time limits of the UPSF system. The simulation workflow, as it is described, is depicted in Figure 3.2.

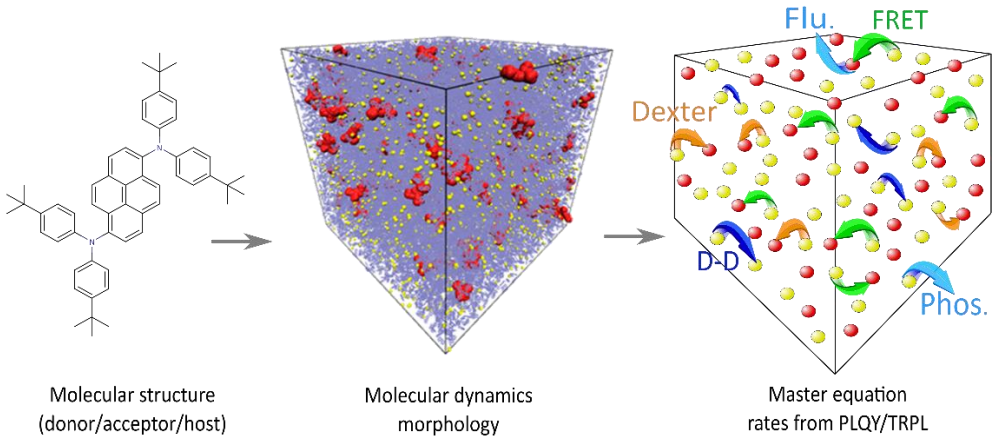

Figure 3.2 Simulation workflow: initial molecular structures are used to construct a morphology for molecular dynamics simulations, followed by rate parameterisation from experimental data, then KMC to randomly propagate the system through time. This provides OLED properties such as photoluminescence quantum yield (PLQY) and radiative decay times and plots such as those achieved by time resolved photoluminescence (TRPL).[196]

3.1 Experimental evidence

The experimental evidence outlined here, which is required for the progression to a computational investigation was taken from the original experimental study of the blue UPSF OLED.[215,216] Three UPSF systems were studied with varying acceptor concentration: 0.5, 1.0 and 1.5 volume % acceptor, within a mixed layer also containing the donor and host. Additional

to a donor only system and an acceptor only system, providing the radiative decay times of phosphorescence and fluorescence respectively. A combination of UV-Visible, steady-state and TRPL spectroscopies were utilised to extract the UPSF properties.

Firstly, in order to ensure that the predominant excitation was in fact donor molecules and not direct acceptor excitations, the wavelength of the laser was adjusted. This had to be within the maximum of donor absorption and as close as possible to the minima of the acceptor absorption. Of course, within the optical excitation experiments, it is not possible to guarantee donor excitation exclusively. Therefore, the aim is to select an excitation wavelength to keep direct acceptor excitation negligible, this was found to be 375 nm. The calculations from absorption coefficients showed that in fact donor molecules absorbed 95, 47 and 32 times more of the light than the acceptor molecules, for the 0.5%, 1.0% and 1.5% acceptor concentrations respectively.

The FRET radius, the distance at which 50% of the donor excitations are transferred via FRET to the acceptor, was estimated to be 2.4 nm. This was achieved from the spectral overlap integral of the extinction spectrum of the acceptor and the normalised photoluminescence spectrum of the donor. This is a smaller value than the typical FRET radius of a non-unicoloured system, typically around 4-5.5 nm,[208,217–219] which is a result of the smaller spectral overlap.

In order to observe the effect of increasing acceptor concentration on the UPSF properties, TRPL experiments were carried out. TRPL is utilised to measure the radiative decay of a sample upon an initial excitation by a short light pulse. The emitted photons from the sample are measured as a function of time, providing information regarding the decay times of the emission, be that fast fluorescence or slow phosphorescence. For the donor only system, (0% acceptor) a (phosphorescence) radiative decay time of 1.60 µs was extracted from the TRPL spectra. Similarly, for the acceptor only system, a radiative decay time of 4 ns for fluorescence was extracted. For the varying donor-acceptor combinations, ranging from 0% to 1.5% acceptor, the TRPL spectra are shown in Figure 3.3, fitted with a multi-exponential fit to achieve the radiative decay times. The 0% acceptor concentration (black) providing the radiative decay time for phosphorescence of 1.60 µs, followed by 1.06 µs (red), 0.77 µs (green) and 0.49 µs (blue) for the 0.5%, 1.0% and 1.5% acceptor concentrations, respectively.

The shift in radiative decay times signifying the shift from slow phosphorescence to faster fluorescence. As a result of more FRET events from the donor to the acceptor, due to increased numbers of acceptors. Additionally, the PLQY values for each of the concentrations can be extracted. As expected, the PLQY for the donor only system was found to be ~100%, where there are no energy transfer pathways leading to efficiency losses. As the acceptor concentration is increased, the PLQY gradually decreases, as a result of increased Dexter energy transfer from the donor to the acceptor, where the excited triplets are trapped and quenched, resulting in a loss of efficiency. PLQY values of 82%, 66% and 63% resulted from the 0.5, 1.0 and 1.5% acceptor concentrations, highlighting the detrimental impact of Dexter transfer.

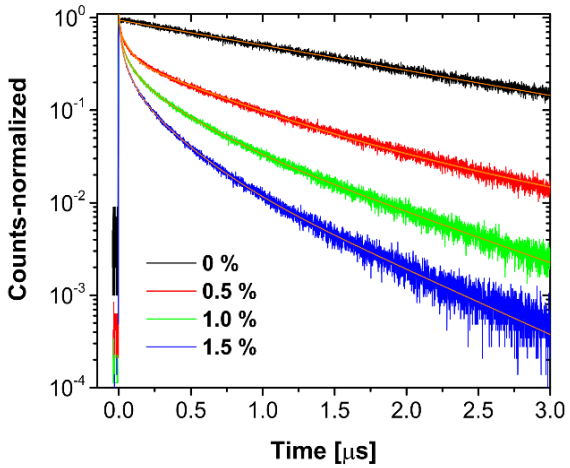

Figure 3.3 TRPL-experimental results for the UPSF system. Samples excited at 375 nm to suppress direct acceptor excitation. The acceptor concentration was gradually increased from 0% (black) to 1.5% (blue). The decays were fitted with a multi-exponential fit (red lines) to derive the mean (intensity weighted) radiative decay time. This figure is taken from the experimental work.[215]

To break the emission down further, in order to directly observe the shift from phosphorescence to fluorescence, the normalised electroluminescence and photoluminescence spectra and the donor-acceptor coefficients with respect to concentration are shown in Figure 3.4. Illustrating that the emission peak width narrows with increasing acceptor concentration, is moving towards the acceptor only system (BA-only). Proving that part of emission is indeed obtained from the acceptors.

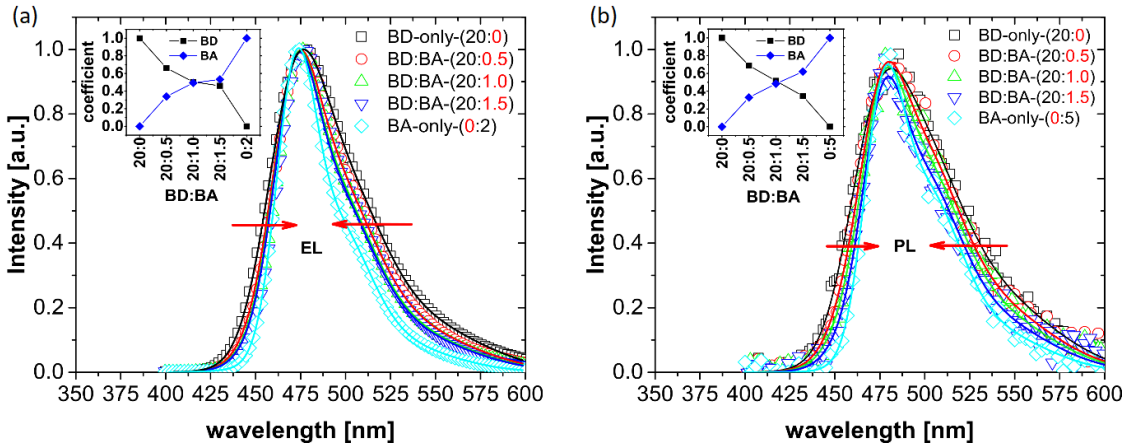

Figure 3.4 UPSF characteristics for the various donor-acceptor concentrations studied, from 0% to 1.5% acceptor and the acceptor only system. (a) Normalised electroluminescence spectra and (b) Normalised photoluminescence spectra, the insets show the donor-acceptor coefficients with respect to concentration. This figure is taken from the experimental work.[215]

To estimate the ratio of phosphorescence to fluorescence, the normalised spectra of the donor only and acceptor only samples were fitted with three gaussians, and the linear combinations were used to reproduce the mixture spectra. The insets of Figure 3.4 show the shift from donor emission (phosphorescence) to acceptor emission (fluorescence) as a ratio between the two, with increasing acceptor concentration. For example, the 1% acceptor concentration, sees roughly a 50/50 emission divide, between phosphorescence and fluorescence. As direct acceptor excitation is limited, as previously described, this shift from phosphorescence to fluorescence is a clear indication of the presence of FRET and that the energy transfer from donor to acceptor does in fact occur.

Finally, the LT70 (luminance decreases to 70% of its initial value) lifetime of the UPSF OLED, was measured experimentally for each acceptor concentration, for two conditions: (i) at the same initial current density (25mA/cm2), and (ii) at the same initial luminance (4000cd/cm2). These were then compared to the relative radiative decay rate (inverse of radiative decay time), as a function of acceptor concentration, shown in Figure 3.5.

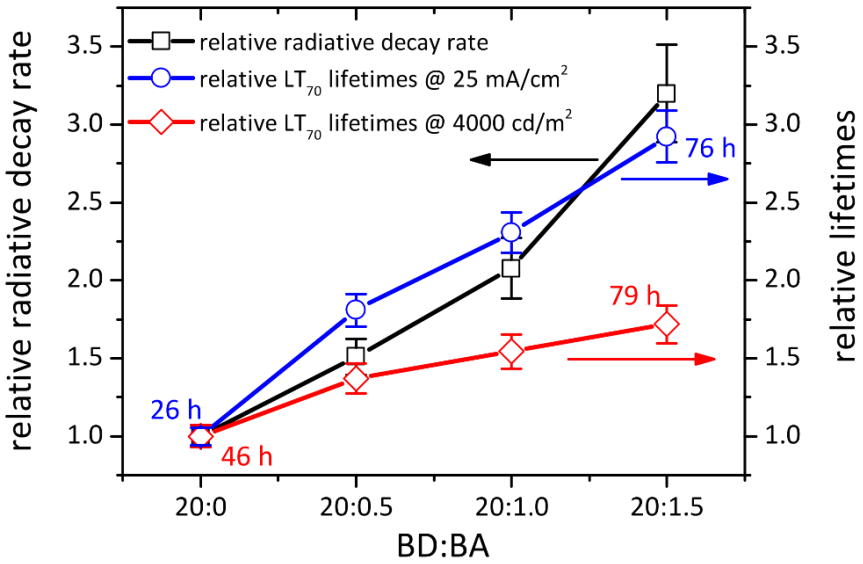

Figure 3.5 Correlation between the radiative decay rate and OLED lifetime. Relative radiative decay rates (black) are compared to relative lifetime values (70% decay, LT 70), for each of the donor-acceptor concentrations. The device lifetimes were measured at constant current, with initial current density of 25mA/cm^2 (blue) and initial luminance of 4000cd/m^2 (red). This figure is taken from the experimental work.[215]

From Figure 3.5, for the 1.5% acceptor concentration, there is a significant correlation between the relative increase of the radiative decay rate (black) and the increase of device lifetime (blue). Signifying that the shift from slow phosphorescence to fast fluorescence, resulting in an overall lower radiative decay time (higher rate), does dramatically improve the device lifetime, by a remarkable factor of three. For the initial luminance of 4000cd/m^2 (red) there is a decrease in current-efficiency, resulting in the more moderate increase over the range of acceptor concentrations. This is due to a higher current being required to reach this initial luminescence, a result of lost excitation from Dexter transfer to the acceptor. Nevertheless, the correlation between relative radiative decay rate and device lifetime, signifies a stability increase as the acceptor concentration is increased, a result of moving away from the long-lived donor triplets, towards short-lived acceptor singlets. That being said, the Dexter transferred excitons which populate the acceptor triplet must not be overlooked, as they contribute to the long-lived excited states, which is a mechanism for faster device degradation. Therefore, in order to maximise the output of UPSF, the suppression of Dexter energy transfer is essential.

3.2 UPSF energy transfer processes

All processes of interest within the UPSF OLED begin with an initial excitation of donor molecules: S_0^{donor} to S_1^{donor} and as initial excitation of the acceptor molecules was limited experimentally, as discussed in the Experimental evidence section, it was not included in the simulations. This is followed by a practically instantaneous transition from S_1^{donor} to T_1^{donor}, populating the first triplet T_1 state of the donor molecule, as shown in Figure 3.1 (b). There are then a number of possibilities, firstly, triplet excitation can decay radiatively, T_1^{donor} to S_0^{donor} (phosphorescence). Secondly, the donor triplet can be transferred from one donor molecule to another, with a rate k_{DD}, via a Dexter energy transfer. As it is Dexter in nature (short range), it can be assumed that this rate decays exponentially as the donor-donor separation (R_{DD}) increases:

$$k_{DD} = k_{DD}^0 e^{-\alpha_{DD} R_{DD}} \tag{3.1}$$

Additionally, the donor triplet can undergo an energy transfer from donor to acceptor, either via the Dexter or Förster mechanism. For short range Dexter energy transfer, T_1^{donor} to $T_1^{acceptor}$ an exponential decay is again assumed, with increasing donor-acceptor separation (R_{DA}):

$$k_{Dexter} = k_{Dexter}^0 e^{-\alpha_{DA} R_{DA}} \tag{3.2}$$

This results in non-radiative decay from the $T_1^{acceptor}$ state, the rate of which is unknown from experiment. For donor-acceptor pairs at separations larger than 1 nm, FRET is the predominantly chosen pathway for the transition T_1^{donor} to $S_1^{acceptor}$ resulting in the fluorescent radiative decay $S_1^{acceptor}$ to $S_0^{acceptor}$. Assuming that the FRET rate depends on k_{ph} the inverse of the phosphorescent decay time (lifetime of the donor excited state),[213,220,221] the relationship to the Förster radius (R_{FRET}) and the donor-acceptor separation is as follows:

$$k_{FRET} = k_{ph} \left(\frac{R_{FRET}}{R_{DA}} \right)^6 \tag{3.3}$$

Experimentally, three acceptor concentrations were investigated: 0.5, 1.0 and 1.5 volume % acceptor molecules. In addition to a donor only system and an acceptor only system, providing the radiative decay times of phosphorescence (1.60 µs) or fluorescence (4 ns), respectively. The inverse of the phosphorescence decay time yields the rate $k_{ph} = 6.25 \times 10^5\ s^{-1}$. The Förster

radius of the given donor-acceptor pair, was also estimated experimentally, with a value of R_{FRET} = 2.4 nm. Utilising the available experimental data for each concentration (a PLQY value, a ratio of phosphorescence:fluorescence emission and a radiative decay time, with TRPL spectra), it is possible to utilise simulations to gain further insight and expand on the initial results.

The experimentally unknown rate constants for donor to donor energy transfer (k_{DD}^{0}), Dexter energy transfer (k_{Dexter}^{0}), and the non-radiative decay of acceptor (k_{NR}), can be determined. These rate constants represent averaged over assemblies of molecules quantities and hence are directly related to the atomistic-scale morphology.

3.3 Amorphous morphologies of ternary mixtures

The complex mixed molecular structure used in experiment must be translated to a structure which can be used for simulations, composed of available sites, between which energy transfer can readily occur. The system is composed of donor, acceptor and host/matrix molecules, with the donors and acceptors being the subject of investigation.

3.3.1 Molecular dynamics

For each of the molecules, shown in Figure 3.1 (a), the OPLS (Optimized Potential for Liquid Simulations) force field[222–225] was used for the Lennard-Jones parameters, with the combination rules and a fudge factor of 0.5 for 1-4 interactions. Missing improper and torsional potentials are then reparametrized based on QM scans.[226] Atomic partial charges of the acceptor, host and donor molecules were computed using density functional theory (wb97xd functional and 6-311+g(d,p) basis set), with the exception of the Ir atom in the donor molecule, for which a pseudopotential equivalent to the def2-tzvp basis set was used. Ground state optimization of isolated molecules were performed, with minimized configurations used to compute the electrostatic potential at the same level of theory and subsequently, atomic partial charges via the CHELPG[227] scheme using the Gaussian09[228] program.

The UPSF system with varying acceptor concentrations were initially simulated with molecular dynamics (MD), using the GROMACS[229,230] package. Using cubic simulation boxes, containing 3600 donor, 24000 host and between 80 to 480 acceptor molecules, as listed in Table 3.1. The individually optimised molecules were then uniformly distributed (ratios according to Table 3.1) and randomly orientated throughout the simulation box. The temperature of the mixture was then slowly raised, to equilibrate above the glass transition temperature (raised to 800K), before being quenched, with a quick decrease to 300K.

Experiment: volume % (acceptor molecules)	**Simulated: number of molecules**	
	Acceptor	Donor
0.5	80	3600
1.0	160	3600
1.5	240	3600
-	320	3600
-	400	3600
-	480	3600

Table 3.1 Molecular dynamics system specification: number of acceptor and donor molecules used in the simulations

3.3.2 KMC structure

The amorphous structure from MD simulations was then utilised to construct the KMC input structure. The MD structure containing all of the donor, acceptor and host molecules has to be converted to a simpler representation. For the purpose of KMC, the host molecules are not required, as there is no energy transfer to these molecules. Therefore, in the conversion to a KMC structure only donor and acceptors are considered. The centre of mass of each and individual donor and acceptor molecule is extracted, in order to build a neighbour list, defined as the list of molecules between which a hop may occur, within a specific cut-off distance. For the UPSF system, this varies for the type of molecule, such that there are donor-donor neighbours, as well as donor-acceptor neighbours. The cut-off distance for each of the pairs were altered to find an optimal value, for donor-donor (DD) pairs this was found to be 2nm, while the donor-acceptor (DA) pairs were within a 5nm distance (with the donor-acceptor

Dexter/FRET distinction being made with the KMC code itself). The distance variation, between DD and DA is due to the fact, that the spectral overlap between the donor emission and the acceptor absorption is much higher than the spectral overlap between donor emission and donor absorption, as found from experiment.

3.4 Respective master equations

Energy transfer through the UPSF system is described as a series of hops from one molecule to another. This may be a hop from donor to donor, donor to acceptor, or the collection of radiative or non-radiative decay. Each hop, also known as an event, then takes the system from an initial state, to a proceeding state, with a rate of transition. The master equation, which describes the probabilistic combinations of these states, makes use of the transition rates, in order to allow for time evolution of the system. KMC can then solve the master equation to generate a random trajectory of energy transfer pathways throughout the UPSF system. There is a master equation for each of the important states, namely the donor triplet (DT), the acceptor singlet (AS) and the acceptor triplet (AT) states. For each state the master equations are listed:

$$\frac{\partial p_{DT}}{\partial t} = Ip_{DT} - k_{FRET}p_{DT} - k_{Dexter}p_{DT} - k_{ph}p_{DT} \tag{3.4}$$

$$\frac{\partial p_{AS}}{\partial t} = k_{FRET}p_{DT} - k_{fl}p_{AS} \tag{3.5}$$

$$\frac{\partial p_{AT}}{\partial t} = k_{Dexter}p_{DT} - k_{Dex(NR)}p_{AT} \tag{3.6}$$

Each state has a probability of occupation, determined by each of the processes related to that state. For example, the donor triplet state (DT), depends on the probability of the state being initially populated (Ip_{DT}), the rate of FRET, the rate of Dexter and the rate of phosphorescence. The acceptor singlet (AS) and acceptor triple (AT), depend on the rate of FRET or Dexter, respectively. As well as how the state will decay, be that via fluorescence, in the case of AS, or via a non-radiative Dexter decay, in the case of AT. There is also a master equation for each of the collection events, as well as, the donor to donor events.

3.5 KMC algorithm for UPSF

The steps of the KMC code, from the initial excitation of donor molecules, to the collection of all photons are listed in Figure 3.6, as a workflow of the algorithm. Using the generated structure from MD simulations, the neighbour list is built. KMC is then initialised, with specified parameters, the initial number of excitations and stop condition. The algorithm utilises a two-level variable step size method (VSSM), to construct the framework of all possible events in the UPSF system. The individual sites (molecules) make up the first level, with each possible event from that molecule on the lower, second level. This hierarchical method allows for quick selection of sites and events, without having to recompute cumulative rates, for each site.

Injection of carriers to the initial number of random donor molecules, enables these sites and starts the KMC process. The time for a reaction to take place (Δt) is then generated, as a random increment, proportional to the cumulative rate. This must occur prior to the event taking place, before any newly enabled or disabled events impact the cumulative rate.[184] The time is then updated with the addition of the reaction time to the initial time ($t = t + \Delta t$). A site (i) is then randomly selected, based on the escape rate, $\omega_i = \sum_j \omega_{ij}$, followed by a random hopping destination (event $i \rightarrow j$). If the destination is the collection node, the energy is collected (phosphorescence / fluorescence / non-radiative decay) and the site is disabled. If the destination is a second available site, such that it is not in the excited state, the hop occurs, enabling the new site (j) and disabling the old site (i). If the new site is already in the excited state, this event is forbidden and disabled. The stop condition is then checked, after any event has occurred, if not met, a new reaction time is generated and the KMC loop continues. The output generated is the radiative and non-radiative decay and the corresponding simulation time.

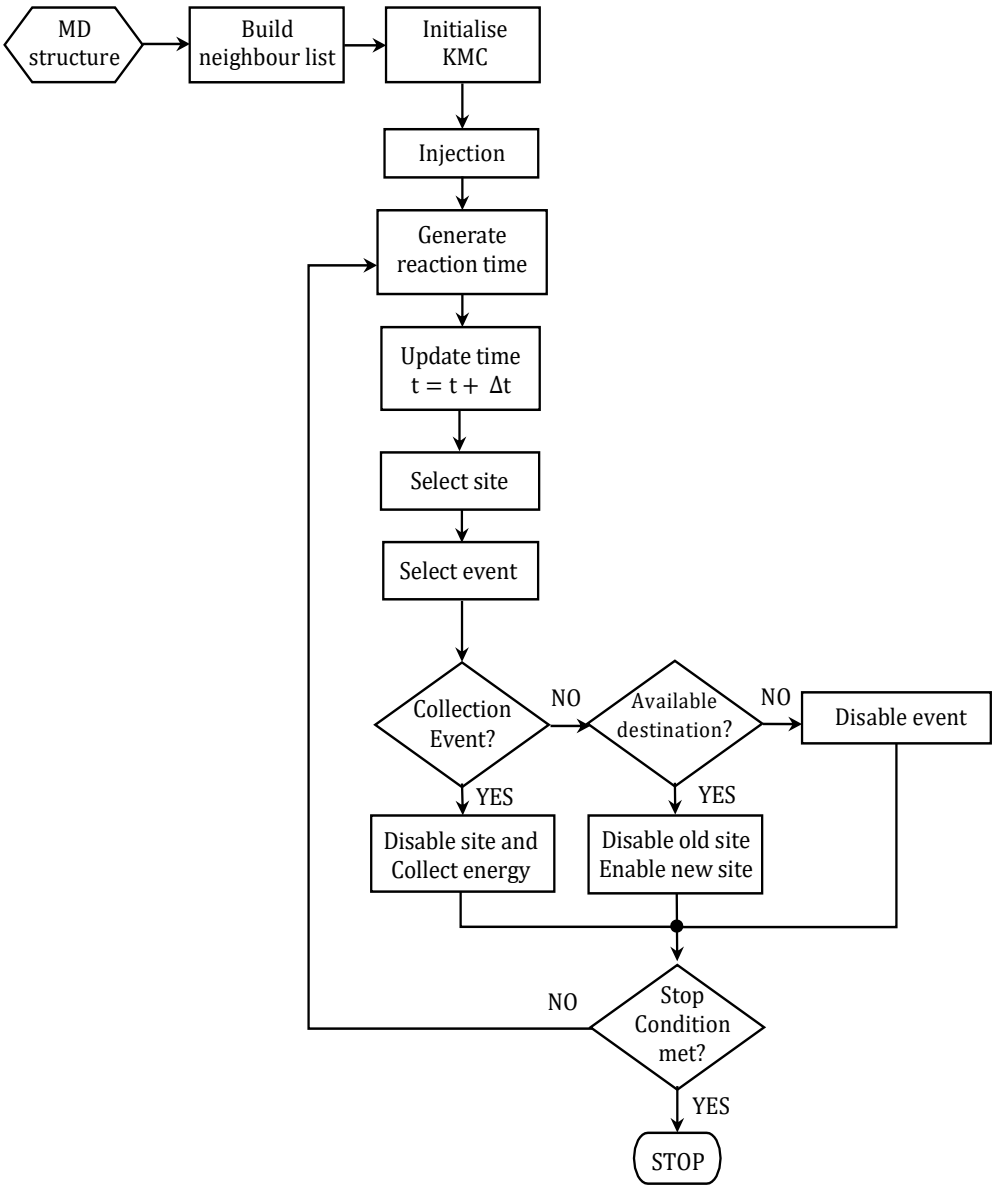

Figure 3.6 Kinetic Monte Carlo algorithm flowchart for the simulation of a UPSF system

3.5.1 Simulated photoluminescence spectra

Similar to the experimentally achieved time resolved photoluminescence (TRPL) spectra, a time dependent emission spectrum is obtained from simulations. This is done by counting the number of both fluorescent or phosphorescent photons, normalising the count and plotting at which time these photons were emitted, named as a simulation photoluminescence (PL)

spectrum, for each of the acceptor concentrations. The photoluminescence quantum yield (PLQY) obtained from simulations can then be directly compared to experiment. The PLQY value being defined as the number of emitted photons, in comparison to the absorbed photons, otherwise defined as the total collected radiative emission, compared to the total collected emission (both radiative and non-radiative):

$$\mathrm{PLQY} = \frac{\text{total emitted photons}}{\text{total absorbed photons}} = \frac{\mathrm{Phos.} + \mathrm{Flu.}}{\mathrm{Phos.} + \mathrm{Flu.} + \mathrm{Dex.}} \tag{3.7}$$

Similar to experimental TRPL data, simulation-PL data is fitted with a multiexponential fit. The multi-exponential fits of both data, allows for the direct comparison of the mean, intensity-weighted, radiative decay times. The fits are achieved with 3 exponentials, with the following the equation:

$$\mathrm{I(t)} = \sum_{\mathrm{i}=1}^{3} \mathrm{A_i} e^{-\frac{\mathrm{t}}{\tau_\mathrm{i}}} \tag{3.8}$$

The average decay lifetime, τ_d, is then calculated, by a direct extraction of the exponential fitting data:

$$\tau_\mathrm{d} = \frac{\sum_{\mathrm{i}=1}^{3} \mathrm{A_i}\, \tau_\mathrm{i}^2}{\sum_{\mathrm{i}=1}^{3} \mathrm{A_i} \tau_\mathrm{i}} \tag{3.9}$$

The radiative decay time is then gathered with a weighting relationship to the PLQY (Φ_{PL}) value:

$$\tau_r = \frac{\tau_d}{\Phi_{PL}} \tag{3.10}$$

Utilising all three equations, with the simulated PL data, the TRPL experimental values and the simulation values can be directly compared.

3.6 Parametrisation of rates

The KMC algorithm is then used to solve the master equations, in order to provide insight into the unknown rate constants of the UPSF system. This is achieved in a (controlled) trial and error manner, the unknown rate constants are initially estimated and then varied in accordance, until the experimentally achieved results have been reproduced.

3.6.1 Donor to donor transfer

It is unknown from experiment the extent to which donor to donor energy transfer plays a role in the overall description of the UPSF system. It quickly became apparent, by varying the rate constants of all donor-acceptor processes, in the absence of any donor-donor transfer, that there were large discrepancies in the PLQY and TRPL spectra of each concentration, when compared to experimental results. Therefore, the transfer of energy between donor to donor was an essential process to include for a quantitative description of the system. By fitting the TRPL spectra with and without taking into account the donor to donor transfer, it is possible to clearly observe the large impact it has on the overall description, shown in Figure 3.7 for the 1% acceptor concertation.

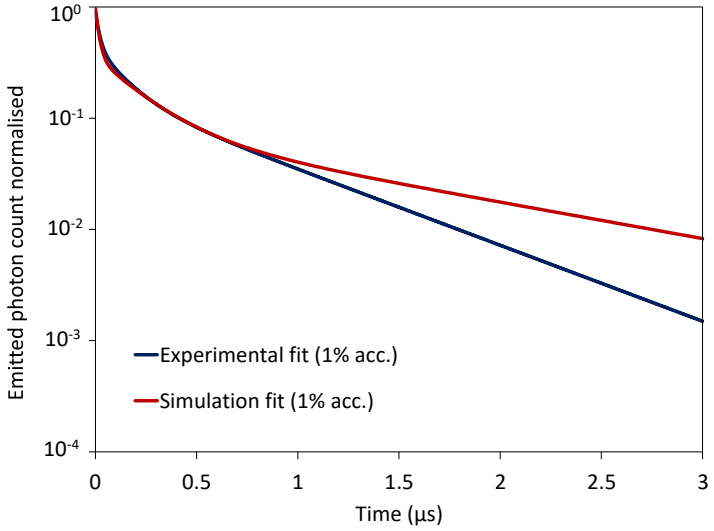

Figure 3.7 Simulated photoluminescence (PL) multi-exponential fit (red), with experimental TRPL multi-exponential fit (blue), for the 1% acceptor system.[196]

In the absence of donor to donor transfer, a donor molecule can (i) transfer energy via FRET or Dexter, if the acceptor molecule is within a given cut-off or (ii) radiatively as phosphorescence. Due to the ratio of donor molecules to acceptor molecules, there is a limited number of donor-acceptor pairs, which results in largely phosphorescence being observed. Confirmed by an overestimation of the radiative decay time, 1.44 μs (sim.) compared to the expected 0.77 μs (exp.), the variation is illustrated in Figure 3.7. By including donor to donor transfer, an initially excited donor molecule, which may otherwise only contribute to

phosphorescence, now has an additional possibility to transfer energy. Resulting in the required amount of FRET/Dexter events to represent the system accurately.

It is clear that donor to donor energy transfer cannot be omitted: short- and long-range decays cannot be reproduced simultaneously, with the estimated PLQY value higher than the experimentally achieved 66%, at 71%. Aside from this, the radiative decay time was almost double that of experiment. Signifying, insufficient donor-acceptor Dexter events and a shift to slower radiative decay, as a result of more phosphorescence than expected. Therefore, the intermediate process of donor to donor transfer, which would facilitate more FRET or Dexter events and lower the number of phosphorescent photons emitted, has to be included. The rate constant, k_{DD}^{0} was then varied, where an optimal value of around $5x10^{5}$ s^{-1} was found. This value ensures that donor to donor transfer is not the predominant energy transfer in the UPSF system, but allows for adequate movement of carriers between the donor molecules, in order to facilitate the required amounts of FRET and Dexter.

3.6.2 Donor to acceptor Dexter energy transfer

In combination with other rate constant variations, the donor-acceptor Dexter rate constant was varied, as this Dexter rate constant increases, the PLQY value decreases (as expected). Hence, to match the correct PLQY values with experiment would appear to be rather simple. Despite this, the difficulty in accurately reproducing experimental emission is with the ratio of phosphorescence to fluorescence. If the Dexter rate is too fast, there are limited FRET events and so limited fluorescence emission. On the other hand, if the Dexter rate is too slow, there is much more FRET events than predicted experimentally. It is for this reason that a further quantity, the Dexter cut-off has to be examined. This is defined as the maximum separation distance at which Dexter may occur. It is intuitive that the separation associated with Dexter must remain short, due to the nature of Dexter transfer. With this in mind, the Dexter cut-off and the rate constant are varied in accordance with one another, in order to achieve the correct PLQY and emission ratios, for each of the acceptor concentrations. A Dexter rate constant, k_{Dexter}^{0}, was found to be $2x10^{7}$ s^{-1}, in combination with a (centre-of-mass) Dexter cut-off of around 2 nm, compared to a maximum of around 5 nm for FRET.

3.6.3 Non-radiative decay from the acceptor triplet

After a Dexter event has occurred, the first triplet state of the acceptor molecule is populated. The decay from this state is non-radiative, resulting in a loss in efficiency of the UPSF system. Upon this quenching mechanism, the acceptor becomes blocked due to the single occupancy constraint. The role of the non-radiative decay is to clear the occupied state of an acceptor molecule. Coupled with the aforementioned rate constants, the rate at which non-radiative decay is collected, was also varied. If the sites are blocked for a long period of time, phosphorescence is the predominant emission, if the sites are cleared too quickly, fluorescence emission is overestimated. The non-radiative emission was varied and optimised accordingly, resulting in a decay time of 0.02 μs, longer than that of fluorescence at 4 ns, but shorter than the 1.60 μs of phosphorescence.

3.6.4 Model validation

The increase in acceptor concentration causes an increase in the amount of FRET events (consequently fluorescence), but also Dexter events. Ultimately, this shifts the emission from largely (slower) phosphorescence, towards faster fluorescence, giving a reduced radiative decay time. As the number of Dexter events also increases, it is expected and shown from experiment that the PLQY should decrease with increasing acceptor concentration. The PLQY values and all emission data, are from the contribution of both phosphorescent and fluorescent photons. With the rate constants optimised, averaging over the three acceptor concentrations, the final values of PLQY, emission ratios and radiative decay times, in comparison to those achieved from experiment, are listed in Table 3.2, for each of the acceptor concentrations. The radiative decay times are achieved from the plots of emission, in a simulated TRPL spectrum, making use of the multiexponential fitting method, described in section 3.5.1. An example of such spectrum and fit for an acceptor concentration of 1%, is shown in Figure 3.8 (a), together with the equivalent experimental fit. Additionally, for all three acceptor concentrations, the simulated multiexponential fits are plotted with the corresponding experimental TRPL multiexponential fits, in Figure 3.8 (b).

Acceptor concentration	PLQY (experiment)	PLQY (simulations)	τ_{rad} (experiment)	τ_{rad} (simulations)
0.5%	82%	76%	1.06 µs	1.35 µs
1.0%	66%	67%	0.77 µs	0.83 µs
1.5%	63%	62%	0.49 µs	0.41 µs

Table 3.2 PLQY and radiative decay times from experiment and simulations, listed with increasing acceptor concentration

The correlation between the experimental and simulated TRPL multiexponential fits is clear, also coupled with the agreement of PLQY values and calculated radiative decay times, listed in Table 3.2**,** signifying an accurate theoretical representation of the UPSF system. The trends observed from both simulations and experiment, show that with increasing acceptor concentration, the radiative decay time is lowered due to a shift from slower to faster emission, or the increase in the number of fluorescent photons, from more FRET events. Additionally, the PLQY values decrease with more acceptor molecules, reinforcing the expectation of more Dexter events.

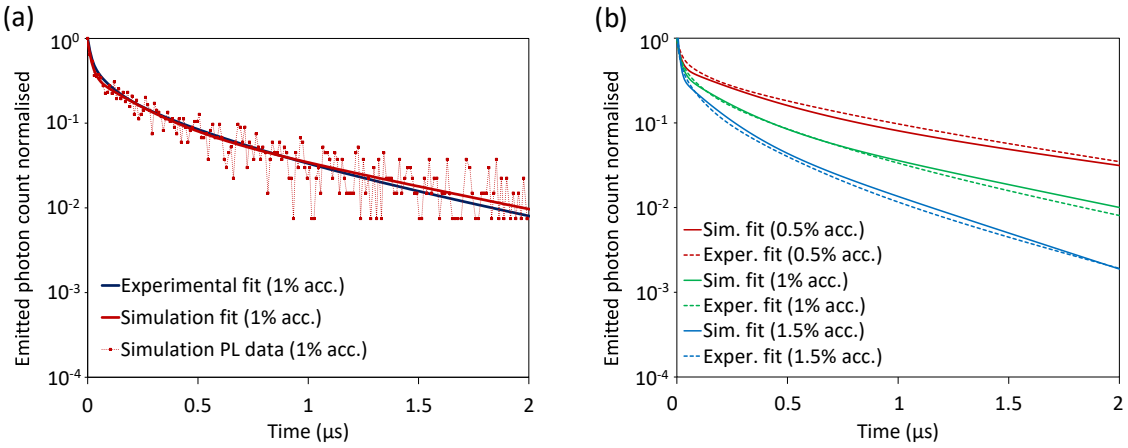

Figure 3.8 (a) Simulated photoluminescence (PL) plot for the 1% acceptor system, emitted photon counts normalised, plotted over a time of 2 µs, emission data (red dots and dashed line) and multiexponential fit (solid red line), with the equivalent experimental TRPL fit (blue). (b) Simulated photoluminescence (PL) multi-exponential fits (solid lines) and equivalent experimental TRPL fits (dashed lines), for 0.5% (red), 1.0% (green) and 1.5% (blue) acceptor concentrations.[196]

3.7 Beyond Experiment

3.7.1 Higher acceptor concentrations

With the simulation results closely matching that of experiment, it is possible to study the system in more depth and expand on the experimental results. To do this, three additional concentrations were chosen, with 2.0, 2.5, and 3.0 volume % acceptors. In the same manner as the previous concentrations, the PLQY values and radiative decay times were evaluated. The PLQY values were found to remain almost constant at around 62 %, with values of 62.5 % (2 % acc.), 62.6 % (2.5 % acc.) and 61.8 % (3 % acc.). All simulated and experimental PLQY values are shown in Figure 3.9 (a).

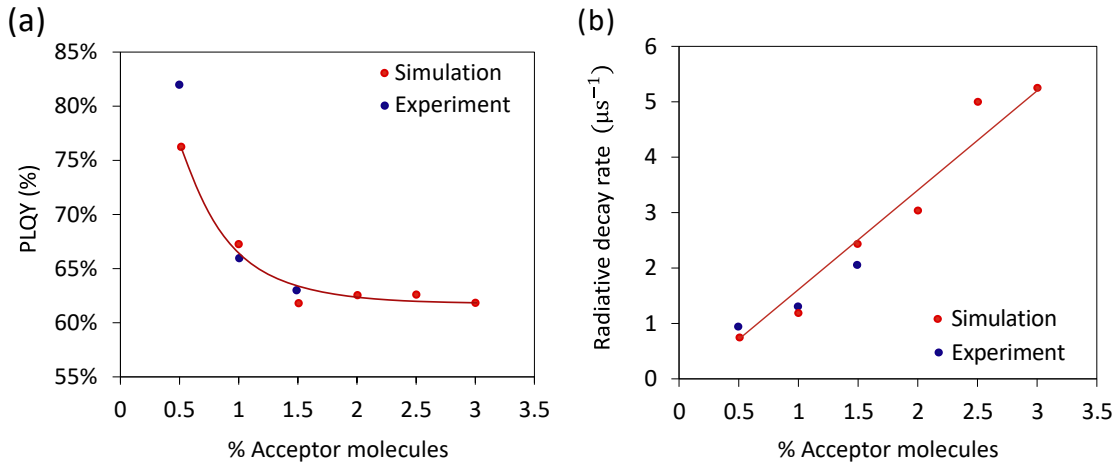

Figure 3.9 Comparison of simulated (red) and experimental (blue) (a) PLQY values and (b) radiative decay rates, for all acceptor concentrations. The red lines serve only as a visual aid.[196]

This indicates that the system reached a degree of saturation, in terms of the number of Dexter events, as a consequence of the slow, non-radiative, acceptor triplet decay. The radiative decay times also appeared to show a lower limit approaching, with 0.33 µs, 0.20 µs and 0.19 µs, for the 2 %, 2.5 % and 3 % concentrations respectively. Indicating a saturation of FRET events and resulting fluorescence, where the addition of further acceptors has little impact on the radiative decay. The radiative decay rate, (the inverse of the radiative decay time), is plotted for each of the concentrations, with comparison to experiment in Figure 3.9 (b). As a result of

the radiative decay time limit, the OLED lifetime will also ultimately reach a limit, due to a direct correlation between radiative decay rates and the lifetime of the OLED, demonstrated experimentally.[215] Additionally, the long-lived acceptor triplet state can contribute to degradation of the UPSF OLED, leading to a further limitation of the device lifetime.

3.7.2 Relative contributions of phosphorescence and fluorescence

A further possibility of understanding the UPSF system more clearly, is with the breakdown of the emission into the constituent phosphorescent or fluorescent photons. The experimental quantity of transfer efficiency, is defined as the proportion of excitons decaying radiatively due to FRET, between the donor and acceptor molecules, i.e. the efficiency of the FRET process.[215] This quantity can be directly plotted with the donor and acceptor emission values, achieved with simulations, for each of the concentrations.

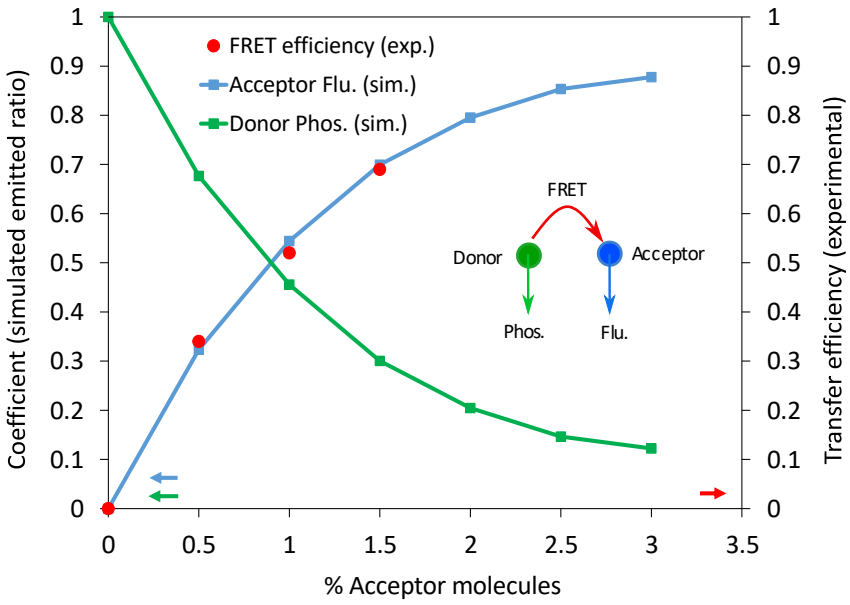

Figure 3.10 Left axis: Simulated emission coefficients, referring to the fraction of emission type, over total emission. Phosphorescence from the donor (green) and fluorescence from the acceptor (blue). Right axis: transfer efficiency calculated from experimentally achieved results, FRET efficiency (red).[196]

It is evident from Figure 3.10 that there is a direct link between the amount of fluorescence predicted from simulations and efficiency of FRET found from experiment. Thus, it can be determined that the fluorescence observed is a direct consequence of FRET from the donor to the acceptor. This is an obvious conclusion from the simulated acceptor emission, as there are no direct (initial) acceptor excitations possible, therefore any fluorescence collected can only be due to FRET. The correlation of experimental FRET efficiency and the fluorescence emission of simulation, signify a further validation of the code, reinforcing the accuracy of the representation of the UPSF system. In addition to this, the trend for higher acceptor concentrations is also shown. As the number of acceptors continues to increase, further than the 1.5 % concentration, the fluorescence emission also continues to increase. That being said, it is clear that this increase begins to level out after 2.5 % acceptor concentration, which is not obvious from experimental results, as a simple linear relationship was shown from the FRET efficiency values. The levelling of the fluorescence emission emphasises the idea of a saturation of acceptor molecules, as found from the lower limits of both PLQY and radiative decay values. This would signify that simply adding acceptor molecules to the UPSF system cannot reduce the radiative decay time to that of fluorescence alone. Since there exists a limit to the amount of fluorescence that is achievable, there is also a limit to the lifetime of the device.

3.7.3 An ideal UPSF OLED

The undesired, donor to acceptor Dexter events cost the UPSF system a loss of efficiency. However, the extent to which this Dexter transfer inhibits FRET, is unknown. Therefore, in the ideal case, which would be the complete suppression of donor-acceptor Dexter energy transfer, any change to the FRET events can be examined.

The extent to which Dexter energy transfer impacts FRET is shown in Figure 3.11, the percentage of FRET events is calculated with respect to phosphorescence or phosphorescence and Dexter, in the case of no Dexter or with the inclusion of Dexter, respectively. In the normal UPSF system, where Dexter energy transfer would be present, the percentage of FRET events reaches a maximum of 54 %, for the 3 % acceptor concentration. On the other hand, in the ideal scenario, where no Dexter transfer occurs between donor and acceptor, this increases to 89 %, an increase of 35 %. This shows that limiting Dexter energy transfer would have a large impact on the amount of FRET and therefore fluorescence. The result of this would be that the UPSF OLED would have a significantly increased operational lifetime, as almost 90 % of the events

would result in fluorescence, moving away from the degradation of the long-lived phosphorescence state.

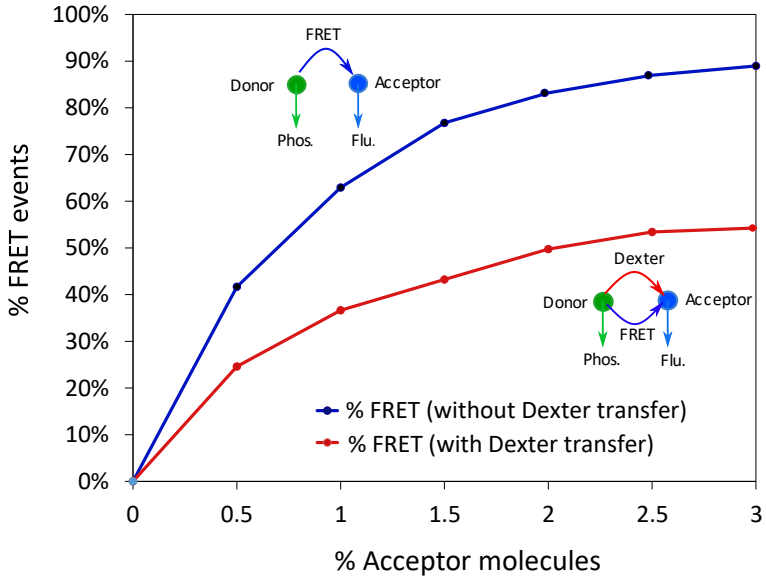

Figure 3.11 Simulation results of the percentage of FRET events, with respect to all events from the donor molecules, with (blue) and without (red) Dexter energy transfer, as a function of acceptor concentration.[196]

Evidently, the suppression of donor-acceptor Dexter transfer can lead to a potentially substantial decrease in the radiative decay time. This is shown in Figure 3.12 for the 3 % acceptor concentration, by reducing the Dexter transfer, from 100 % in the original system, to 0 % in the ideal case. A reduction by a factor of 0.4, leading to a radiative decay time of 0.08 µs, highlights the significant impact of Dexter transfer. A second modification to the system, to achieve an ideal UPSF OLED, would be with an increase of the FRET radius, R_{FRET}. Also, independently demonstrated in Figure 3.12 for the 3 % acceptor concentration. By increasing the FRET radius from 2.4 nm to 5 nm, a reduction by a factor of 0.1 was found, resulting in a radiative decay time of 0.02 µs, exceeding the effect of Dexter elimination. Therefore, when used in combination, the complete suppression of Dexter transfer and the increase of the FRET radius to 5 nm, would significantly improve the UPSF system, with simulations predicting a radiative decay time of 0.02 µs and a PLQY of 100 %.

However, it should be noted that tuning the FRET radius is particularly challenging in the UPSF system. Broadening of the donor emission will most likely result in higher-energy

photons already in the initial phosphorescent OLED, leading to faster degradation. Broadening of the acceptor absorption will also broaden its emission, leading to a shift of the OLED colour coordinate towards green. Another alternative is to align transition dipole moments of the donor and acceptor and increase the FRET rate by increasing the dipole-dipole interaction term. However, the dipole-dipole interaction depends not only on the relative molecular orientations, but also on the orientation of the vector connecting the molecules, which still varies in space. A simple estimate for a cubic lattice shows that the orientation-dependent prefactor increases from 2/3 = 0.67 for molecules oriented isotropically, to only ca 0.7 if donor and acceptor transition dipoles would be oriented perfectly in the plane of the substrate (while their connection vector remains isotropic), to 0.8 if donor and acceptor transition dipoles are perfectly aligned perpendicular to the substrate (while their connection vector remains isotropic). Only if donor-acceptor pairs are chemically bound so that their transition dipole moments are parallel to each other and to the vector connecting them, one can achieve a sizable prefactor of four. Hence, the chemical design of a dual donor-acceptor system is a clear scientific challenge.

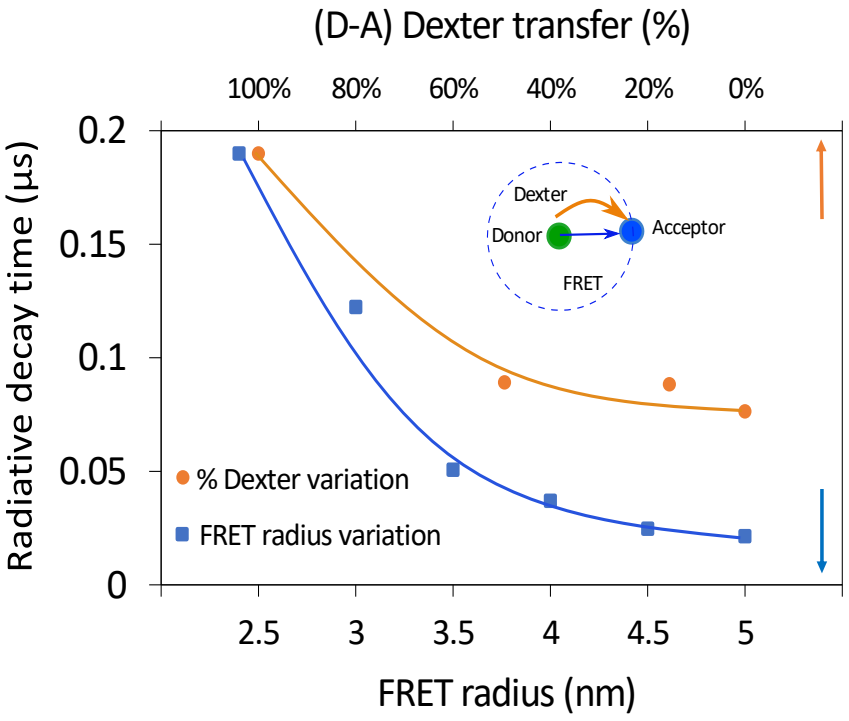

Figure 3.12 Radiative decay time (µs) reduction, towards an ideal UPSF OLED. Top axis: The effects of supressing Dexter transfer (orange) or bottom axis: increasing the FRET radius (blue). The blue and orange lines serve only as a visual aid.[196]

3.8 Conclusion

The potential of a UPSF system, which facilitates both singlet and triplet emission, keeping in mind its application in a blue OLED has been estimated. The individual energy transfer processes have been examined and their rate constants optimised to match experimental findings, allowing for a multiscale simulation model of a blue UPSF OLED. By expanding the scope of experiment, it was shown that the current set of materials is limited to radiative decay times of around 0.20 µs, which can be achieved by increasing the acceptor concentration (ca 3 % vol). At these concentrations, the undesired Dexter energy transfer, which results in a loss of efficiency, also saturates, resulting in PLQY values around 60%. Both PLQY and radiative decay time cannot be improved by addition of further acceptors. In fact, further acceptor addition would be detrimental to this goal, as the continued population of the long-lived acceptor triplet, contributes to degradation of the OLED.

An ideal UPSF system was also examined, where there would be no Dexter energy transfer, the extent to which it limits the number of FRET events in the system was apparent. By stopping donor-acceptor Dexter transfer it is possible for the UPSF system to increase FRET (and hence fluorescence) by 35 %. Additionally, if the FRET radius can be doubled, in combination with Dexter suppression, the UPSF system can achieve radiative decay times of around 0.02 µs, which is a remarkable decrease, illustrating the possibilities of the UPSF concept. The chemical design of such donor-acceptor combinations is, however, a challenge, as it easily leads to a trade-off between the FRET efficiency and the OLED colour coordinate.

4 OLED material library*

One of the major advantages of using organic molecules is the possibility of manipulating chemical composition to target specific properties, such as emission colour and charge carrier transport abilities. By employing appropriate material design, the aim is to achieve an optimal balance between stability, efficiency, operational driving voltage, and the colour coordinate of the OLED device. However, molecular design often relies on chemical intuition and with a vast number of potential candidates for each of the layers, this approach is inherently flawed. Therefore, in order to optimise design, a systematic approach which links chemical structure to macroscopic properties would be greatly beneficial.[118,119] Ideally, this would focus solely on *in-silico* pre-screening, prior to synthesis. Predictive computational modelling is, however, not yet sufficiently accurate for this task exclusively[120] and with experimental pre-screening being an extensive and costly procedure, a collective experimental and *in-silico* approach presents a favourable alternative.

The morphology of the system is crucial in this task, as morphological disorder can lead to energetic disorder and energy traps, affecting charge transport. As a result, predictive structure–property simulations are difficult, as realistic morphologies require accurate modelling capable of predicting local packing arrangements, molecular ordering, and trap concentration.[121] In order to construct morphologies representative of experimental systems, simulations require well controlled generation of homogenous amorphous solids. This can be achieved by thermal annealing above the glass transition temperature of the material, followed by a fast cooling process to form a glass structure, in an attempt to imitate the typical deposition process of an OLED layer structure. By doing so, the molecules are locked in local energy minima. Unfortunately, this often varies significantly between experiment and simulation, such that the

*Text adapted from:
[1]. Computer aided design of stable and efficient OLEDs; Paterson, L.; May, F.; Andrienko, D.; J. Appl. Phys. **2020**, 128 (16), 160901. doi: 10.1063/5.0022870[1]
[2] Physical properties of OLED host materials; Mondal, A.; Paterson, L.; Cho, J.; Lin, K.-H.; Bas van der Zee, Wetzelaer, G. A. H.; Stankevych, A.; Vakhnin, A.; Kim, J.-J.; Kadashchuk, A.; Blom, P. W. M.; May, F.; Andrienko, D.; Submitted to Chemical Physics Reviews (2021)

resulting morphologies regularly disagree. The main challenge is that realistic molecular packing is difficult to achieve and requires long simulation times to study self-assembly. By employing more complex methodology with increased computational cost, ultra-stable glass structures can be achieved by depositing particles one-by-one to obtain uniform packing, more closely mimicking that of experimental physical vapor deposition structures.[231]

Accurate morphologies rely on efficient classical force fields, while accurate descriptions of morphological and electronic degrees of freedom require polarisable force fields. The parametrisation of these force fields is a tedious task and impossible for the vast number of organic compounds required for pre-screening.[232–234] To overcome this, it is possible to use the similarities among the molecules most likely to be experimentally investigated, in order to create molecular fragments or building blocks, including the force field parameters. The concept of an extendable molecular library, containing the building blocks required to generate realistic morphologies, would then permit the swift characterisation of new systems/materials.

For this concept to be brought to a realisation, a well-defined simulation workflow must firstly be approved, as the *in-silico* evaluation of organic materials involves accurate prediction of device characteristics from the corresponding molecular building blocks, requiring simulations over a broad range of length and time scales. To establish a starting point, simulation results for twelve small organic molecules are summarised, the molecular structures of which are shown in Figure 4.1. The simulation results are tested for accuracy by comparing energetic disorder, ionisation energy in the solid-state, and charge carrier mobilities, to experimentally measured values. By doing so, the outlined simulation workflow and the force fields used can be validated, allowing for the expansion of the library and further structures to be investigated.

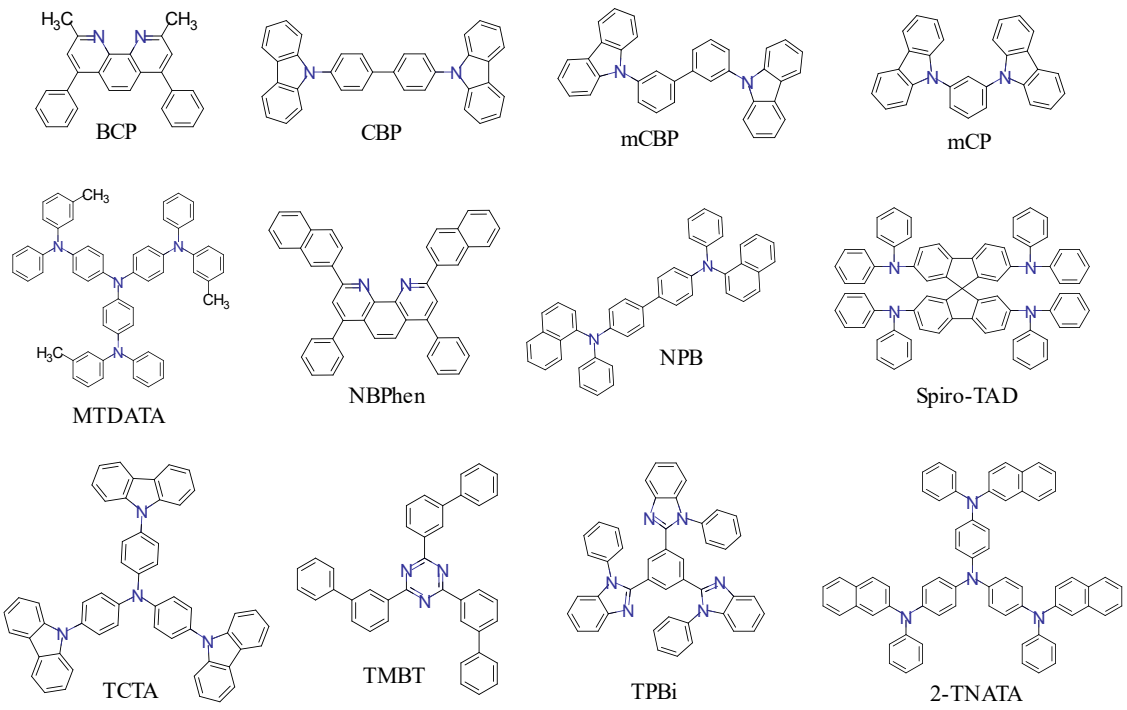

Figure 4.1 Chemical structures of the twelve small organic molecules investigated for the OLED material library; BCP, CBP, mCBP, mCP, MTDATA, NBPhen, NPB, TCTA, TMBT, TPBi, Spiro-TAD, and 2-TNATA.

4.1 Simulation workflow

Firstly, in order to generate realistic morphologies, appropriate force fields including accurate descriptions of bonded and non-bonded interactions, must be used. Additionally, polarisable force fields are required, which take into account the charge distribution rearrangement caused by changes in the environmental charge distribution. An amorphous morphology can then be simulated with molecular dynamics (MD), typically annealing above the glass transition temperature, followed by fast quenching to room temperature using the NPT ensemble. Density functional theory (DFT) based electronic structure methods, can be utilised to compute gas-phase ionisation energy (IE_0) and electron affinity (EA_0). The choice of functional has to be carefully considered, with the importance of considering long-range corrected hybrid functionals for IE_0 and EA_0 values, recently shown.[235] In disordered organic materials, such as those found in OLEDs, charge carriers are localised and propagate through the system by

successive hops from one molecule to another. Rates can be computed with the Miller-Abraham expression,[177] typically utilised within gaussian disorder models (GDM), with a lattice arrangement of hopping sites and gaussian distributed site energies. Alternatively, rates can be described by a thermally activated type of transport, in terms of Marcus theory.[168–170] Or by using Weiss-Dorsey rates[172–176] for a wider range of temperature regimes, specifically using the low temperature approximations where Marcus rates are not applicable.

Within the high temperature limit of classical charge-transfer theory,[168,171] the Marcus rate equation is derived from the importance of environmental coupling, using linear response theory to describe a heat bath coupled to electronic tunneling.[172] This quantum mechanical tunnelling moves the electron from one molecule to the other, at sufficiently high temperatures, when the nuclear vibrations (also described as bath fluctuations) bring the corresponding energy levels into resonance. The rate for a charge to hop from site i to site j (ω_{ij}) is given by:

$$\omega_{ij} = \frac{2\pi}{\hbar} \frac{J_{ij}^2}{\sqrt{4\pi\lambda_{ij} k_B T}} \exp\left[-\frac{(\Delta E_{ij} - \lambda_{ij})^2}{4\lambda_{ij} k_B T}\right] \tag{4.1}$$

Here, λ_{ij} is the reorganisation energy, the response to a change of charge state. J_{ij} is the electronic coupling matrix elements, describing the strength of coupling between two localised states, and $\Delta E_{ij} = E_i - E_j$ is the driving force, or site energy difference between two neighbouring sites, where E_i is the site energy of molecule i.[163] Molecules within a small cut-off range are considered neighbours, between which carrier hopping can occur. The quantities within the Marcus equation are then computed for each neighbouring pair. Computation of site energies includes (1) the ionisation energy and electron affinity of a single molecule, in charged and neutral geometries and (2) the interaction with the environment, including the electrostatic and induction contributions, with adequate cut-offs for long-range interactions to be considered. For reorganisation energies, considering a charging and discharging molecule, the internal contribution due to geometric rearrangement and external contribution due to the environment, must both be included. Finally, the electronic coupling elements require approximation of diabatic states, usually with the ionisation energy and electron affinity, for hole or electron transport, respectively. With the charge transfer rates computed, it is possible to then model charge dynamics. Each carrier hop or event, takes the system from state ‘a’ to ‘b’, with the corresponding rate for this transition and a probability for it to occur, which can be represented by the master equation. Kinetic Monte Carlo (KMC) is one method of solving the master

equation, effectively providing charge carrier mobilities in the given system, for holes or electrons.[118,149]

In the following sections, each step of the simulation workflow is outlined in greater detail. The results are included for the most relevant parameters of the simulations and compared to experimental values, where available.

4.1.1 Molecular Dynamics

DFT methods were used to accurately parameterise the empirical OPLS-AA force field,[232–234] for the twelve chemically diverse molecules. All Lennard-Jones parameters were taken from this force field in combination with the fudge-factor of 0.5 for 1-4 interactions. Atomic partial charges were computed using the ChelpG[156] scheme for electrostatic potential fitting as implemented in Gaussian09,[236] employing the ground state electrostatic potential determined at the B3LYP/6-311+g(d,p) level of theory. In order to generate amorphous morphologies, MD simulations were carried out using the GROMACS simulation package.[229,230,237] The amorphous state was generated by an annealing step, followed by a rapid quenching to lock the molecules in a local energy minimum. This procedure has been previously applied for the preparation of amorphous structures of OLED materials.[238,239] The starting configurations used in the MD simulations were prepared by randomly arranging 3000 molecules in a simulation box using the Packmol program.[240] These initial structures were energy-minimised using the steepest-descent method and annealed from 300 K to 800 K, followed by fast quenching to 300 K. Further equilibration for 2 ns and 1 ns production runs were performed at 300 K. All simulations were performed in the NPT ensemble using canonical velocity rescaling thermostat,[241] a Berendsen barostat for pressure coupling,[141] and the smooth particle mesh Ewald technique for long-range electrostatic interactions. A time-step of 0.005 ps was used to integrate the equations of motion. Non-bonded interactions were computed with a real-space cut off of 1.3 nm.

4.1.2 Coupling elements

The transfer integral or coupling elements, $J_{ij} = \langle \phi^i \mid \hat{H} \mid \phi^j \rangle$, represent the strength of the coupling of the two frontier orbitals $|\phi^i\rangle$ and $|\phi^j\rangle$ localised on each molecule in the charge

transfer complex. It is highly sensitive to the characteristic features of the frontier orbitals as well as the mutual orientations of the two molecules and follows an exponential decay with distance. The electronic coupling elements, were computed for each neighbouring molecular pair (ij) using a projection method.[167,242] Molecular pairs were added to the neighbour list, with a centre-of-mass distance cut-off (between rigid fragments) of 0.7 nm. These calculations were performed at the PBEPBE/6-311+g(d,p) level of theory using the Gaussian09,[236] and VOTCA[147,148] packages. The frozen core approximation was used with the highest occupied molecular orbitals providing a major contribution to the diabatic states of the dimer.

4.1.3 Reorganisation energies

The reorganisation energy of the system takes into account the charging and discharging of a molecule. When a charge moves from molecule i to molecule j, there is an intramolecular contribution (λ_{ij}^{int}), due to the internal reorganisation of the two molecules and an intermolecular, known as an outersphere contribution (λ_{ij}^{out}), due to the relaxation of the surrounding environment.[147,163] The internal reorganisation energy is calculated as $\lambda_{ij}^{int} = (U_i^{nC} - U_i^{nN}) + (U_j^{cN} - U_j^{cC})$, for molecule i and j, where the lowercase represents the neutral (n) or charged (c) molecule and the uppercase represents the neutral (N) or charged (C) geometry. The individual contributions were calculated by DFT using B3LYP/6-311+g(d,p) level of theory.

4.1.4 Electron affinity and ionisation energy

For the isolated molecules, DFT at the M062X/6-311g(d,p) level of theory* was used to compute the gas-phase ionisation energy (IE_0) and electron affinity (EA_0), with the Gaussian09 program.[236] For this, the neutral molecule in the neutral geometry (E_{nN}), as well as the charged molecule in the charged geometry (E_{cC}) were computed. The IE_0 and EA_0 values were then calculated as $E_{cC} - E_{nN}$, where E_{cC} represents, either the cationic or anionic state. The solid-state electron affinities (EA_{tot}) and ionisation energies (IE_{tot}) were calculated from the

* Various levels of theory were used and the resulting IEs compared with experimental values, the M062X functional was shown to give the best overall correlation.

corresponding density of states (DOS) (explained in section 4.1.5), as EA= α +2σ or IE= α - 2σ, where α represents the mean of the DOS and σ is the width of the distribution, for electrons or holes, respectively. The gas-phase ionisation energy (IE_0) and electron affinity (EA_0), as well as the solid-state electron affinities (EA_{tot}) and ionisation energies (IE_{tot}) are summarised in Table 4.1 (a) and (b) for each material. Experimental IE values are compared with simulation values, as listed in the table, with a correlation plot shown in Figure 4.2. For the experimental values, photoelectron yield spectroscopy in air (PESA) was performed on 50 nm thick thermally evaporated films at Merck KGaA, Darmstadt, Germany. The IE values from ultraviolet photoelectron spectroscopy (UPS) are taken from the literature, with references included in Table 4.1 (b).

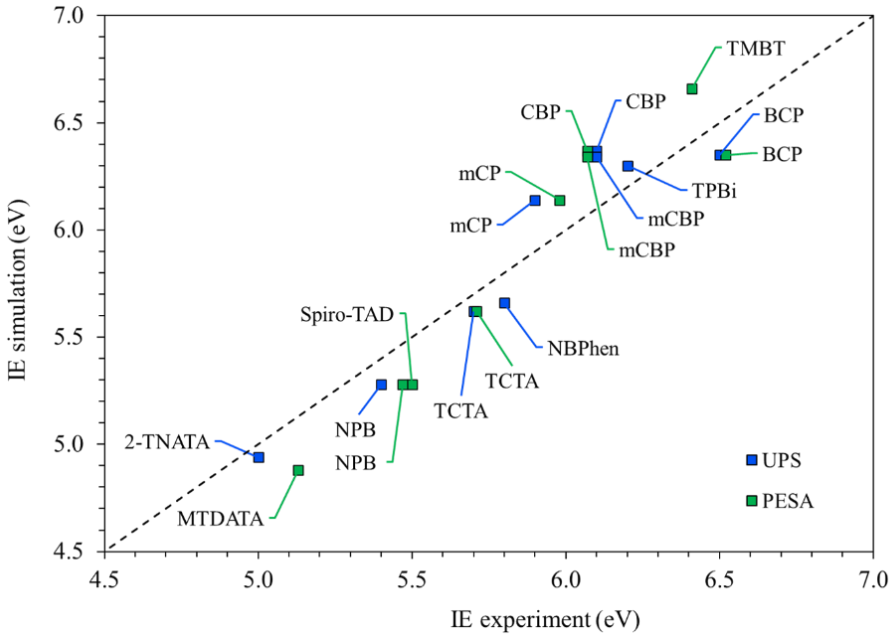

Figure 4.2 Simulated solid-state ionisation energies (IE_{tot}) compared to experimental values obtained by UPS: $R^2 = 0.899$ (blue) & PESA: $R^2 = 0.911$ (green). The linear relationship (x = y) is shown by the dashed line.

The IE values obtained from the DOS of the various materials are in good agreement with the experimental IE values, depicted in Figure 4.2 as the total correlation and in Figure 4.3 (b) for the individual materials. The computed IE_{tot} values are a combination of the gas-phase IE_0, as well as the electrostatic and induction contributions. This is necessary as the gas-phase IE is

for a single isolated molecule and does not account for the solid-state effects required to accurately determine electronic properties. The good agreement of the computed (IE_{tot}) and experimental IE values, signifies a high degree of accuracy of the polarizable force fields and the computational method used.

The situation is somewhat different for electron affinities, where using different computational techniques can lead to large variation of the gas-phase electron affinity values. Moreover, there is no clear benchmark possible for the solid-state, because of the sparse availability of the inverse photoemission spectroscopy measurements. So, a clear method of validating the simulation EA_{tot} values remains to be established.

(a)

System	$\sigma^{sim}_{electron}$	EA_{sim}			
		EA_0	EA_{elec}	EA_{ind}	EA_{tot}
BCP	0.144	0.39	-0.30	0.65	1.03
CBP	0.118	0.45	0.003	0.68	1.37
mCBP	0.151	0.41	-0.19	0.69	1.21
mCP	0.145	-0.27	-0.22	0.80	0.61
MTDATA	0.109	-0.11	-0.12	0.95	0.93
NBPhen	0.168	1.04	-0.41	0.62	1.58
NPB	0.098	0.12	-0.21	0.73	0.83
Spiro-TAD	0.102	0.29	-0.13	0.69	1.05
TCTA	0.189	0.08	0.01	1.43	1.90
TMBT	0.159	0.98	-0.36	0.70	1.64
TPBi	0.125	0.59	-0.18	0.69	1.35
2-TNATA	0.187	0.16	-0.10	1.04	1.47

(b)

System	σ^{sim}_{hole}	σ^{exp}_{hole}		IE_{sim}				IE_{exp}	
				IE_0	IE_{elec}	IE_{ind}	IE_{tot}		
BCP	0.138			7.57	0.28	0.66	6.35	6.52/6.5	PESA/UPS[243–245]
CBP	0.096	0.125/0.10	TSL/SCLC[238]	7.10	-0.05	0.59	6.37	6.07/6.1	PESA/UPS[246–248]
mCBP	0.122	0.131	TSL	7.32	0.09	0.65	6.34	6.07/6.1	PESA/UPS[246]
mCP	0.127	0.140	TSL	7.38	0.21	0.77	6.14	5.98/5.9	PESA/UPS[245]
MTDATA	0.079			5.70	0.12	0.54	4.88	5.13	PESA
NBPhen	0.163	0.167	TSL	7.23	0.41	0.83	5.66	5.8	UPS[249]
NPB	0.087	0.088/0.09	TSL/SCLC[238]	6.25	0.20	0.60	5.28	5.47/5.4	PESA/UPS[243,247]
Spiro-TAD	0.090	0.110/0.09	TSL/SCLC[238]	6.23	0.15	0.62	5.28	5.50	PESA
TCTA	0.122	0.110/0.10	TSL/SCLC[238]	6.63	-0.02	0.79	5.62	5.71/5.7	PESA/UPS[246,250]
TMBT	0.141			8.06	0.35	0.77	6.66	6.41	PESA
TPBi	0.134	0.150	TSL	7.40	0.17	0.66	6.30	6.2	UPS[248]
2-TNATA	0.097	0.10	SCLC[238]	5.72	0.09	0.50	4.94	5.0	UPS[247]

Table 4.1 Energetic disorder (σ, eV) for (a) electron transport & electronic affinities (EA, eV) and (b) hole transport with experimental values (eV) & Ionisation energies (IE, eV) in the studied amorphous materials, with experimental values (eV) and references, where available. SCLC: space charge limited current, TSL: thermally stimulated luminescence, UPS: Ultraviolet photoelectron spectroscopy, PESA: photoemission spectroscopy in air.

4.1.5 Density of states

The MD simulation trajectories were used to evaluate the site energies of holes and electrons by employing a perturbative scheme. In this approach, the electrostatic and induction energies are added to the gas phase energies (IE_0 or EA_0), to obtain the total site energy. The electrostatic contribution is calculated with the use of Coulomb sums based on distributed multipoles (obtained from the GDMA program[155]) for neutral and charged molecules in their respective ground states. The polarisation contribution is computed using a polarisable force field based on the Thole model[160,161] with isotropic atomic polarizabilities (α_{ai}) on atoms a in molecules i. Aperiodic embedding of a charge method[251] as implemented in the VOTCA[147,148] package, was used for these calculations.

Even though the variations of the reorganisation energies and electronic coupling elements lead to variations in the simulated mobility (μ) the most significant parameter is the distribution of site energies E_i within the system, characterized by the energetic disorder (σ). To a certain extent, this is anticipated, as the mobility is exceptionally sensitive to changes in the width of the disorder distribution, for example, the $\mu \propto \exp\left[-C\left(\frac{\sigma}{k_B T}\right)^2\right]$.[179,181,252]

The energetic disorder stems from the disorder on the local electronic states which, as shown in Figure 4.3, is Gaussian-distributed. The distributions of the on-site energy differences, i.e., the differences between the energies of the system when a selected molecule is in the anionic/cationic or neutral state, including the constant internal contribution due to the gas phase electron affinity/ionisation energy, are displayed in Figure 4.3(a) and (b) for electrons and holes, respectively.

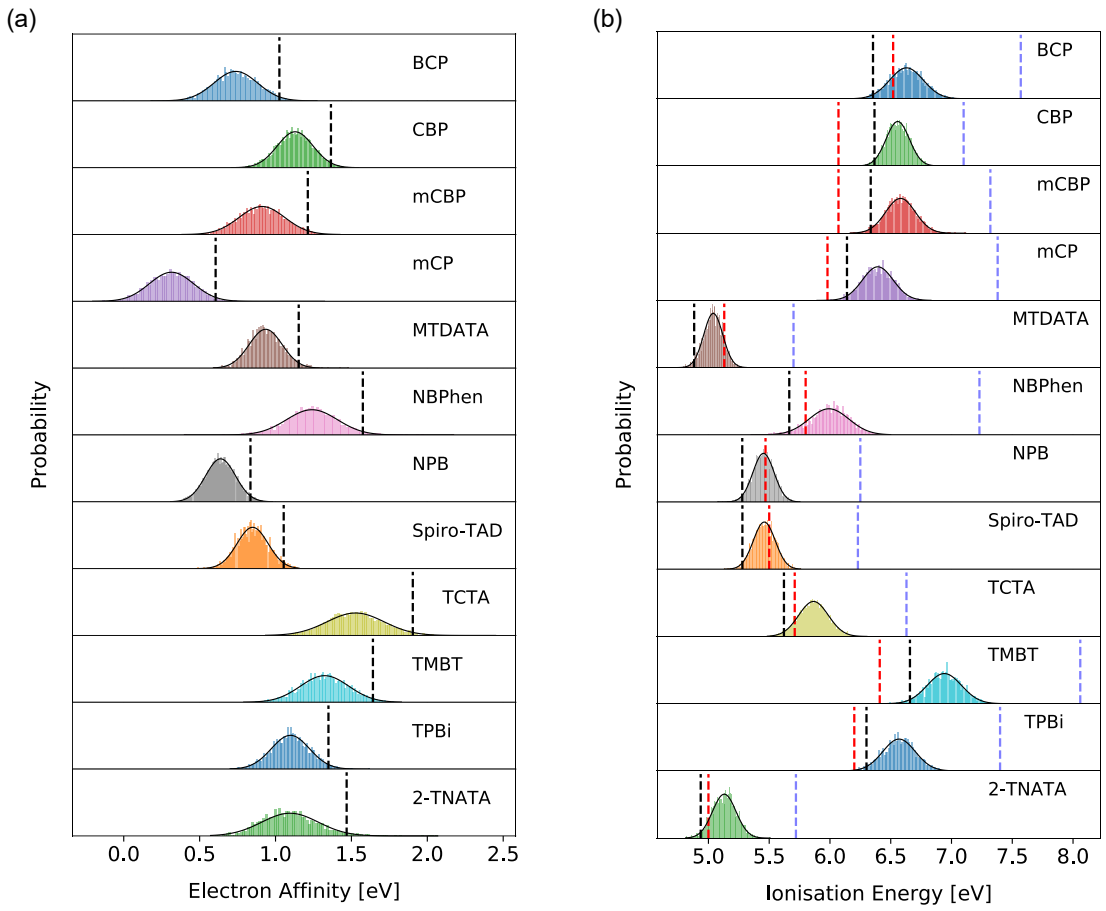

Figure 4.3 The density of states (distribution of site energies) in the amorphous materials for (a) anion, with solid-state electron affinity (EA_{tot}) shown by the black dashed lines, and (b) cation, with solid-state ionisation energy (IE_{tot}) shown by the black dashed lines. Experimental reference lines for ionisation energy (IE_{exp}) are shown as red dashed lines. Gas phase ionisation energy (IE_0) values obtained by M062X/6-311+g(d,p) level of theory are shown using blue dashed lines.

Energetic disorder

The corresponding energetic disorder (widths of site energy distributions) are summarised in Table 4.1(a) and (b). In amorphous organic materials, the energetic disorder is predominantly electrostatic. Such electrostatic interaction originates from the potential exerted on a molecule from its specific environment. Therefore, the disorder is governed by the molecular static multipoles, as well as the positional and conformational order, in a given material. On the other hand, the induction contribution stemming from the interaction of microscopic dipoles with the

localised charge carrier, reduces the energetic disorder.[147,253] The electrostatic and induction contributions for each system, for both electrons and holes, are listed in Table 4.1(a) and (b).

The energetic disorder (hole transport) values are directly compared in Figure 4.4 to experimental values from previously reported space charge limited current (SCLC) measurements[238] and/or newly carried out thermally stimulated luminescence (TSL) measurements (Kadashchuk et. al. Institute of Physics, National Academy of Sciences of Ukraine), the experimental values are also listed in Table 4.1 (b). The details of the TSL measurements have been described for the investigation of intrinsic energetic disorder, for a variety of important organic materials, elsewhere.[254–260] As electron transport in materials with a low EA (< 3.6 eV) is most likely hindered by electron trapping (oxygen-related traps),[34] the TSL technique probes the hole DOS in the materials discussed here.

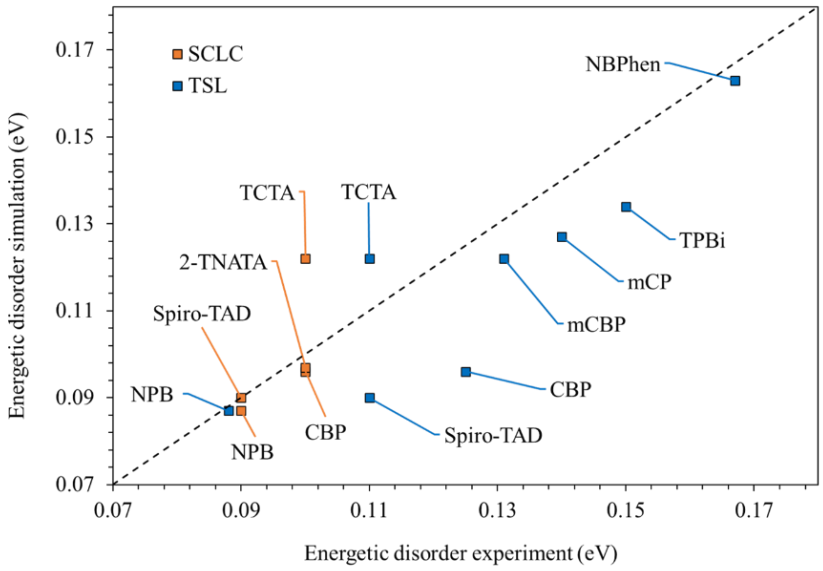

Figure 4.4 Simulated and experimental energetic disorder (eV) values for the studied materials; SCLC (orange squares), TSL (blue squares) (TSL: $R^2 = 0.77$). The linear relationship (x = y) is shown by the black dashed line, highlighting the correlation of experimental and simulated values.

Simulations predict a significant variation of energic disorder among the twelve materials for hole transport, spanning from σ = 0.087 eV observed for a weakly disordered NPB, to σ = 0.163 eV obtained for highly disordered NBPhen. The experimental results are in agreement and demonstrate a similar overall trend (Figure 4.4) with the simulation values. However, as TSL measures the ‘effective DOS’ and even a small concentration of shallow extrinsic traps can

give rise to a notable DOS broadening,[261] energetic disorder may vary slightly between experiment and simulation. Also shown in Figure 4.4, are the differences between the experimental techniques of SCLC and TSL, which may be partially due to different film morphologies related to different deposition methods (vacuum deposition or spin-coated from a solution). Nevertheless, the overall trend in energetic disorder values, in comparison to both experimental methods, is reproduced well by simulations. This is a vital observation, as the prediction of the disorder parameter is crucial for the overall accuracy of the charge transport simulations and the resulting carrier mobility.

Molecular dipoles

The observed energetic disorder can be potentially related to molecular dipoles, since lattice models with randomly oriented dipoles of equal magnitude d and lattice spacing a yield disorder $\sigma \sim d/a$. However, in a realistic morphology, both distances and dipoles can vary from molecule to molecule, which then increases the disorder. Broad distributions of dipole moments are attributed to the presence of one or more soft dihedrals in the organic materials. At finite temperature, rotation around such soft degrees of freedom leads to multiple conformers. The distribution of molecular dipoles, for the twelve materials, are shown in Figure 4.5.

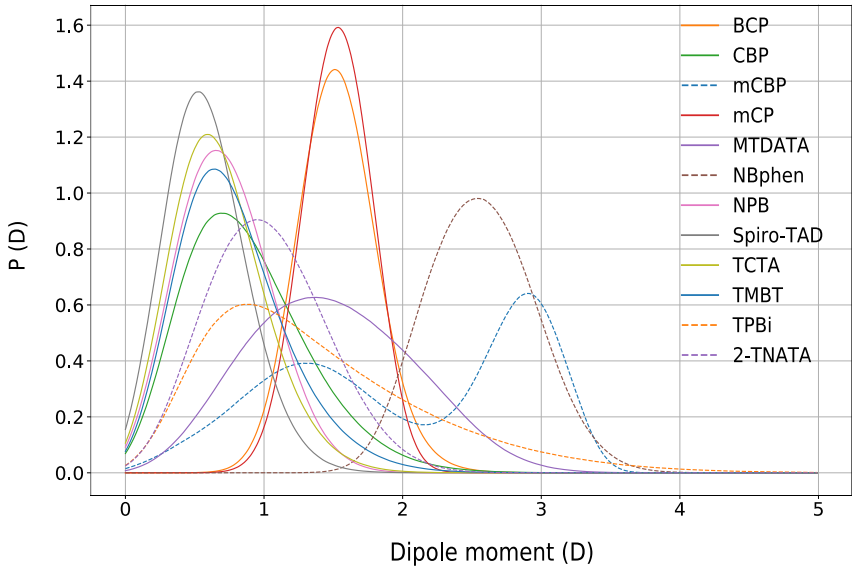

Figure 4.5 Distribution of molecular dipoles in the amorphous morphology for the twelve organic materials, calculated from MD simulations at 300K, with the partial charges obtained by GDMA.

In general, materials with a narrow distribution of molecular dipoles in their amorphous morphologies, possess small fluctuations of electrostatic multipoles in the amorphous matrix which results in smaller energetic disorder, for example NPB and Spiro-TAD. But this is not a universal conclusion and the exact role molecular dipoles play on disorder is not clear, for example the weakly disorder MTDATA possessing a large distribution of molecular dipoles. Therefore, as a point of interest, this will require further investigation for a better understanding, in order for the distribution of molecular dipoles to be considered as a potentially suitable parameter for pre-screening.

4.1.6 Charge carrier mobility

Charge transport rates were computed using the high temperature limit of classical charge transport theory, as given by the Marcus rate equation.[168–170] The master equation can then be solved with kinetic Monte Carlo (KMC), providing the time evolution of the system, giving a randomly generated trajectory of charge carrier movement. This was carried out for one charge carrier (hole or electron) in the presence of an applied electric field ($F = 1 \times 10^4$ V/cm), using a periodic simulation box. Mobilities were extracted as $\mu = \langle v \rangle / F$, where $\langle v \rangle$ is the average projection of the carrier velocity in the direction of the field ($F = 1 \times 10^4$ V/cm). The convergence of simulated mobilities with respect to the system size (i.e., a sufficient number of sites for the simulated transport to be nondispersive) due to energetic disorder must be ensured. For this purpose, the critical temperature (within Gaussian disorder model), T_c, at which the transition from dispersive to nondispersive regime takes place, was estimated and is shown in Figure 4.6 for holes and Figure 4.7 for electrons. Subsequently, fitting the mobilities obtained in the non-dispersive regimes to an empirical temperature dependence, allowing for extrapolation of the charge carrier mobility to the non-dispersive regime at room-temperature shown in Figure 4.6 and Figure 4.7. Details of such calculations can be found elsewhere.[2,194]All charge transport calculations were performed using the VOTCA package.[147,148]

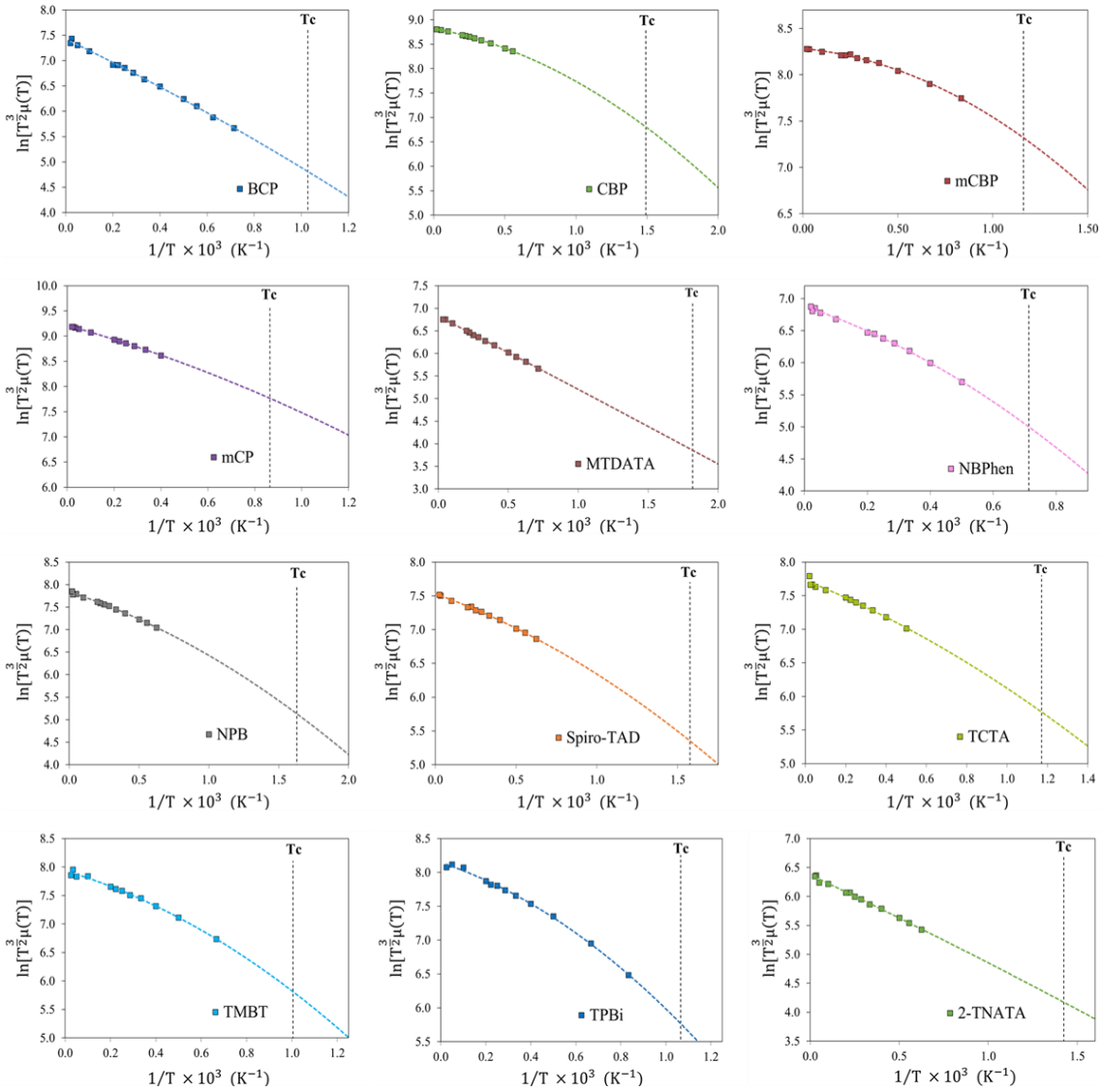

Figure 4.6 Hole mobility temperature dependence for the twelve materials, including the estimated critical temperature (within Gaussian Disorder model) Tc, at which the transition from dispersive to nondispersive regime takes place (dashed black line). Calculated for one charge carrier (hole) at a range of high temperatures, with an applied field F = $1x10^4$ V/cm. Further information regarding the temperature dependence, explanation of the fitting procedure and extraction of room temperature mobilities, can be found here.[194]

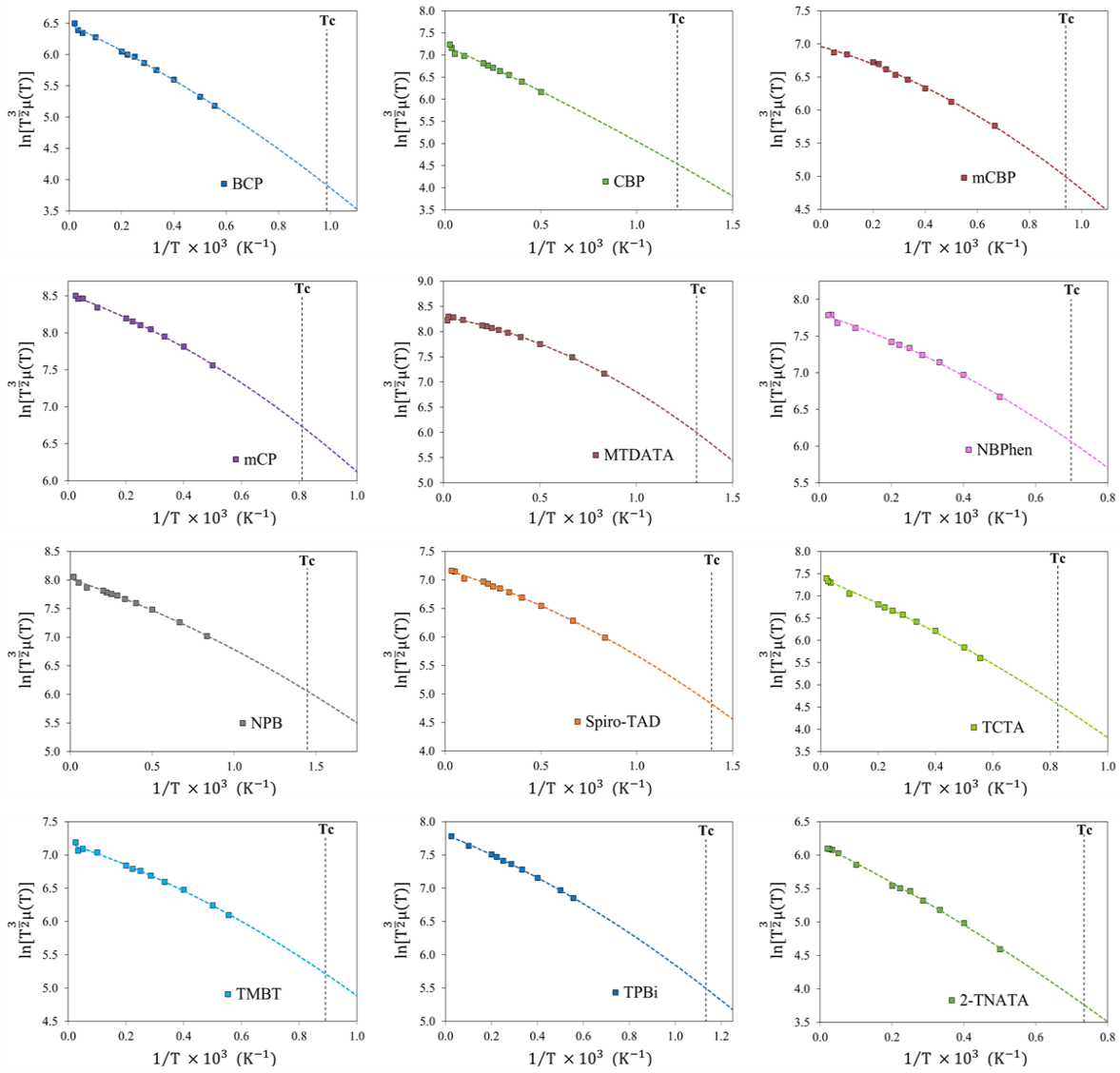

Figure 4.7 Electron mobility temperature dependence for the twelve materials, including the estimated critical temperature (within Gaussian Disorder model) Tc, at which the transition from dispersive to nondispersive regime takes place (dashed black line). Calculated for one charge carrier (electron) at a range of high temperatures, with an applied field F = $1x10^4$ V/cm. Further information regarding the temperature dependence, explanation of the fitting procedure and extraction of room temperature mobilities, can be found here.[194]

The single-carrier mobilities at room temperature for holes and electrons are summarised in Table 4.2. The experimentally measured mobility and the corresponding experimental techniques used, are also listed for comparison. Additionally, Figure 4.8 shows the correlation between the simulated and experimentally measured mobility.

System	$\mu_{hole}^{(sim)}$	$\mu_{hole}^{(exp)}$		$\mu_{elecrton}^{(sim)}$	$\mu_{electron}^{(exp)}$	
BCP	$7.94x10^{-6}$	-	-	$1.35x10^{-7}$	-	-
CBP	$4.91x10^{-4}$	$2.2x10^{-4}$	SCLC[238]	$3.64x10^{-5}$	-	-
		$5.0x10^{-4}$	TOF[262]			
mCBP	$9.00x10^{-4}$	-	-	$8.24x10^{-5}$	-	-
mCP	$2.35x10^{-4}$	$5.0x10^{-4}$	TOF[263]	$1.35x10^{-7}$	-	-
MTDATA	$1.56x10^{-5}$	$1.3x10^{-5}$	TOF[264]	$8.17x10^{-6}$	-	-
NBPhen	$1.37x10^{-8}$	-	-	$5.20x10^{-5}$	$4.2x10^{-4}$	TOF[249,265,266]
NPB	$2.04x10^{-4}$	$2.3x10^{-4}$	SCLC[238]	$4.04x10^{-4}$	(6-9) $x10^{-4}$	TOF[243]
		$2.7x10^{-4}$	TOF[264]			
Spiro-TAD	$4.99x10^{-4}$	$3.1x10^{-4}$	SCLC[238]	$3.67x10^{-5}$	-	-
		$5.0x10^{-4}$	TOF[267]			
TCTA	$1.00x10^{-4}$	$8.9x10^{-5}$	SCLC[238]	$1.61x10^{-9}$	$< 10^{-8}$	* [269]
		$2.0x10^{-4}$	TOF[268]			
TMBT	$7.47x10^{-6}$	-	-	$6.38x10^{-5}$	$1.2x10^{-4}$	TOF[270]
TPBi	$1.18x10^{-7}$	-	-	$1.18x10^{-5}$	$6.5x10^{-5}$	SCLC[271]
					(3-8) $x10^{-5}$	TOF[272]
2-TNATA	$1.72x10^{-5}$	$2.7x10^{-5}$	SCLC[238]	$4.64x10^{-6}$	(1-3) $x10^{-4}$	TOF[243]
		(2–9) $x10^{-5}$	TOF[40]			

Table 4.2 Room temperature hole and electron mobility (cm^2/Vs), achieved from simulations of the amorphous organic materials, with experimentally achieved mobilities and the corresponding techniques used, references included. TOF: time of flight experiment, SCLC: space charge limited current method.

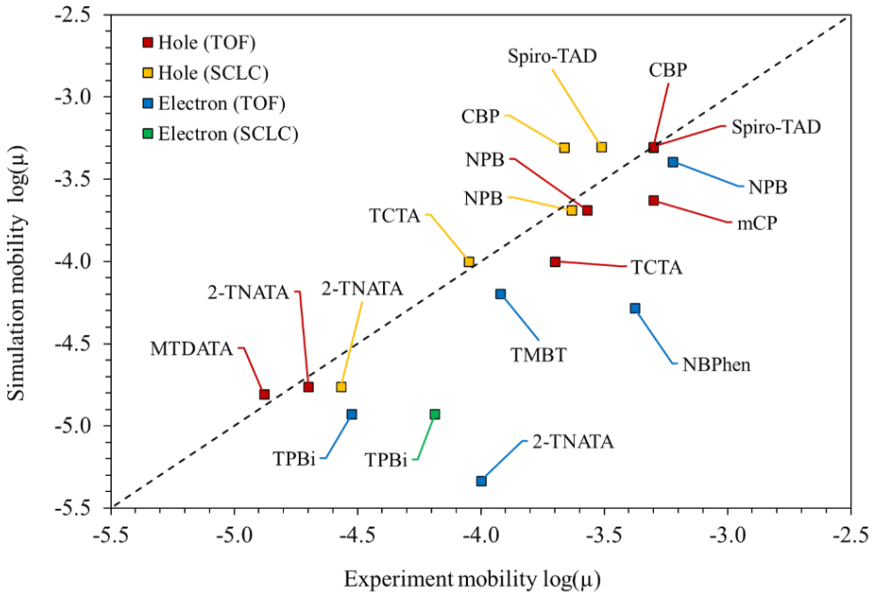

Figure 4.8 Room temperature hole and electron mobility (μ) values achieved by simulation and compared to experiment values where available. Hole-TOF (red): $R^2 = 0.95$ & Hole-SCLC (yellow): $R^2 = 0.94$, Electron-TOF (blue): $R^2 = 0.57$ and Electron-SCLC (green). The linear relationship (x=y) is shown by the black dashed line, highlighting the correlation of experimental and simulated values.

The remarkable agreement of simulation and experiment is particularly evident for hole mobilities (Figure 4.8). On the other hand, for electron mobilities, a larger deviation is observed between experiment and simulation, where simulated results indicate a systematic underestimation of experimental measurements. There are several possible explanations to account for these discrepancies. Firstly, due to the much larger energetic disorder for electrons in certain materials (Table 4.1) when compared to holes, the electron mobility will be inherently lower. Furthermore, as a result of the large disorder found in 2-TNATA and NBPhen, these materials exhibit the largest variation to experimental electron mobility, which may stem from energetic traps in the simulated morphologies. Additionally, due to different morphologies, the structural and energetic disorder can differ significantly between simulation and experiment. Despite the reasonable agreement for energetic disorder for hole transport, shown in Figure 4.4, the experimental materials used for the mobility correlation are a collection of referenced values from various studies, with potentially significant variations in disorder. The simulated morphologies for the twelve materials, do not account for the presence of carrier traps formed by structural defects or impurities such as water, which are typically unavoidable in reality. In

fact, hole or electron transport has been shown to become trap limited in materials with an IE greater than 6 eV or an EA less than 3.6 eV, respectively.[34] Therefore, direct comparison of simulation and experiment mobilities may be difficult, when considering low EA and high IE materials.

Nevertheless, the simulated mobilities indicate a remarkable agreement to experimental values, emphasising a high degree of accuracy in the computational protocol, as a whole. From this perspective, a molecular library based on these methods is not only feasible, but also has excellent prospects.

4.2 Conclusion and outlook

It is clear that a molecular library of OLED hosts would be invaluable, permitting the swift evaluation of new materials. The key question here, is how accurately and reliable a combination of various simulation techniques can predict relevant material properties, to bring pre-screening a step closer.

Firstly, considering ionisation energies from PESA measurements and UPS data taken from the literature, an excellent agreement with simulation results was observed. This encourages confidence in the polarisable force fields used for evaluation of the solid-state electrostatic contribution. Electron affinity values, on the other hand, will require further examination, but this may be challenging with sparse availability of experimental values from inverse photoemission spectroscopy measurements. Accurate solid-state energetics allows the density of states (DOS) to be predicted, and when comparing the widths of the distributions to the thermally stimulated luminescence (TSL) measurements, a similar trend was observed. The energetic disorder can be potentially correlated to the distribution of molecular dipoles, but the extent of this will require further investigation to be conclusive.

Finally, the simulated charge carrier mobility showed a remarkable agreement to experimental values, particularly for hole transport where energetic disorder is typically lower. The accurate prediction of the DOS and energetic disorder is therefore vital, as it has a significant impact on mobility.

Overall, the correlation of simulation and experimental results has been used to validate the accuracy of the force fields and the simulation methods, as an initial step towards building a

larger molecular library. The agreement of simulation and experiment, for the various parameters, particularly mobility, highlights the predictive capability of the outlined methods. The next step is to expand this library with further materials, in an effort to draw structure-property conclusions for effective pre-screening.

5 The future of computational OLED design*

Ideally, parameter-free computer-based OLED design would be employed, utilising pre-existing building blocks and tools, to begin with accurate prediction of material morphology for a new system, followed by calculation of the energetic landscape. This would lead to rate evaluation of the various processes within the system, such as charge or exciton transfer, proceeding to solving of the time-dependent master equation. All of which providing essential quantities for material evaluation, such as electron affinity, ionisation energy and hole and electron mobilities. However, this multiscale procedure, with length and time scales spanning several orders of magnitude is non-trivial and as such, it is difficult to predict device properties, from structure alone.

A necessity for future OLED development (and for all organic electronics), is the complete understanding of all fundamental processes within the device and constituent materials. Charge and energy transfer simulations play a pivotal role in this pursuit. Thereby promoting the advancement of simulation techniques and methods to achieve an increasingly comprehensive description. Exciton formation and transfer, is particularly important for OLED functionality. The theoretical tools used to determine exciton transport parameters include DFT for electronic excitation properties,[273] many-body Green's function theory and GW approximation with the Bethe-Salpeter equation (GW-BSE)[274] for excited states,[273,275,276] and an adaption of Marcus theory to describe exciton diffusion.[277] Further to this, an essential link between micro and macroscale would be employing more realistic charge transport dynamics. With an important addition, but computationally demanding approach, being the inclusion of explicit coulomb interactions and re-evaluation of charge transfer rates at each KMC step.

* Adapted and reprinted from,[1] Computer Aided Design of Stable and Efficient OLEDs; Paterson, L.; May, F.; Andrienko, D.; J. Appl. Phys. 2020, 128 (16), 160901. doi: 10.1063/5.0022870.1 with the permission of AIP Publishing

5.1 Explicit coulomb interaction

The embedding of electrostatics within KMC simulations, would provide valuable insight into charge dynamics. Specifically, within slab geometries and for interface interactions, which are vital for device characteristics. However, when investigating a system which is stochastically propagated in time, with each charge carrier hop leading to a new charge distribution and consequently altering all interaction with other charge carriers, the complexity of the problem is elevated and requires accurate and efficient methodology.

The accurate evaluation of electrostatic interactions, is crucial, but still remains a challenge, as the methods to compute electrostatics require large system sizes and inherently long-range (complex) interactions, leading to high computational cost. Interaction distance cut-off methods can be applied, to reduce the electrostatic contributions. But due to the long-range nature of electrostatics, as a result of the 1/r decay of the Coulomb potential, a cut-off radius is often insufficient and more exact methods have to be employed. In fact, neglecting long-range contributions has been shown to cause inaccuracies, with large variation of simulated carrier densities and device performance predictions, when compared to exact methods.[278] On the other hand, using exact methods for computing electrostatics typically involves summation techniques, such as Ewald summation[150] and the more efficient particle mesh Ewald (PME).[152,153] However, in large periodic systems an exact description is often unfeasible or highly computationally demanding. Therefore, further methods have to be considered, specifically for non-periodic systems (requiring more sophisticated summation).

5.1.1 Implementation within KMC

To expand on this, for the discussion of carrier hopping, with a rate according to the Marcus rate equation (explained in section 2.3.6), the driving force is the site energy difference ΔE_{ij} between the two hopping sites (i and j). This includes the total electrostatic energy before and after the hop has occurred, making the site energy the central component for electrostatic interactions. Explicit coulomb interactions, i.e., changing interactions with changing site occupations, allows for more accurate charge dynamics. A simple but elegant method to update the site energies affected by a carrier hop, can potentially permit a modest adaption to the KMC algorithm. If all electrostatic interactions can be computed prior to KMC, then it is possible to

simply read in these values and update site energies accordingly, followed by re-calculation of the rates with each carrier hop.

Computing electrostatic interactions

To achieve a realistic description, it is advantageous to consider a typical OLED layer with slab geometry and two parallel opposing interfaces. The interface and accurate electrostatic interaction, require the implementation of dielectric contrast, i.e., the central organic layer has a different dielectric constant to the upper and lower layers. In a typical system, the inclusion of 3-dimensional periodic boundary conditions (pbc), already cause the interactions to become increasingly complex. This includes, not only all interactions of charges within the central simulation box, but also all interactions of periodic charges. If dielectric contrast is then introduced at the planar interfaces, as would be the case at the interfaces with the upper and lower layers within the device, then image charges are also incorporated. For a single charge in the middle organic layer the interactions then include, (i) all periodic charges, (ii) all image charges and, (iii) all periodic image charges, as shown in Figure 5.1.*

The dielectric contrast can be described by a prefactor (Δ) for the top (t) and bottom (b) boundaries of the middle layer (m), given in terms of the dielectric constants (ε) of each layer.

$$\Delta_t = \frac{\varepsilon_m - \varepsilon_t}{\varepsilon_m + \varepsilon_t} \tag{5.1}$$

$$\Delta_b = \frac{\varepsilon_m - \varepsilon_b}{\varepsilon_m + \varepsilon_b} \tag{5.2}$$

The image charges placed along the z direction, shown in Figure 5.1, then depend on the dielectric contrast. A real single charge (q) located within the middle layer (of thickness d_z) at the position z_q, gives rise to a series of image charges along the z direction. The first image charge after the top and bottom dielectric boundaries represented by $q\Delta_t$ and $q\Delta_b$, respectively. The next set of charges are then reflected images, such that they become $q\Delta_t\Delta_b$ in the top direction and $q\Delta_b\Delta_t$ in the bottom direction.

* The total electrostatic contribution also takes into account the interactions of all charges, e.g., interaction of image and periodic charges, image and periodic image charges …

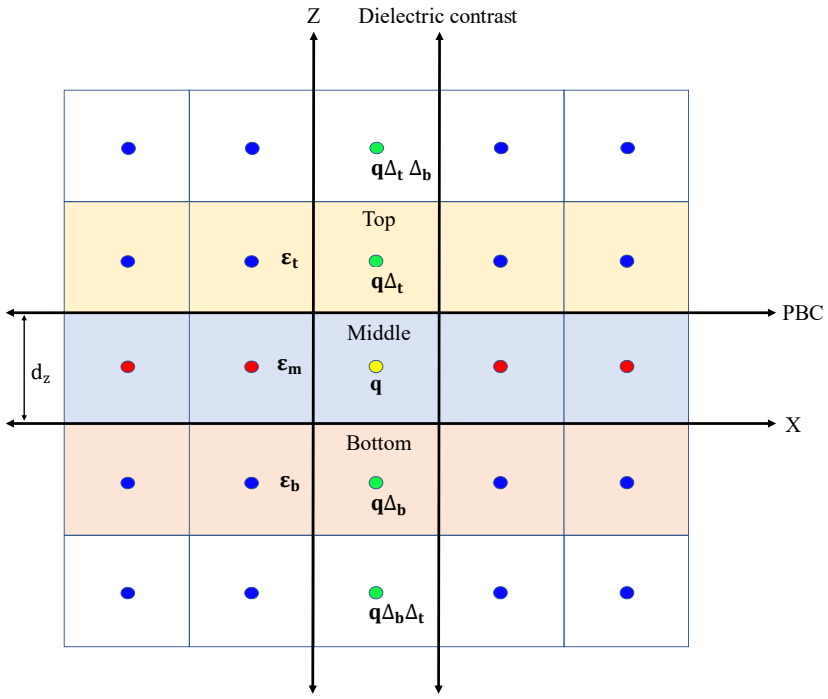

Figure 5.1 A single real charge (q) placed in a middle layer slab geometry, with pbc in X and Y (only X is shown for simplicity), and two parallel opposing interfaces (top and bottom) exhibiting dielectric contrast placed along the Z direction. For the real charge (yellow) electrostatic interaction with periodic charges (red), image charges (green) and periodic images (blue), are to be included.

An efficient method of including planar dielectric interfaces via image charge summation has been established, known as the ICMMM2D method,[279,280] an extension of the MMM2D method for electrostatic interaction in 2D slab geometry.[281] The MMM algorithm[282] is based on Fourier transform using a convergence factor $\left(e^{-\beta|r_{ij}+n|}\right)$ and a screened Coulomb interaction with screening length $1/\beta$. Within the ICMMM2D method, the periodic (due to pbc in two dimensions) and periodic image (due to the dielectric boundary in the third dimension) charge contributions to the electrostatic interactions are considered, by implementing two planar dielectric interfaces and splitting the system into interacting cells, of width λ. The simulation (real) box, with dimensions $l_x x\, l_y x\, l_z$ is split into k cells, along the z direction, such that $\lambda=l_z/k$. The pairwise interactions between two charges (i & j) are then considered in terms of a short-range contribution, which includes charges residing in neighbouring cells (the charge

separation would always be $|z|< 2\lambda$), known as the near formula* (specified here for a single dielectric constant, with $\varepsilon_b = \varepsilon_m = \varepsilon_t$):[279]

$$\begin{aligned}\phi(x_{ij}, y_{ij}, z_{ij}) \;=\; & 4u_x \sum_{l,p>0} [K_0(\omega_p \rho_l) + K_0(\omega_p \rho_{-l})]\cos(\omega_p x_{ij}) \\ & - 2u_x \sum_{n\geq 1} \frac{b_{2n}}{2n(2n)!} \mathrm{Re}[(2\pi u_y (z + iy_{ij}))^{2n}] \\ & - u_x \sum_{n\geq 1} \binom{-1/2}{n} \frac{[\psi^{(2n)}(N_\psi - u_x x_{ij}) + \psi^{(2n)}(N_\psi + u_x x_{ij})]}{(2n)!} (u_x \rho_0)^{2n} \\ & - 2u_x \log\left(4\pi \frac{u_y}{u_x}\right) + \sum_{k=1}^{N_\psi - 1} \left(\frac{1}{r_k} + \frac{1}{r_{-k}}\right) + {}' \frac{1}{r_0}\end{aligned} \tag{5.3}$$

Where, x_{ij}, y_{ij}, z_{ij} define the components of the vector connecting two charges, $u_x=1/l_x$, $u_y=1/l_y$ and $\omega_p=2\pi u_x p$. Additional $\rho_l = \sqrt{(y + l l_y)^2 + z^2}$ and $r_k = \sqrt{(x + k l_x)^2 + y^2 + z^2}$. The Bessel function of the second kind is denoted by K_0, the Bernoulli numbers by b_n, the Digamma function of order n by $\psi^{(n)}$ and a tuning constant N_ψ.[281] The prime on the last term of the near formula signifies exclusion when calculating interaction of charges with its own images.

The long-range pair-wise interactions of charges separated by more than one cell ($|z| > \lambda$), is known as the far formula:

$$\begin{aligned}\phi(x_{ij}, y_{ij}, z_{ij}) = \; & 4u_x u_y \sum_{p,q>0} \frac{\exp(-2\pi f_{pq}|z_{ij}|)}{f_{pq}} \cos(\omega_p x_{ij}) \cos(\omega_q y_{ij}) \\ & + 2u_x u_y \left(\sum_{p>0} \frac{\exp(-2\pi f_p |z_{ij}|)}{f_p} \cos(\omega_p x_{ij}) \right. \\ & \left. + \sum_{q>0} \frac{\exp(-2\pi f_q |z_{ij}|)}{f_q} \cos(\omega_q y_{ij}) \right) - 2\pi u_x u_y |z_{ij}|\end{aligned} \tag{5.4}$$

Where u_x, u_y and ω_p are defined as in the near formula, with the addition of $\omega_q=2\pi u_y q$. The additional terms are specified as, $f_{pq} = \sqrt{(u_x p)^2 + (u_y q)^2}$, $f_p = u_x p$ and $f_q = u_y q$. Due to

*For derivation of the specific electrostatic contributions and convergence factors, including the far and near formulas, refer to MMM,[282] MMM2D[281] and ICMMM2D[279]

the convergence problem of the far formula as $|z| \rightarrow 0$, the near formula is necessary. When used together, they provide the total electrostatic energy of a set of N charges, via pairwise addition (for the condition of $|z| \sim \lambda$, either the near of far formula can be used). It should be noted that particular attention should be paid to a system with a net charge. A neutralising background or neutralising walls can be utilised, in order to account for the divergent contribution, which arises in a non-neutral system.[283]

The ICMMM2D[279] method reports an asymptotic scaling of $N^{5/3}$, making it suitable when considering systems with a few hundred charges. Therefore, it is one of the possible methods for efficient and accurate evaluation of long-range electrostatics, with the potential to compute all possible pairwise electrostatic interactions, prior to the KMC simulation.

Updating the site energies

In order to utilise the pairwise electrostatic interaction from a method such as ICMMM2D, for the use in KMC, the contribution to the site energies of the given system should be clarified. Considering a system with N sites (real simulation box), by placing two charge carriers on every site combination (sites i & j, with $i \neq j$), it is possible to construct a N x N matrix of all electrostatic interactions in the system. This total electrostatic energy for occupation of these two sites, can then be used in an additive manner within the KMC simulation, when considering more than two charges. Such that, the electrostatic contribution to an occupied site simply becomes the sum of all pair-wise interactions from the N x N matrix. For example, for three charges placed on positions i, j and k, the electrostatic contribution to the site energy of i, is the total electrostatic energy of i & j, and i & k.

Therefore, an initial occupation of N sites, by **n** charge carriers, constitutes a simple update to the site energies, from the N x N matrix, followed by an update to the rates for each hop to follow. It is the proceeding steps, where the problems arise, the stochastic time evolution of the system via hopping events, changes the site occupation and thus changes the electrostatic contributions to the site energies. This requires a continuous site energy update (and rate update) for all occupied sites, at each KMC step, which can become computationally demanding ($\sim O(N^2)$ scaling for N charges), if adopting a naive approach. Therefore, the sophistication of site energy updates determines the expenditure of the method. Evaluation of site energies requires two electrostatic terms, before and after a hop. The two-step evaluation is then as follows:

1. Calculate site energy differences for all potential moves of **n** charge carriers ($\Delta E_{ij} = E_i - E_j$)
2. After a hop: update electrostatics of the occupied sites

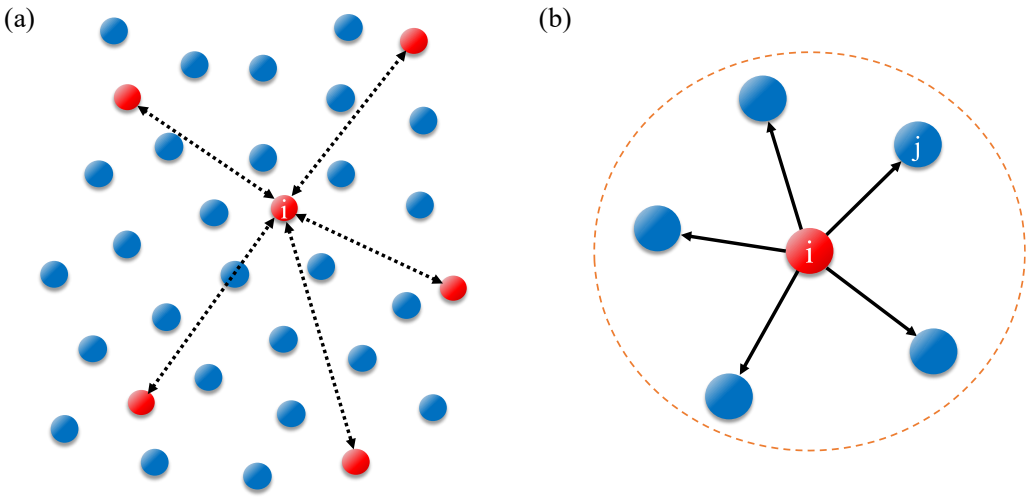

Figure 5.2 (a) Electrostatic interaction between site i and all other charges within the system (red) contributes to the total electrostatic energy of site i, (b) A charge on site i has a neighbour cut-off, $r_{cut\text{-}off}$ (orange dashed circle). The hop i→j (from i to available site j), has a rate kij, with a site energy difference ΔEij, the electrostatics before and after a hop from i to j contribute to the site energy difference and hopping rate.

The first step of the evaluation considers all n charges within the system, calculating the site energy of each occupied site with the electrostatic contribution of the other charges, as shown in Figure 5.2 (a). For the individual (occupied) sites, the site energy difference ΔE_{ij} is evaluated in terms of the total electrostatic energy before a potential hop E_i^{el} and after a potential hop E_j^{el}, illustrated in Figure 5.2 (b). If the hop i→j then occurs, the total electrostatic term is removed from site i (disabling) and added to site j (enabling). The second step of the evaluation then involves the update of all occupied sites (and their hopping sites), to include the new interaction with site j, this being a computationally demanding update and the overall limiting factor of the method thus far. Therefore, the ultimate goal is to achieve an efficient mechanism of updating the occupied sites after a hop has occurred (i.e., effective site energy and rate updates at each KMC step).

Very recently an efficient method of electrostatic inclusion in KMC was demonstrated (~O(N) scaling), exploiting the fact that each KMC step corresponds to one charge carrier hop, resulting in a modest charge redistribution.[284,285] This has been achieved with a new variant of the Fast Multipole Method,[284] and in a second approach utilising local charge contributions to the hopping rate, before and after a hop, allowing for a newly adapted cut-off scheme.[285] The implementation of electrostatics within KMC simulations is clearly challenging, but this recent progress, shows it is achievable.

5.2 Machine learning

Furthermore, computational material design tools look toward other future developments. A key area and one which has gained significant interest in recent years, is that of machine learning based techniques. Application of machine learning for OLED materials would be a significant step forward for their computational design. For this to be achievable, accurate molecular/chemical descriptors are crucial. This is a difficult task, as it requires identification of correlations between similar structures with similar properties, and linking this to a simple and systematic feature which can be extracted.[286] For OLED materials these vital descriptors are missing and only when they can be accurately obtained, can the field move towards machine learning approaches.

Nevertheless, recent progress in machine learning demonstrates the significant potential of these methods. Firstly, local properties such as electrostatic multipoles can already be predicted using kernel-based techniques.[287] Secondly, they can present practical strategies to parametrise force fields, by providing coarse-grained (CG) potentials which are more efficient.[288] Thirdly, properties such as the glass transition temperature can be correlated to the chemical structure, using a quantitative structure-property relationship approach,[289] with predictive modelling capable of pre-screening thermally stable candidates, from only topological indicies.[290] Altogether highlighting the possibilities of machine learning, in the context of OLED design.

6 Summary and outlook

OLED applications offer a unique alternative to traditional display technologies. Their flexible, lightweight and transparent possibilities, can already be found in a host of applications, from the automotive industry to mobile devices. However, due to their commercial infancy, they have obstacles to overcome, particularly regarding device lifetime and efficiency. The first hurdle is the device fabrication and processability, regarding the discussion of small molecule (SM)OLEDs vs. polymeric OLEDs (PLEDs). If SM-OLEDs are to reach their full potential, in terms of market share, simpler manufacturing must be realised. This would involve moving away from inefficient and expensive vacuum deposition processes, towards an ink-jet style printing process, something that has already been achieved for PLEDs. However, the simple device architecture of PLEDs leads to lower performance when compared to SM-OLEDs. The balance of high performance and high processability, for both SM-OLEDs and PLEDs, remains to be accomplished.

Due to their higher performance, SM-OLEDs are the subject of the present work. The vast research efforts have been highlighted throughout, including those for each of the individual OLED layers with respect to their constituent materials. Most notably, the emissive layer and the extensive efforts to achieve an efficient and stable blue OLED. Blue is particularly problematic, due to the limitations of the individual emitters, resulting in a trade-off between stability, efficiency and device colour coordinate. This stems from stable but inefficient fluorescence or efficient but unstable phosphorescence. To this aim, thermally activated delayed fluorescence (TADF) emitters have been extensively investigated, whereby a process of reverse intersystem crossing allows for more efficient fluorescent emission. However, with triplet state occupation times similar to that of phosphorescent emitters, the low stability problem remains. To address this, the novel approach of unicoloured phosphor-sensitised fluorescence (UPSF), using a dual emitting system, has been shown to achieve a balance of stability, efficiency and emissive colour. Accompanied by the multiscale computational study, presented in Chapter 3, the possibilities of the concept were quantified. Utilising the available experimental data, it was possible to parametrise the rates for all the essential processes within

the UPSF device and then expand on the experimental study, highlighting the potential of the concept with appropriate material design, and also the underlying limitations. Thereby proving that simulations can, not only be advantageous, but are an essential tool in the design of future OLEDs, addressing some of the questions left unanswered by experiment alone.

Furthermore, predictive and reliable computational modelling can help to reduce cost and enhance the process of systematic material design. Currently, the prediction of physical properties from chemical composition cannot be exclusively achieved from an *in-silico* approach, and rather, a collective experimental and computational approach is adopted. Charge transport simulations require parameters and amorphous structures which are gathered from first principles and molecular dynamics (MD) simulations, typically with experimental input. This requires rigorous parametrisation of classical force fields, for molecular degrees of freedom and the use of polarisable force fields for electronic degrees of freedom. Before then proceeding to kinetic Monte Carlo (KMC) simulations for charge dynamics and device modelling. This multiscale procedure, is of course, a non-trivial task and would be impossible for the consideration of pre-screening the vast number of potential candidates for OLED applications. Therefore, the introduction of an OLED material library, which utilises molecular building blocks to construct and characterise new compounds, can present a significant step forward. The realisation of computational pre-screening, via a molecular library, would be greatly beneficial in reducing OLED materials to a more manageable number, prior to synthesis. To establish a starting point for a material library, twelve small molecules were used to approve a simulation workflow, by comparing results to experiment for all relevant material properties, presented in Chapter 4. The correlation of simulation and experimental results, not only shows the accuracy and predictive capabilities of the computational methods used, but it also paves the way for further systems to be studied and subsequently the expansion of the library.

For the field of computer aided OLED design to progress, certain aspects of the forward problem need to be addressed before moving to parameter-free methods, allowing for extraction of device properties from molecular structure alone. To establish accurate structure-property relationships, further computational method development is essential. To this aim, one of the pressing issues to address is accurate and efficient embedding of long-range electrostatic interactions, when solving the master equation. Explicit coulomb interaction within KMC is particularly problematic, as it requires rate updates at each KMC step, making it computationally demanding. The initial steps required to make this feasible are outlined in

Chapter 5, but further method development is required. When brought to a realisation, this would allow for simulation of more realistic charge dynamics and therefore more accurate device properties. Ultimately, by addressing such aspects of the forward problem, the gap between structure and device properties can be closed, thereby reducing both experimental and computational cost.

References

(1) Paterson, L.; May, F.; Andrienko, D. Computer Aided Design of Stable and Efficient OLEDs. *Journal of Applied Physics* **2020**, *128* (16), 160901. https://doi.org/10.1063/5.0022870.

(2) Kordt, P. *Charge Dynamics in Organic Semiconductors; from Chemical Structure to Devices*; DE GRUYTER, 2016.

(3) Bernanose, A.; Comte, M.; Vouaux, P. A New Method of Emission of Light by Certain Organic Compounds. *J. Chim. Phys.* **1953**, *50*, 64–68. https://doi.org/10.1051/jcp/1953500064.

(4) Bernanose, A.; Vouaux, P. Electroluminescence of Organic Compounds. *J. Chim. Phys.* **1953**, *50*, 261–263. https://doi.org/10.1051/jcp/1953500261.

(5) Pope, M.; Kallmann, H. P.; Magnante, P. Electroluminescence in Organic Crystals. *The Journal of Chemical Physics* **1963**, *38* (8), 2042–2043. https://doi.org/10.1063/1.1733929.

(6) Tang, C. W.; VanSlyke, S. A. Organic Electroluminescent Diodes. *Appl. Phys. Lett.* **1987**, *51* (12), 913–915. https://doi.org/10.1063/1.98799.

(7) Brütting, W. *Physics of Organic Semiconductors*; WILEY_VCH Verlag GmbH & Co. KGaA, Weinheim, 2005.

(8) Spindler, J. P.; Hamer, J. W.; Kondakova, M. E. OLED Manufacturing Equipment and Methods. In *Handbook of Advanced Lighting Technology*; Karlicek, R., Sun, C.-C., Zissis, G., Ma, R., Eds.; Springer International Publishing: Cham, 2017; pp 417–441. https://doi.org/10.1007/978-3-319-00176-0_26.

(9) Shibata, M.; Sakai, Y.; Yokoyama, D. Advantages and Disadvantages of Vacuum-Deposited and Spin-Coated Amorphous Organic Semiconductor Films for Organic Light-Emitting Diodes. *J. Mater. Chem. C* **2015**, *3* (42), 11178–11191. https://doi.org/10.1039/C5TC01911G.

(10) Knox, J. E.; Halls, M. D.; Hratchian, H. P.; Bernhard Schlegel, H. Chemical Failure Modes of AlQ3-Based OLEDs: AlQ3 Hydrolysis. *Phys. Chem. Chem. Phys.* **2006**, *8* (12), 1371. https://doi.org/10.1039/b514898g.

(11) Burroughes, J. H.; Bradley, D. D. C.; Brown, A. R.; Marks, R. N.; Mackay, K.; Friend, R. H.; Burns, P. L.; Holmes, A. B. Light-Emitting Diodes Based on Conjugated Polymers. *Nature* **1990**, *347* (6293), 539–541. https://doi.org/10.1038/347539a0.

(12) Li, W.; Wang, Q.; Cui, J.; Chou, H.; Shaheen, S. E.; Jabbour, G. E.; Anderson, J.; Lee, P.; Kippelen, B.; Peyghambarian, N.; Armstrong, N. R.; Marks, T. J. Covalently Interlinked Organic LED Transport Layers via Spin-Coating/Siloxane Condensation. 5.

(13) Zhang, Y.-D.; Hreha, R. D.; Jabbour, G. E.; Kippelen, B.; Peyghambarian, N.; Marder, S. R. Photo-Crosslinkable Polymers as Hole-Transport Materials for Organic Light-Emitting Diodes. *J. Mater. Chem.* **2002**, *12* (6), 1703–1708. https://doi.org/10.1039/b110088m.

(14) Jungermann, S.; Riegel, N.; Müller, D.; Meerholz, K.; Nuyken, O. Novel Photo-Cross-Linkable Hole-Transporting Polymers: Synthesis, Characterization, and Application in

Organic Light Emitting Diodes. *Macromolecules* **2006**, *39* (26), 8911–8919. https://doi.org/10.1021/ma060844o.

(15) Duan, L.; Hou, L.; Lee, T.-W.; Qiao, J.; Zhang, D.; Dong, G.; Wang, L.; Qiu, Y. Solution Processable Small Molecules for Organic Light-Emitting Diodes. *J. Mater. Chem.* **2010**, *20* (31), 6392. https://doi.org/10.1039/b926348a.

(16) Chen, J.; Shi, C.; Fu, Q.; Zhao, F.; Hu, Y.; Feng, Y.; Ma, D. Solution-Processable Small Molecules as Efficient Universal Bipolar Host for Blue, Green and Red Phosphorescent Inverted OLEDs. *J. Mater. Chem.* **2012**, *22* (11), 5164. https://doi.org/10.1039/c2jm16463a.

(17) Tang, C. W.; VanSlyke, S. A.; Chen, C. H. Electroluminescence of Doped Organic Thin Films. *Journal of Applied Physics* **1989**, *65* (9), 3610–3616. https://doi.org/10.1063/1.343409.

(18) Kulkarni, A. P.; Tonzola, C. J.; Babel, A.; Jenekhe, S. A. Electron Transport Materials for Organic Light-Emitting Diodes. *Chem. Mater.* **2004**, *16* (23), 4556–4573. https://doi.org/10.1021/cm049473l.

(19) Udhiarto, A.; Sister, Y.; Rini, S.; Asvial, M.; Munir, B. Effect of Hole Transport Layer and Electron Transport Layer on the Performance of a Single Emissive Layer Organic Light Emitting Diode. In *2015 International Conference on Quality in Research (QiR)*; IEEE: Lombok, Indonesia, 2015; pp 137–140. https://doi.org/10.1109/QiR.2015.7374913.

(20) Féry, C.; Racine, B.; Vaufrey, D.; Doyeux, H.; Cinà, S. Physical Mechanism Responsible for the Stretched Exponential Decay Behavior of Aging Organic Light-Emitting Diodes. *Appl. Phys. Lett.* **2005**, *87* (21), 213502. https://doi.org/10.1063/1.2133922.

(21) Schmidt, T. D.; Jäger, L.; Noguchi, Y.; Ishii, H.; Brütting, W. Analyzing Degradation Effects of Organic Light-Emitting Diodes via Transient Optical and Electrical Measurements. *Journal of Applied Physics* **2015**, *117* (21), 215502. https://doi.org/10.1063/1.4921829.

(22) Kondakov, D. Y.; Young, R. H. Variable Sensitivity of Organic Light-Emitting Diodes to Operation-Induced Chemical Degradation: Nature of the Antagonistic Relationship between Lifetime and Efficiency. *Journal of Applied Physics* **2010**, *108* (7), 074513. https://doi.org/10.1063/1.3483251.

(23) Scholz, S.; Kondakov, D.; Lüssem, B.; Leo, K. Degradation Mechanisms and Reactions in Organic Light-Emitting Devices. *Chem. Rev.* **2015**, *115* (16), 8449–8503. https://doi.org/10.1021/cr400704v.

(24) Tang, C. W.; VanSlyke, S. A. Organic Electroluminescent Diodes. 4.

(25) Duan, L.; Xie, K.; Qiu, Y. Review Paper: Progress on Efficient Cathodes for Organic Light-Emitting Diodes. *J. Soc. Inf. Display* **2011**, *19* (6), 453. https://doi.org/10.1889/JSID19.6.453.

(26) Adachi, C.; Baldo, M. A.; Forrest, S. R.; Lamansky, S.; Thompson, M. E.; Kwong, R. C. High-Efficiency Red Electrophosphorescence Devices. *Appl. Phys. Lett.* **2001**, *78* (11), 1622–1624. https://doi.org/10.1063/1.1355007.

(27) Kawamura, Y.; Yanagida, S.; Forrest, S. R. Energy Transfer in Polymer Electrophosphorescent Light Emitting Devices with Single and Multiple Doped Luminescent Layers. *Journal of Applied Physics* **2002**, *92* (1), 87–93. https://doi.org/10.1063/1.1479751.

(28) Zhou, X.; Qin, D. S.; Pfeiffer, M.; Blochwitz-Nimoth, J.; Werner, A.; Drechsel, J.; Maennig, B.; Leo, K.; Bold, M.; Erk, P.; Hartmann, H. High-Efficiency Electrophosphorescent Organic Light-Emitting Diodes with Double Light-Emitting Layers. *Appl. Phys. Lett.* **2002**, *81* (21), 4070–4072. https://doi.org/10.1063/1.1522495.

(29) Hung, L. S.; Tang, C. W.; Mason, M. G. Enhanced Electron Injection in Organic Electroluminescence Devices Using an Al/LiF Electrode. *Appl. Phys. Lett.* **1997**, *70* (2), 152–154. https://doi.org/10.1063/1.118344.
(30) Bolink, H. J.; Coronado, E.; Repetto, D.; Sessolo, M. Air Stable Hybrid Organic-Inorganic Light Emitting Diodes Using ZnO as the Cathode. *Appl. Phys. Lett.* **2007**, *91* (22), 223501. https://doi.org/10.1063/1.2809387.
(31) Pu, Y.-J.; Miyamoto, M.; Nakayama, K.; Oyama, T.; Masaaki, Y.; Kido, J. Lithium Phenolate Complexes for an Electron Injection Layer in Organic Light-Emitting Diodes. *Organic Electronics* **2009**, *10* (2), 228–232. https://doi.org/10.1016/j.orgel.2008.11.003.
(32) Kao, P.-C.; Lin, J.-H.; Wang, J.-Y.; Yang, C.-H.; Chen, S.-H. Improved Electron Injection into Alq3 Based OLEDs Using a Thin Lithium Carbonate Buffer Layer. *Synthetic Metals* **2010**, *160* (15–16), 1749–1753. https://doi.org/10.1016/j.synthmet.2010.06.012.
(33) Sasabe, H.; Kido, J. Low Molecular Weight Materials: Electron-Transport Materials. In *Handbook of Organic Light-Emitting Diodes*; Adachi, C., Hattori, R., Kaji, H., Tsujimura, T., Eds.; Springer Japan: Tokyo, 2019; pp 1–10. https://doi.org/10.1007/978-4-431-55761-6_51-1.
(34) Kotadiya, N. B.; Mondal, A.; Blom, P. W. M.; Andrienko, D.; Wetzelaer, G.-J. A. H. A Window to Trap-Free Charge Transport in Organic Semiconducting Thin Films. *Nat. Mater.* **2019**, *18* (11), 1182–1186. https://doi.org/10.1038/s41563-019-0473-6.
(35) Montes, V. A.; Pérez-Bolívar, C.; Estrada, L. A.; Shinar, J.; Anzenbacher, P. Ultrafast Dynamics of Triplet Excitons in Alq $_3$ -Bridge-Pt(II)Porphyrin Electroluminescent Materials. *J. Am. Chem. Soc.* **2007**, *129* (42), 12598–12599. https://doi.org/10.1021/ja073491x.
(36) O'Brien, D. F.; Baldo, M. A.; Thompson, M. E.; Forrest, S. R. Improved Energy Transfer in Electrophosphorescent Devices. *Appl. Phys. Lett.* **1999**, *74* (3), 442–444. https://doi.org/10.1063/1.123055.
(37) Baldo, M. A.; Lamansky, S.; Burrows, P. E.; Thompson, M. E.; Forrest, S. R. Very High-Efficiency Green Organic Light-Emitting Devices Based on Electrophosphorescence. *Appl. Phys. Lett.* **1999**, *75* (1), 4–6. https://doi.org/10.1063/1.124258.
(38) Keum, C.-M.; Kronenberg, N. M.; Murawski, C.; Yoshida, K.; Deng, Y.; Berz, C.; Li, W.; Wei, M.; Samuel, I. D. W.; Gather, M. C. The Role of Metallic Dopants in Improving the Thermal Stability of the Electron Transport Layer in Organic Light-Emitting Diodes. *Advanced Optical Materials* **2018**, *6* (17), 1800496. https://doi.org/10.1002/adom.201800496.
(39) Kotadiya, N. B.; Lu, H.; Mondal, A.; Ie, Y.; Andrienko, D.; Blom, P. W. M.; Wetzelaer, G.-J. A. H. Universal Strategy for Ohmic Hole Injection into Organic Semiconductors with High Ionization Energies. *Nature Mater* **2018**, *17* (4), 329–334. https://doi.org/10.1038/s41563-018-0022-8.
(40) Shirota, Y.; Kuwabaraa, Y.; Okuda, D.; Okuda, R.; Inada, H.; Kawamib, S.; Imaib, K. Starburst Molecules Based on X-Electron Systems as Materials for Organic Electroluminescent Devices. 7.
(41) Shahnawaz, S.; Sudheendran Swayamprabha, S.; Nagar, M. R.; Yadav, R. A. K.; Gull, S.; Dubey, D. K.; Jou, J.-H. Hole-Transporting Materials for Organic Light-Emitting Diodes: An Overview. *J. Mater. Chem. C* **2019**, *7* (24), 7144–7158. https://doi.org/10.1039/C9TC01712G.
(42) Martins, J. S.; Bartolomeu, A. A.; dos Santos, W. H.; da Silva Filho, L. C.; de Oliveira, E. F.; Lavarda, F. C.; Cuin, A.; Legnani, C.; Maciel, I. O.; Fragneaud, B.; Quirino, W. G. New Class of Organic Hole-Transporting Materials Based on Xanthene Derivatives for

Organic Electronic Applications. *J. Phys. Chem. C* **2017**, *121* (24), 12999–13007. https://doi.org/10.1021/acs.jpcc.7b02034.

(43) Zheng, Z.; Dong, Q.; Gou, L.; Su, J.-H.; Huang, J. Novel Hole Transport Materials Based on N,N′-Disubstituted-Dihydrophenazine Derivatives for Electroluminescent Diodes. *J. Mater. Chem. C* **2014**, *2* (46), 9858–9865. https://doi.org/10.1039/C4TC01965B.

(44) Zhang, Q.; Chen, J.; Cheng, Y.; Wang, L.; Ma, D.; Jing, X.; Wang, F. Novel Hole-Transporting Materials Based on 1,4-Bis(Carbazolyl)Benzene for Organic Light-Emitting Devices. *J. Mater. Chem.* **2004**, *14* (5), 895. https://doi.org/10.1039/b309630k.

(45) Schmidt, T. D.; Lampe, T.; Sylvinson M. R., D.; Djurovich, P. I.; Thompson, M. E.; Brütting, W. Emitter Orientation as a Key Parameter in Organic Light-Emitting Diodes. *Phys. Rev. Applied* **2017**, *8* (3), 037001. https://doi.org/10.1103/PhysRevApplied.8.037001.

(46) Moon, C.-K.; Kim, K.-H.; Lee, J. W.; Kim, J.-J. Influence of Host Molecules on Emitting Dipole Orientation of Phosphorescent Iridium Complexes. *Chem. Mater.* **2015**, *27* (8), 2767–2769. https://doi.org/10.1021/acs.chemmater.5b00469.

(47) Baldo, M. A.; O'Brien, D. F.; You, Y.; Shoustikov, A.; Sibley, S.; Thompson, M. E.; Forrest, S. R. Highly Efficient Phosphorescent Emission from Organic Electroluminescent Devices. **1998**, *395*, 4.

(48) Tung, Y.-L.; Wu, P.-C.; Liu, C.-S.; Chi, Y.; Yu, J.-K.; Hu, Y.-H.; Chou, P.-T.; Peng, S.-M.; Lee, G.-H.; Tao, Y.; Carty, A. J.; Shu, C.-F.; Wu, F.-I. Highly Efficient Red Phosphorescent Osmium(II) Complexes for OLED Applications. *Organometallics* **2004**, *23* (15), 3745–3748. https://doi.org/10.1021/om0498246.

(49) Fujii, H.; Sakurai, H.; Tani, K.; Wakisaka, K.; Hirao, T. Bright and Ultimately Pure Red Electrophosphorescent Diode Bearing Diphenylquinoxaline. *IEICE Electron. Express* **2005**, *2* (8), 260–266. https://doi.org/10.1587/elex.2.260.

(50) Kanno, H.; Ishikawa, K.; Nishio, Y.; Endo, A.; Adachi, C.; Shibata, K. Highly Efficient and Stable Red Phosphorescent Organic Light-Emitting Device Using Bis[2-(2-Benzothiazoyl)Phenolato]Zinc(II) as Host Material. *Appl. Phys. Lett.* **2007**, *90* (12), 123509. https://doi.org/10.1063/1.2643908.

(51) Meerheim, R.; Walzer, K.; Pfeiffer, M.; Leo, K. Ultrastable and Efficient Red Organic Light Emitting Diodes with Doped Transport Layers. *Appl. Phys. Lett.* **2006**, *89* (6), 061111. https://doi.org/10.1063/1.2268354.

(52) Li, H.-Y.; Zhou, L.; Teng, M.-Y.; Xu, Q.-L.; Lin, C.; Zheng, Y.-X.; Zuo, J.-L.; Zhang, H.-J.; You, X.-Z. Highly Efficient Green Phosphorescent OLEDs Based on a Novel Iridium Complex. *J. Mater. Chem. C* **2013**, *1* (3), 560–565. https://doi.org/10.1039/C2TC00052K.

(53) Tao, Y.; Wang, Q.; Yang, C.; Zhong, C.; Qin, J.; Ma, D. Multifunctional Triphenylamine/Oxadiazole Hybrid as Host and Exciton-Blocking Material: High Efficiency Green Phosphorescent OLEDs Using Easily Available and Common Materials. *Adv. Funct. Mater.* **2010**, *20* (17), 2923–2929. https://doi.org/10.1002/adfm.201000669.

(54) Chang, C.-H.; Kuo, M.-C.; Lin, W.-C.; Chen, Y.-T.; Wong, K.-T.; Chou, S.-H.; Mondal, E.; Kwong, R. C.; Xia, S.; Nakagawa, T.; Adachi, C. A Dicarbazole–Triazine Hybrid Bipolar Host Material for Highly Efficient Green Phosphorescent OLEDs. *J. Mater. Chem.* **2012**, *22* (9), 3832. https://doi.org/10.1039/c2jm14686j.

(55) Chen, H.-F.; Yang, S.-J.; Tsai, Z.-H.; Hung, W.-Y.; Wang, T.-C.; Wong, K.-T. 1,3,5-Triazine Derivatives as New Electron Transport–Type Host Materials for Highly Efficient Green Phosphorescent OLEDs. *J. Mater. Chem.* **2009**, *19* (43), 8112. https://doi.org/10.1039/b913423a.

(56) Wang, Y.; Wang, W.; Huang, Z.; Wang, H.; Zhao, J.; Yu, J.; Ma, D. High-Efficiency Red Organic Light-Emitting Diodes Based on a Double-Emissive Layer with an External Quantum Efficiency over 30%. *J. Mater. Chem. C* **2018**, *6* (26), 7042–7045. https://doi.org/10.1039/C8TC01639A.
(57) Yang, Q.; Hao, Y.; Wang, Z.; Li, Y.; Wang, H.; Xu, B. Double-Emission-Layer Green Phosphorescent OLED Based on LiF-Doped TPBi as Electron Transport Layer for Improving Efficiency and Operational Lifetime. *Synthetic Metals* **2012**, *162* (3–4), 398–401. https://doi.org/10.1016/j.synthmet.2011.12.027.
(58) Furue, R.; Matsuo, K.; Ashikari, Y.; Ooka, H.; Amanokura, N.; Yasuda, T. Highly Efficient Red-Orange Delayed Fluorescence Emitters Based on Strong π-Accepting Dibenzophenazine and Dibenzoquinoxaline Cores: Toward a Rational Pure-Red OLED Design. *Advanced Optical Materials* **2018**, *6* (5), 1701147. https://doi.org/10.1002/adom.201701147.
(59) Ni, F.; Wu, Z.; Zhu, Z.; Chen, T.; Wu, K.; Zhong, C.; An, K.; Wei, D.; Ma, D.; Yang, C. Teaching an Old Acceptor New Tricks: Rationally Employing 2,1,3-Benzothiadiazole as Input to Design a Highly Efficient Red Thermally Activated Delayed Fluorescence Emitter. *J. Mater. Chem. C* **2017**, *5* (6), 1363–1368. https://doi.org/10.1039/C7TC00025A.
(60) Wang, S.; Yan, X.; Cheng, Z.; Zhang, H.; Liu, Y.; Wang, Y. Highly Efficient Near-Infrared Delayed Fluorescence Organic Light Emitting Diodes Using a Phenanthrene-Based Charge-Transfer Compound. *Angew. Chem. Int. Ed.* **2015**, *54* (44), 13068–13072. https://doi.org/10.1002/anie.201506687.
(61) Wang, C.; Zheng, Y.-Q.; Tang, J.; Yu, J.-L.; Yang, F.; Wei, B.; Li, X.-F.; Zhang, J.-H. Highly Efficient Green TADF Organic Light-Emitting Diodes by Simultaneously Manipulating Hole and Electron Transport. *Nanotechnology* **2019**, *30* (11), 115201. https://doi.org/10.1088/1361-6528/aaf8c2.
(62) Tanaka, H.; Shizu, K.; Miyazaki, H.; Adachi, C. Efficient Green Thermally Activated Delayed Fluorescence (TADF) from a Phenoxazine–Triphenyltriazine (PXZ–TRZ) Derivative. *Chem. Commun.* **2012**, *48* (93), 11392. https://doi.org/10.1039/c2cc36237f.
(63) Kim, B. S.; Lee, J. Y. Engineering of Mixed Host for High External Quantum Efficiency above 25% in Green Thermally Activated Delayed Fluorescence Device. *Adv. Funct. Mater.* **2014**, *24* (25), 3970–3977. https://doi.org/10.1002/adfm.201303730.
(64) Im, Y.; Lee, J. Y. Recent Progress of Green Thermally Activated Delayed Fluorescent Emitters. *Journal of Information Display* **2017**, *18* (3), 101–117. https://doi.org/10.1080/15980316.2017.1333046.
(65) Seino, Y.; Inomata, S.; Sasabe, H.; Pu, Y.-J.; Kido, J. High-Performance Green OLEDs Using Thermally Activated Delayed Fluorescence with a Power Efficiency of over 100 Lm W^{-1}. *Adv. Mater.* **2016**, *28* (13), 2638–2643. https://doi.org/10.1002/adma.201503782.
(66) Seifert, R.; Rabelo de Moraes, I.; Scholz, S.; Gather, M. C.; Lüssem, B.; Leo, K. Chemical Degradation Mechanisms of Highly Efficient Blue Phosphorescent Emitters Used for Organic Light Emitting Diodes. *Organic Electronics* **2013**, *14* (1), 115–123. https://doi.org/10.1016/j.orgel.2012.10.003.
(67) Kim, S.; Bae, H. J.; Park, S.; Kim, W.; Kim, J.; Kim, J. S.; Jung, Y.; Sul, S.; Ihn, S.-G.; Noh, C.; Kim, S.; You, Y. Degradation of Blue-Phosphorescent Organic Light-Emitting Devices Involves Exciton-Induced Generation of Polaron Pair within Emitting Layers. *Nat Commun* **2018**, *9* (1), 1211. https://doi.org/10.1038/s41467-018-03602-4.
(68) Zhang, Y.; Aziz, H. Degradation Mechanisms in Blue Phosphorescent Organic Light-Emitting Devices by Exciton–Polaron Interactions: Loss in Quantum Yield versus Loss

in Charge Balance. *ACS Appl. Mater. Interfaces* **2017**, *9* (1), 636–643. https://doi.org/10.1021/acsami.6b13823.
(69) Song, W.; Lee, J. Y. Degradation Mechanism and Lifetime Improvement Strategy for Blue Phosphorescent Organic Light-Emitting Diodes. *Advanced Optical Materials* **2017**, *5* (9), 1600901. https://doi.org/10.1002/adom.201600901.
(70) Tanaka, M.; Nagata, R.; Nakanotani, H.; Adachi, C. Understanding Degradation of Organic Light-Emitting Diodes from Magnetic Field Effects. *Commun Mater* **2020**, *1* (1), 18. https://doi.org/10.1038/s43246-020-0019-0.
(71) van Eersel, H.; Bobbert, P. A.; Janssen, R. A. J.; Coehoorn, R. Monte Carlo Study of Efficiency Roll-off of Phosphorescent Organic Light-Emitting Diodes: Evidence for Dominant Role of Triplet-Polaron Quenching. *Appl. Phys. Lett.* **2014**, *105* (14), 143303. https://doi.org/10.1063/1.4897534.
(72) Zang, F. X.; Sum, T. C.; Huan, A. C. H.; Li, T. L.; Li, W. L.; Zhu, F. Reduced Efficiency Roll-off in Phosphorescent Organic Light Emitting Diodes at Ultrahigh Current Densities by Suppression of Triplet-Polaron Quenching. *Appl. Phys. Lett.* **2008**, *93* (2), 023309. https://doi.org/10.1063/1.2955527.
(73) Jeon, S. K.; Lee, J. Y. Four Times Lifetime Improvement of Blue Phosphorescent Organic Light-Emitting Diodes by Managing Recombination Zone. *Organic Electronics* **2015**, *27*, 202–206. https://doi.org/10.1016/j.orgel.2015.09.016.
(74) Baldo, M. A.; Adachi, C.; Forrest, S. R. Transient Analysis of Organic Electrophosphorescence. II. Transient Analysis of Triplet-Triplet Annihilation. *Phys. Rev. B* **2000**, *62* (16), 10967–10977. https://doi.org/10.1103/PhysRevB.62.10967.
(75) Reineke, S.; Schwartz, G.; Walzer, K.; Leo, K. Reduced Efficiency Roll-off in Phosphorescent Organic Light Emitting Diodes by Suppression of Triplet-Triplet Annihilation. *Appl. Phys. Lett.* **2007**, *91* (12), 123508. https://doi.org/10.1063/1.2786840.
(76) Luo, Y.; Aziz, H. Probing Triplet-Triplet Annihilation Zone and Determining Triplet Exciton Diffusion Length by Using Delayed Electroluminescence. *Journal of Applied Physics* **2010**, *107* (9), 094510. https://doi.org/10.1063/1.3410678.
(77) May, F.; Al-Helwi, M.; Baumeier, B.; Kowalsky, W.; Fuchs, E.; Lennartz, C.; Andrienko, D. Design Rules for Charge-Transport Efficient Host Materials for Phosphorescent Organic Light-Emitting Diodes. *J. Am. Chem. Soc.* **2012**, *134* (33), 13818–13822. https://doi.org/10.1021/ja305310r.
(78) Hirata, S.; Sakai, Y.; Masui, K.; Tanaka, H.; Lee, S. Y.; Nomura, H.; Nakamura, N.; Yasumatsu, M.; Nakanotani, H.; Zhang, Q.; Shizu, K.; Miyazaki, H.; Adachi, C. Highly Efficient Blue Electroluminescence Based on Thermally Activated Delayed Fluorescence. *Nature Materials* **2015**, *14* (3), 330–336. https://doi.org/10.1038/nmat4154.
(79) Uoyama, H.; Goushi, K.; Shizu, K.; Nomura, H.; Adachi, C. Highly Efficient Organic Light-Emitting Diodes from Delayed Fluorescence. *Nature* **2012**, *492* (7428), 234–238. https://doi.org/10.1038/nature11687.
(80) Bui, T.-T.; Goubard, F.; Ibrahim-Ouali, M.; Gigmes, D.; Dumur, F. Recent Advances on Organic Blue Thermally Activated Delayed Fluorescence (TADF) Emitters for Organic Light-Emitting Diodes (OLEDs). *Beilstein J. Org. Chem.* **2018**, *14*, 282–308. https://doi.org/10.3762/bjoc.14.18.
(81) dos Santos, P. L.; Ward, J. S.; Bryce, M. R.; Monkman, A. P. Using Guest–Host Interactions To Optimize the Efficiency of TADF OLEDs. *J. Phys. Chem. Lett.* **2016**, *7* (17), 3341–3346. https://doi.org/10.1021/acs.jpclett.6b01542.
(82) Jankus, V.; Data, P.; Graves, D.; McGuinness, C.; Santos, J.; Bryce, M. R.; Dias, F. B.; Monkman, A. P. Highly Efficient TADF OLEDs: How the Emitter-Host Interaction Controls Both the Excited State Species and Electrical Properties of the Devices to

Achieve Near 100% Triplet Harvesting and High Efficiency. *Adv. Funct. Mater.* **2014**, *24* (39), 6178–6186. https://doi.org/10.1002/adfm.201400948.

(83) Rajamalli, P.; Senthilkumar, N.; Gandeepan, P.; Ren-Wu, C.-C.; Lin, H.-W.; Cheng, C.-H. A Method for Reducing the Singlet–Triplet Energy Gaps of TADF Materials for Improving the Blue OLED Efficiency. *ACS Appl. Mater. Interfaces* **2016**, *8* (40), 27026–27034. https://doi.org/10.1021/acsami.6b10678.

(84) Cai, M.; Zhang, D.; Duan, L. High Performance Thermally Activated Delayed Fluorescence Sensitized Organic Light-Emitting Diodes. *Chem. Rec.* **2019**, *19* (8), 1611–1623. https://doi.org/10.1002/tcr.201800148.

(85) Nakanotani, H.; Higuchi, T.; Furukawa, T.; Masui, K.; Morimoto, K.; Numata, M.; Tanaka, H.; Sagara, Y.; Yasuda, T.; Adachi, C. High-Efficiency Organic Light-Emitting Diodes with Fluorescent Emitters. *Nat Commun* **2014**, *5* (1), 4016. https://doi.org/10.1038/ncomms5016.

(86) Lee, K. H.; Lee, J. Y. Phosphor Sensitized Thermally Activated Delayed Fluorescence Organic Light-Emitting Diodes with Ideal Deep Blue Device Performances. *J. Mater. Chem. C* **2019**, *7* (28), 8562–8568. https://doi.org/10.1039/C9TC02746G.

(87) Baldo, M. A.; Thompson, M. E.; Forrest, S. R. High-Efficiency Fluorescent Organic Light-Emitting Devices Using a Phosphorescent Sensitizer. *Nature* **2000**, *403* (6771), 750–753. https://doi.org/10.1038/35001541.

(88) D'Andrade, B. W.; Baldo, M. A.; Adachi, C.; Brooks, J.; Thompson, M. E.; Forrest, S. R. High-Efficiency Yellow Double-Doped Organic Light-Emitting Devices Based on Phosphor-Sensitized Fluorescence. *Appl. Phys. Lett.* **2001**, *79* (7), 1045–1047. https://doi.org/10.1063/1.1388159.

(89) Lei, G.; Wang, L.; Qiu, Y. Blue Phosphorescent Dye as Sensitizer and Emitter for White Organic Light-Emitting Diodes. *Appl. Phys. Lett.* **2004**, *85* (22), 5403–5405. https://doi.org/10.1063/1.1827326.

(90) Cheng, G.; Zhang, Y.; Zhao, Y.; Liu, S.; Ma, Y. Improved Efficiency for White Organic Light-Emitting Devices Based on Phosphor Sensitized Fluorescence. *Appl. Phys. Lett.* **2006**, *88* (8), 083512. https://doi.org/10.1063/1.2178478.

(91) Kanno, H.; Sun, Y.; Forrest, S. R. White Organic Light-Emitting Device Based on a Compound Fluorescent-Phosphor-Sensitized-Fluorescent Emission Layer. *Appl. Phys. Lett.* **2006**, *89* (14), 143516. https://doi.org/10.1063/1.2357038.

(92) Eickhoff, C.; Murer, P.; Geßner, T.; Birnstock, J.; Kröger, M.; Choi, Z.; Watanabe, S.; May, F.; Lennartz, C.; Stengel, I.; Münster, I.; Kahle, K.; Wagenblast, G.; Mangold, H. Long-Lived and Highly Efficient Green and Blue Phosphorescent Emitters and Device Architectures for OLED Displays. In *Organic Light Emitting Materials and Devices XIX*; International Society for Optics and Photonics, 2015; Vol. 9566, p 95662N. https://doi.org/10.1117/12.2199079.

(93) Heimel, P.; Mondal, A.; May, F.; Kowalsky, W.; Lennartz, C.; Andrienko, D.; Lovrincic, R. Unicolored Phosphor-Sensitized Fluorescence for Efficient and Stable Blue OLEDs. *Nature Communications* **2018**, *9* (1). https://doi.org/10.1038/s41467-018-07432-2.

(94) Chen, S.; Deng, L.; Xie, J.; Peng, L.; Xie, L.; Fan, Q.; Huang, W. Recent Developments in Top-Emitting Organic Light-Emitting Diodes. *Adv. Mater.* **2010**, *22* (46), 5227–5239. https://doi.org/10.1002/adma.201001167.

(95) Hofmann, S.; Thomschke, M.; Freitag, P.; Furno, M.; Lüssem, B.; Leo, K. Top-Emitting Organic Light-Emitting Diodes: Influence of Cavity Design. *Appl. Phys. Lett.* **2010**, *97* (25), 253308. https://doi.org/10.1063/1.3530447.

(96) Riel, H.; Karg, S.; Beierlein, T.; Rieß, W.; Neyts, K. Tuning the Emission Characteristics of Top-Emitting Organic Light-Emitting Devices by Means of a Dielectric Capping Layer: An Experimental and Theoretical Study. *J. Appl. Phys.* **2003**, *94* (8), 8.

(97) Meyer, J.; Winkler, T.; Hamwi, S.; Schmale, S.; Kröger, M.; Görrn, P.; Johannes, H.-H.; Riedl, T.; Lang, E.; Becker, D.; Dobbertin, T.; Kowalsky, W. Highly Efficient Fully Transparent Inverted OLEDs; Kafafi, Z. H., So, F., Eds.; San Diego, CA, 2007; p 66550L. https://doi.org/10.1117/12.734051.
(98) Chen, Y.; Wei, X.; Li, Z.; Liu, Y.; Liu, J.; Wang, R.; Wang, P.; Yamada-Takamura, Y.; Wang, Y. N-Doping-Induced Efficient Electron-Injection for High Efficiency Inverted Organic Light-Emitting Diodes Based on Thermally Activated Delayed Fluorescence Emitter. *J. Mater. Chem. C* **2017**, *5* (33), 8400–8407. https://doi.org/10.1039/C7TC02406A.
(99) Jetly, A.; Mehra, R. Efficient Tandem Organic Light Emitting Diode Using Organic Photovoltaic Charge Generation Layer. *International Journal of Optics* **2018**, *2018*, 1–10. https://doi.org/10.1155/2018/9458530.
(100) Fröbel, M.; Fries, F.; Schwab, T.; Lenk, S.; Leo, K.; Gather, M. C.; Reineke, S. Three-Terminal RGB Full-Color OLED Pixels for Ultrahigh Density Displays. *Sci Rep* **2018**, *8* (1), 9684. https://doi.org/10.1038/s41598-018-27976-z.
(101) Gustafsson, G.; Cao, Y.; Treacy, G. M.; Klavetter, F.; Colaneri, N.; Heeger, A. J. Flexible Light-Emitting Diodes Made from Soluble Conducting Polymers. *Nature* **1992**, *357* (6378), 477–479. https://doi.org/10.1038/357477a0.
(102) Lee, C.-C. Modeling and Validation of Mechanical Stress in Indium Tin Oxide Layer Integrated in Highly Flexible Stacked Thin Films. *Thin Solid Films* **2013**, *544*, 443–447. https://doi.org/10.1016/j.tsf.2013.02.084.
(103) Lee, C.-C.; Shih, Y.-S.; Wu, C.-S.; Tsai, C.-H.; Yeh, S.-T.; Peng, Y.-H.; Chen, K.-J. Development of Robust Flexible OLED Encapsulations Using Simulated Estimations and Experimental Validations. *J. Phys. D: Appl. Phys.* **2012**, *45* (27), 275102. https://doi.org/10.1088/0022-3727/45/27/275102.
(104) Chiang, C.-J.; Winscom, C.; Bull, S.; Monkman, A. Mechanical Modeling of Flexible OLED Devices. *Organic Electronics* **2009**, *10* (7), 1268–1274. https://doi.org/10.1016/j.orgel.2009.07.003.
(105) Transparent OLEDs (TOLEDs); Universal Display Corporation. https://oled.com/oleds/transparent-oleds-toleds/.
(106) Lee, J.; Hofmann, S.; Furno, M.; Thomschke, M.; Kim, Y. H.; Lüssem, B.; Leo, K. Influence of Organic Capping Layers on the Performance of Transparent Organic Light-Emitting Diodes. 3.
(107) Chung, J.; Cho, H.; Koh, T.-W.; Lee, J.; Kim, E.; Lee, J.; Lee, J.-I.; Yoo, S. Towards Highly Efficient and Highly Transparent OLEDs: Advanced Considerations for Emission Zone Coupled with Capping Layer Design. **2015**, 9.
(108) HOW OLEDs Work: PMOLEDs and AMOLEDs. https://electronics.howstuffworks.com/oled3.htm.
(109) Dynamic AMOLED Technology; Samsung Display:Mobile Devices. https://www.samsung.com/global/galaxy/what-is/dynamic-amoled/.
(110) Samsung Galaxy Fold. https://www.samsung.com/global/galaxy/galaxy-fold/.
(111) LG AMOLED Used for the Apple Smartwatch Display. https://www.oled-info.com/confirmed-apples-watch-uses-amoled-display.
(112) LG OLED Technology for TV Applications and the Advantages They Have. https://www.lg.com/global/business/technology-solution-oled.
(113) OLED (Organic LED): A Top Lighting Trend for Automotive Lighting OLED: Organic LED Is the Future Light Technology for Car Lighting. https://www.osram.com/am/specials/trends-in-automotive-lighting/oled-panel-lighting/oled-organic-led-a-top-lighting-trend-for-automotive-lighting/index.jsp.

(114) Osram Presents Flexible OLEDs for Vehicle Lighting. https://www.osram-group.com/media/press-releases/pr-2016/05-07-2016.
(115) Osram Brings Transparent OLEDs to Industry Maturity. https://www.osram-group.com/en/media/press-releases/pr-2012/13-12-2012.
(116) Coehoorn, R.; van Eersel, H.; Bobbert, P.; Janssen, R. Kinetic Monte Carlo Study of the Sensitivity of OLED Efficiency and Lifetime to Materials Parameters. *Adv. Funct. Mater.* **2015**, *25* (13), 2024–2037. https://doi.org/10.1002/adfm.201402532.
(117) Cottaar, J.; Coehoorn, R.; Bobbert, P. A. Modeling of Charge Transport across Disordered Organic Heterojunctions. *Organic Electronics* **2012**, *13* (4), 667–672. https://doi.org/10.1016/j.orgel.2012.01.013.
(118) Kordt, P.; van der Holst, J. J. M.; Al Helwi, M.; Kowalsky, W.; May, F.; Badinski, A.; Lennartz, C.; Andrienko, D. Modeling of Organic Light Emitting Diodes: From Molecular to Device Properties. *Adv. Funct. Mater.* **2015**, *25* (13), 1955–1971. https://doi.org/10.1002/adfm.201403004.
(119) Friederich, P.; Fediai, A.; Kaiser, S.; Konrad, M.; Jung, N.; Wenzel, W. Toward Design of Novel Materials for Organic Electronics. *Adv. Mater.* **2019**, *31* (26), 1808256. https://doi.org/10.1002/adma.201808256.
(120) Baumeier, B.; May, F.; Lennartz, C.; Andrienko, D. Challenges for in Silico Design of Organic Semiconductors. *J. Mater. Chem.* **2012**, *22* (22), 10971. https://doi.org/10.1039/c2jm30182b.
(121) Andrienko, D. CHAPTER 9. Simulations of Morphology and Charge Transport in Supramolecular Organic Materials. In *Smart Materials Series*; Koch, N., Ed.; Royal Society of Chemistry: Cambridge, 2014; pp 309–362. https://doi.org/10.1039/9781782626947-00309.
(122) Schrödinger, E. An Undulatory Theory of the Mechanics of Atoms and Molecules. *Physical Review* **1926**, *28* (6), 1049–1070. https://doi.org/10.1103/PhysRev.28.1049.
(123) Born, M.; Oppenheimer, R. Zur Quantentheorie der Molekeln. *Ann. Phys.* **1927**, *389* (20), 457–484. https://doi.org/10.1002/andp.19273892002.
(124) Cramer, Christopher. J. *Essentials of Computational Chemistry Theories and Models*, Second Edition.; Wiley-VCH ; John Wiley, 2007.
(125) Hartree, D. R. The Wave Mechanics of an Atom with a Non-Coulomb Central Field. Part I. Theory and Methods. *Math. Proc. Camb. Phil. Soc.* **1928**, *24* (1), 89–110. https://doi.org/10.1017/S0305004100011919.
(126) Fock, V. Näherungsmethode Zur Lösung Des Quantenmechanischen Mehrkörperproblems (Approximation Method for Solving the Quantum Mechanical Multibody Problem). *Zeitschrift für Physik* **1930**, *61*, 126–148. https://doi.org/10.1007/BF01340294.
(127) Slater, J. C. A Simplification of the Hartree-Fock Method. *Phys. Rev.* **1951**, *81* (3), 385–390. https://doi.org/10.1103/PhysRev.81.385.
(128) Roothaan, C. C. J. New Developments in Molecular Orbital Theory. *Rev. Mod. Phys.* **1951**, *23* (2), 69–89. https://doi.org/10.1103/RevModPhys.23.69.
(129) Shavitt, I. The History and Evolution of Configuration Interaction. *Mol. Phys.* **1998**, *94* (1), 3–17. https://doi.org/10.1080/00268979809482290.
(130) Møller, Chr.; Plesset, M. S. Note on an Approximation Treatment for Many-Electron Systems. *Phys. Rev.* **1934**, *46* (7), 618–622. https://doi.org/10.1103/PhysRev.46.618.
(131) Bartlett, R. J.; Musiał, M. Coupled-Cluster Theory in Quantum Chemistry. *Rev. Mod. Phys.* **2007**, *79* (1), 291–352. https://doi.org/10.1103/RevModPhys.79.291.
(132) Hohenberg, P.; Kohn, W. Inhomogeneous Electron Gas. *Phys. Rev.* **1964**, *136* (3B), B864–B871. https://doi.org/10.1103/PhysRev.136.B864.

(133) Kohn, W.; Sham, L. J. Quantum Density Oscillations in an Inhomogeneous Electron Gas. *Phys. Rev.* **1965**, *137* (6A), A1697–A1705. https://doi.org/10.1103/PhysRev.137.A1697.
(134) Kohn, W.; Sham, L. J. Self-Consistent Equations Including Exchange and Correlation Effects. *Phys. Rev.* **1965**, *140* (4A), A1133–A1138. https://doi.org/10.1103/PhysRev.140.A1133.
(135) Becke, A. D. Density-functional Thermochemistry. III. The Role of Exact Exchange. *The Journal of Chemical Physics* **1993**, *98* (7), 5648–5652. https://doi.org/10.1063/1.464913.
(136) Lee, C.; Yang, W.; Parr, R. G. Development of the Colle-Salvetti Correlation-Energy Formula into a Functional of the Electron Density. *Phys. Rev. B* **1988**, *37* (2), 785–789. https://doi.org/10.1103/PhysRevB.37.785.
(137) Perdew, J. P.; Ernzerhof, M.; Burke, K. Rationale for Mixing Exact Exchange with Density Functional Approximations. *The Journal of Chemical Physics* **1996**, *105* (22), 9982–9985. https://doi.org/10.1063/1.472933.
(138) Stephens, P. J.; Devlin, F. J.; Chabalowski, C. F.; Frisch, M. J. Ab Initio Calculation of Vibrational Absorption and Circular Dichroism Spectra Using Density Functional Force Fields. *J. Phys. Chem.* **1994**, *98* (45), 11623–11627. https://doi.org/10.1021/j100096a001.
(139) Frenkel, D.; Smit, B. *Understanding Molecular Simulations: From Algorithms to Applications*, 2nd ed.; Computational science series; Academic Press: San Diego, CA, 2002.
(140) *Computational Soft Matter: From Synthetic Polymers to Proteins; Winter School, 29 February - 6 March 2004, Gustav-Stresemann-Institut, Bonn, Germany. 2: Lecture Notes*; Gustav-Stresemann-Institut e.V. für Übernationale Bildung und Europäische Zusammenarbeit, John von Neumann-Institut für Computing, Johannes Gutenberg-Universität Mainz, Max-Planck-Institut für Biophysikalische Chemie, Max-Planck-Institut für Polymerforschung, Eds.; NIC series; NIC: Jülich, 2004.
(141) Berendsen, H. J. C.; Postma, J. P. M.; van Gunsteren, W. F.; DiNola, A.; Haak, J. R. Molecular Dynamics with Coupling to an External Bath. *The Journal of Chemical Physics* **1984**, *81* (8), 3684–3690. https://doi.org/10.1063/1.448118.
(142) Andersen, H. C. Molecular Dynamics Simulations at Constant Pressure and/or Temperature. *The Journal of Chemical Physics* **1980**, *72* (4), 2384–2393. https://doi.org/10.1063/1.439486.
(143) Nosé, S. A Unified Formulation of the Constant Temperature Molecular Dynamics Methods. *The Journal of Chemical Physics* **1984**, *81* (1), 511–519. https://doi.org/10.1063/1.447334.
(144) Hoover, W. G. Canonical Dynamics: Equilibrium Phase-Space Distributions. *Phys. Rev. A* **1985**, *31* (3), 1695–1697. https://doi.org/10.1103/PhysRevA.31.1695.
(145) Bussi, G.; Donadio, D.; Parrinello, M. Canonical Sampling through Velocity Rescaling. *The Journal of Chemical Physics* **2007**, *126* (1), 014101. https://doi.org/10.1063/1.2408420.
(146) Tkatchenko, A.; DiStasio, R. A.; Car, R.; Scheffler, M. Accurate and Efficient Method for Many-Body van Der Waals Interactions. *Phys. Rev. Lett.* **2012**, *108* (23), 236402. https://doi.org/10.1103/PhysRevLett.108.236402.
(147) Rühle, V.; Lukyanov, A.; May, F.; Schrader, M.; Vehoff, T.; Kirkpatrick, J.; Baumeier, B.; Andrienko, D. Microscopic Simulations of Charge Transport in Disordered Organic Semiconductors. *J. Chem. Theory Comput.* **2011**, *7* (10), 3335–3345. https://doi.org/10.1021/ct200388s.

(148) Rühle, V.; Junghans, C.; Lukyanov, A.; Kremer, K.; Andrienko, D. Versatile Object-Oriented Toolkit for Coarse-Graining Applications. *J. Chem. Theory Comput.* **2009**, *5* (12), 3211–3223. https://doi.org/10.1021/ct900369w.
(149) Andrienko, D. Multiscale Concepts in Simulations of Organic Semiconductors. In *Handbook of Materials Modeling*; Andreoni, W., Yip, S., Eds.; Springer International Publishing: Cham, 2018; pp 1–12. https://doi.org/10.1007/978-3-319-42913-7_39-1.
(150) Ewald, P. P. Die Berechnung optischer und elektrostatischer Gitterpotentiale. *Ann. Phys.* **1921**, *369* (3), 253–287. https://doi.org/10.1002/andp.19213690304.
(151) Electrostatic Energy in Ionic Crystals. 31.
(152) Darden, T.; York, D.; Pedersen, L. Particle Mesh Ewald: An $N \cdot \log(N)$ Method for Ewald Sums in Large Systems. *The Journal of Chemical Physics* **1993**, *98* (12), 10089–10092. https://doi.org/10.1063/1.464397.
(153) Essmann, U.; Perera, L.; Berkowitz, M. L.; Darden, T.; Lee, H.; Pedersen, L. G. A Smooth Particle Mesh Ewald Method. *The Journal of Chemical Physics* **1995**, *103* (19), 8577–8593. https://doi.org/10.1063/1.470117.
(154) Stone, A. J.; Alderton, M. Distributed Multipole Analysis: Methods and Applications. *Molecular Physics* **1985**, *56* (5), 1047–1064. https://doi.org/10.1080/00268978500102891.
(155) Stone, A. J. Distributed Multipole Analysis: Stability for Large Basis Sets. 5.
(156) Breneman, C. M.; Wiberg, K. B. Determining Atom-Centered Monopoles from Molecular Electrostatic Potentials. The Need for High Sampling Density in Formamide Conformational Analysis. *J. Comput. Chem.* **1990**, *11* (3), 361–373. https://doi.org/10.1002/jcc.540110311.
(157) Singh, U. C.; Kollman, P. A. An Approach to Computing Electrostatic Charges for Molecules. *J. Comput. Chem.* **1984**, *5* (2), 129–145. https://doi.org/10.1002/jcc.540050204.
(158) Charges Fit to Electrostatic Potentials. II. Can Atomic Charges Be Unambiguously Fit to Electrostatic Potentials? *JOURNAL OF COMPUTATIONAL CHEMISTRY 17* (3), 17.
(159) Thole, B. T. Molecular Polarizabilities Calculated with a Modified Dipole Interaction. *Chem. Phys.* **1981**, *59* (3), 341–350. https://doi.org/10.1016/0301-0104(81)85176-2.
(160) Thole, B. T. Molecular Polarizabilities Calculated with a Modified Dipole Interaction. *Chemical Physics* **1981**, No. 3, 341–350. https://doi.org/10.1016/0301-0104(81)85176-2.
(161) van Duijnen, P. Th.; Swart, M. Molecular and Atomic Polarizabilities: Thole's Model Revisited. *J. Phys. Chem. A* **1998**, *102* (14), 2399–2407. https://doi.org/10.1021/jp980221f.
(162) Rühle, V.; Lukyanov, A.; May, F.; Schrader, M.; Vehoff, T.; Kirkpatrick, J.; Baumeier, B.; Andrienko, D. Microscopic Simulations of Charge Transport in Disordered Organic Semiconductors. *J. Chem. Theory Comput.* **2011**, *7* (10), 3335–3345. https://doi.org/10.1021/ct200388s.
(163) May, V.; Kühn, O. *Charge and Energy Transfer Dynamics in Molecular Systems*, 2nd, rev.enl. ed ed.; Wiley-VCH ; John Wiley: Weinheim : Chichester, 2004.
(164) Kirkpatrick, J. An Approximate Method for Calculating Transfer Integrals Based on the ZINDO Hamiltonian. *Int. J. Quantum Chem.* **2008**, *108* (1), 51–56. https://doi.org/10.1002/qua.21378.
(165) Ridley, J.; Zerner, M. An Intermediate Neglect of Differential Overlap Technique for Spectroscopy: Pyrrole and the Azines. *Theoret. Chim. Acta* **1973**, *32* (2), 111–134. https://doi.org/10.1007/BF00528484.

(166) Bacon, A. D.; Zerner, M. C. An Intermediate Neglect of Differential Overlap Theory for Transition Metal Complexes: Fe, Co and Cu Chlorides. *Theoret. Chim. Acta* **1979**, *53* (1), 21–54. https://doi.org/10.1007/BF00547605.
(167) Baumeier, B.; Kirkpatrick, J.; Andrienko, D. Density-Functional Based Determination of Intermolecular Charge Transfer Properties for Large-Scale Morphologies. *Phys. Chem. Chem. Phys.* **2010**, *12* (36), 11103. https://doi.org/10.1039/c002337j.
(168) Marcus, R. A. Electron Transfer Reactions in Chemistry. Theory and Experiment. *Rev. Mod. Phys.* **1993**, *65* (3), 599–610. https://doi.org/10.1103/RevModPhys.65.599.
(169) Marcus, R. A. Chemical and Electrochemical Electron-Transfer Theory. *Annu. Rev. Phys. Chem.* **1964**, *15* (1), 155–196. https://doi.org/10.1146/annurev.pc.15.100164.001103.
(170) Marcus, R. A.; Sutin, N. Electron Transfers in Chemistry and Biology. *Biophys. Acta* **1985**, *811* (3), 265–322. https://doi.org/10.1016/0304-4173(85)90014-X.
(171) Hutchison, G. R.; Ratner, M. A.; Marks, T. J. Hopping Transport in Conductive Heterocyclic Oligomers: Reorganization Energies and Substituent Effects. *J. Am. Chem. Soc.* **2005**, *127* (7), 2339–2350. https://doi.org/10.1021/ja0461421.
(172) Egger, R.; Mak, C. H.; Weiss, U. Quantum Rates for Nonadiabatic Electron Transfer. *The Journal of Chemical Physics* **1994**, *100* (4), 2651–2660. https://doi.org/10.1063/1.466460.
(173) Grabert, H.; Weiss, U. Thermal Enhancement of the Quantum Decay Rate in a Dissipative System. *Z. Physik B - Condensed Matter* **1984**, *56* (2), 171–183. https://doi.org/10.1007/BF01469699.
(174) Grabert, H.; Weiss, U. Quantum Tunneling Rates for Asymmetric Double-Well Systems with Ohmic Dissipation. *Phys. Rev. Lett.* **1985**, *54* (15), 1605–1608. https://doi.org/10.1103/PhysRevLett.54.1605.
(175) Fisher, M. P. A.; Dorsey, A. T. Dissipative Quantum Tunneling in a Biased Double-Well System at Finite Temperatures. *Phys. Rev. Lett.* **1985**, *54* (15), 1609–1612. https://doi.org/10.1103/PhysRevLett.54.1609.
(176) Grabert, H.; Olschowski, P.; Weiss, U. Quantum Decay Rates for Dissipative Systems at Finite Temperatures. *Phys. Rev. B* **1987**, *36* (4), 1931–1951. https://doi.org/10.1103/PhysRevB.36.1931.
(177) Miller, A.; Abrahams, E. Impurity Conduction at Low Concentrations. *Phys. Rev.* **1960**, *120* (3), 745–755. https://doi.org/10.1103/PhysRev.120.745.
(178) Coropceanu, V.; Cornil, J.; da Silva Filho, D. A.; Olivier, Y.; Silbey, R.; Brédas, J.-L. Charge Transport in Organic Semiconductors. *Chem. Rev.* **2007**, *107* (4), 926–952. https://doi.org/10.1021/cr050140x.
(179) Bässler, H. Charge Transport in Disordered Organic Photoconductors a Monte Carlo Simulation Study. *phys. stat. sol. (b)* **1993**, *175* (1), 15–56. https://doi.org/10.1002/pssb.2221750102.
(180) Dunlap, D. H.; Parris, P. E.; Kenkre, V. M. Charge-Dipole Model for the Universal Field Dependence of Mobilities in Molecularly Doped Polymers. *Phys. Rev. Lett.* **1996**, *77* (3), 542–545. https://doi.org/10.1103/PhysRevLett.77.542.
(181) Novikov, S. V.; Dunlap, D. H.; Kenkre, V. M.; Parris, P. E.; Vannikov, A. V. Essential Role of Correlations in Governing Charge Transport in Disordered Organic Materials. *Phys. Rev. Lett.* **1998**, *81* (20), 4472–4475. https://doi.org/10.1103/PhysRevLett.81.4472.
(182) Bouhassoune, M.; Mensfoort, S. L. M. van; Bobbert, P. A.; Coehoorn, R. Carrier-Density and Field-Dependent Charge-Carrier Mobility in Organic Semiconductors with Correlated Gaussian Disorder. *Organic Electronics* **2009**, *10* (3), 437–445. https://doi.org/10.1016/j.orgel.2009.01.005.

(183) Frenkel, J. On Pre-Breakdown Phenomena in Insulators and Electronic Semi-Conductors. *Phys. Rev.* **1938**, *54* (8), 647–648. https://doi.org/10.1103/PhysRev.54.647.
(184) Jansen, A. P. J. An Introduction To Monte Carlo Simulations Of Surface Reactions. *arXiv:cond-mat/0303028* **2003**.
(185) Gillespie, D. T. A General Method for Numerically Simulating the Stochastic Time Evolution of Coupled Chemical Reactions. *Journal of computational physics* **1976**, *22*, 403–434.
(186) Gillespie, D. T. Exact Stochastic Simulation of Coupled Chemical Reactions. *J. Phys. Chem.* **1977**, *81* (25), 2340–2361. https://doi.org/10.1021/j100540a008.
(187) Young, W. M.; Elcock, E. W. Monte Carlo Studies of Vacancy Migration in Binary Ordered Alloys: I. *Proc. Phys. Soc.* **1966**, *89* (3), 735–746. https://doi.org/10.1088/0370-1328/89/3/329.
(188) Bortz, A. B.; Kalos, M. H.; Lebowitz, J. L. A New Algorithm for Monte Carlo Simulation of King Spin Systems. *MONTE CARLO SIMULATION* 9.
(189) Fichthorn, K. A.; Weinberg, W. H. Theoretical Foundations of Dynamical Monte Carlo Simulations. *The Journal of Chemical Physics* **1991**, *95* (2), 1090–1096. https://doi.org/10.1063/1.461138.
(190) Jansen, A. P. J. Monte Carlo Simulations of Chemical Reactions on a Surface with Time-Dependent Reaction-Rate Constants. *Computer Physics Communications* **1995**, *86* (1–2), 1–12. https://doi.org/10.1016/0010-4655(94)00155-U.
(191) Nikitenko, V. R.; von Seggern, H. Nonequilibrium Transport of Charge Carriers and Transient Electroluminescence in Organic Light-Emitting Diodes. *Journal of Applied Physics* **2007**, *102* (10), 103708. https://doi.org/10.1063/1.2811926.
(192) Borsenberger, P. M.; Magin, E. H.; Van Auweraer, M. D.; De Schryver, F. C. The Role of Disorder on Charge Transport in Molecularly Doped Polymers and Related Materials. *Phys. Stat. Sol. (a)* **1993**, *140* (1), 9–47. https://doi.org/10.1002/pssa.2211400102.
(193) Scher, H.; Montroll, E. W. Anomalous Transit-Time Dispersion in Amorphous Solids. *Phys. Rev. B* **1975**, *12* (6), 2455–2477. https://doi.org/10.1103/PhysRevB.12.2455.
(194) Lukyanov, A.; Andrienko, D. Extracting Nondispersive Charge Carrier Mobilities of Organic Semiconductors from Simulations of Small Systems. *Phys. Rev. B* **2010**, *82* (19), 193202. https://doi.org/10.1103/PhysRevB.82.193202.
(195) Seki, K.; Tachiya, M. Electric Field Dependence of Charge Mobility in Energetically Disordered Materials: Polaron Aspects. *Phys. Rev. B* **2001**, *65* (1), 014305. https://doi.org/10.1103/PhysRevB.65.014305.
(196) Paterson, L.; Mondal, A.; Heimel, P.; Lovrincic, R.; May, F.; Lennartz, C.; Andrienko, D. Perspectives of Unicolored Phosphor-Sensitized Fluorescence. *Adv. Electron. Mater.* **2019**, *5* (12), 1900646. https://doi.org/10.1002/aelm.201900646.
(197) Seifert, R.; Rabelo de Moraes, I.; Scholz, S.; Gather, M. C.; Lüssem, B.; Leo, K. Chemical Degradation Mechanisms of Highly Efficient Blue Phosphorescent Emitters Used for Organic Light Emitting Diodes. *Organic Electronics* **2013**, *14* (1), 115–123. https://doi.org/10.1016/j.orgel.2012.10.003.
(198) Hirata, S.; Sakai, Y.; Masui, K.; Tanaka, H.; Lee, S. Y.; Nomura, H.; Nakamura, N.; Yasumatsu, M.; Nakanotani, H.; Zhang, Q.; Shizu, K.; Miyazaki, H.; Adachi, C. Highly Efficient Blue Electroluminescence Based on Thermally Activated Delayed Fluorescence. *Nature Materials* **2015**, *14* (3), 330–336. https://doi.org/10.1038/nmat4154.
(199) Uoyama, H.; Goushi, K.; Shizu, K.; Nomura, H.; Adachi, C. Highly Efficient Organic Light-Emitting Diodes from Delayed Fluorescence. *Nature* **2012**, *492* (7428), 234–238. https://doi.org/10.1038/nature11687.

(200) Tanaka, H.; Shizu, K.; Miyazaki, H.; Adachi, C. Efficient Green Thermally Activated Delayed Fluorescence (TADF) from a Phenoxazine–Triphenyltriazine (PXZ–TRZ) Derivative. *Chemical Communications* **2012**, *48* (93), 11392. https://doi.org/10.1039/c2cc36237f.

(201) Nasu, K.; Nakagawa, T.; Nomura, H.; Lin, C.-J.; Cheng, C.-H.; Tseng, M.-R.; Yasuda, T.; Adachi, C. A Highly Luminescent Spiro-Anthracenone-Based Organic Light-Emitting Diode Exhibiting Thermally Activated Delayed Fluorescence. *Chemical Communications* **2013**, *49* (88), 10385. https://doi.org/10.1039/c3cc44179b.

(202) Endo, A.; Ogasawara, M.; Takahashi, A.; Yokoyama, D.; Kato, Y.; Adachi, C. Thermally Activated Delayed Fluorescence from Sn4+-Porphyrin Complexes and Their Application to Organic Light Emitting Diodes - A Novel Mechanism for Electroluminescence. *Advanced Materials* **2009**, *21* (47), 4802–4806. https://doi.org/10.1002/adma.200900983.

(203) Nakanotani, H.; Masui, K.; Nishide, J.; Shibata, T.; Adachi, C. Promising Operational Stability of High-Efficiency Organic Light-Emitting Diodes Based on Thermally Activated Delayed Fluorescence. *Scientific Reports* **2013**, *3* (Lt 50), 2–6. https://doi.org/10.1038/srep02127.

(204) Nakanotani, H.; Higuchi, T.; Furukawa, T.; Masui, K.; Morimoto, K.; Numata, M.; Tanaka, H.; Sagara, Y.; Yasuda, T.; Adachi, C. High-Efficiency Organic Light-Emitting Diodes with Fluorescent Emitters. *Nature Communications* **2014**, *5* (May), 1–7. https://doi.org/10.1038/ncomms5016.

(205) Furukawa, T.; Nakanotani, H.; Inoue, M.; Adachi, C. Dual Enhancement of Electroluminescence Efficiency and Operational Stability by Rapid Upconversion of Triplet Excitons in OLEDs. *Scientific Reports* **2015**, *5* (1), 8429. https://doi.org/10.1038/srep08429.

(206) Lampande, R.; Kim, G. H.; Im, J. B.; Kim, K. J.; Lee, J. Y.; Kwon, J. H. 45-4: Approach for Attaining Short Exciton Lifetime in Thermally Activated Delayed Fluorescence Emitters. *SID Symposium Digest of Technical Papers* **2017**, *48* (1), 664–667. https://doi.org/10.1002/sdtp.11724.

(207) Yao, L.; Yang, B.; Ma, Y. Progress in Next-Generation Organic Electroluminescent Materials: Material Design beyond Exciton Statistics. *Science China Chemistry* **2014**, *57* (3), 335–345. https://doi.org/10.1007/s11426-013-5046-y.

(208) Baldo, M. A.; Thompson, M. E.; Forrest, S. R. High-Efficiency Fluorescent Organic Light-Emitting Devices Using a Phosphorescent Sensitizer. *Nature* **2000**, *403* (6771), 750–753. https://doi.org/10.1038/35001541.

(209) D'Andrade, B. W.; Baldo, M. A.; Adachi, C.; Brooks, J.; Thompson, M. E.; Forrest, S. R. High-Efficiency Yellow Double-Doped Organic Light-Emitting Devices Based on Phosphor-Sensitized Fluorescence. *Applied Physics Letters* **2001**, *79* (7), 1045–1047. https://doi.org/10.1063/1.1388159.

(210) Lei, G.; Wang, L.; Qiu, Y. Blue Phosphorescent Dye as Sensitizer and Emitter for White Organic Light-Emitting Diodes. *Applied Physics Letters* **2004**, *85* (22), 5403–5405. https://doi.org/10.1063/1.1827326.

(211) Cheng, G.; Zhang, Y.; Zhao, Y.; Liu, S.; Ma, Y. Improved Efficiency for White Organic Light-Emitting Devices Based on Phosphor Sensitized Fluorescence. *Applied Physics Letters* **2006**, *88* (8), 86–89. https://doi.org/10.1063/1.2178478.

(212) Kanno, H.; Sun, Y.; Forrest, S. R. White Organic Light-Emitting Device Based on a Compound Fluorescent-Phosphor-Sensitized-Fluorescent Emission Layer. *Applied Physics Letters* **2006**, *89* (14), 1–4. https://doi.org/10.1063/1.2357038.

(213) Förster, Th. Zwischenmolekulare Energiewanderung und Fluoreszenz. *Annalen der Physik* **1948**, *437* (1–2), 55–75. https://doi.org/10.1002/andp.19484370105.

(214) Kim, H.-G.; Kim, K.-H.; Kim, J.-J. Highly Efficient, Conventional, Fluorescent Organic Light-Emitting Diodes with Extended Lifetime. *Advanced Materials* **2017**, *29* (39), 1702159. https://doi.org/10.1002/adma.201702159.
(215) Heimel, P.; Mondal, A.; May, F.; Kowalsky, W.; Lennartz, C.; Andrienko, D.; Lovrincic, R. Unicolored Phosphor-Sensitized Fluorescence for Efficient and Stable Blue OLEDs. *Nature Communications* **2018**, *9* (1), 4990. https://doi.org/10.1038/s41467-018-07432-2.
(216) Eickhoff, C.; Murer, P.; Geßner, T.; Birnstock, J.; Kröger, M.; Choi, Z.; Watanabe, S.; May, F.; Lennartz, C.; Stengel, I.; Münster, I.; Kahle, K.; Wagenblast, G.; Mangold, H. Long-Lived and Highly Efficient Green and Blue Phosphorescent Emitters and Device Architectures for OLED Displays. In *Organic Light Emitting Materials and Devices XIX*; International Society for Optics and Photonics, 2015; Vol. 9566, p 95662N. https://doi.org/10.1117/12.2199079.
(217) Virgili, T.; Lidzey, D. G.; Bradley, D. D. C. Efficient Energy Transfer from Blue to Red in Tetraphenylporphyrin-Doped Poly (9, 9-Dioctylfluorene) Light-Emitting Diodes. *Advanced Materials* **2000**, *12* (1), 58–62.
(218) Cerullo, G.; Stagira, S.; Zavelani-rossi, M.; Silvestri, D. S.; Virgili, T. Rster Transfer Dynamics in Tetraphenylporphyrin Ultrafast F o. *Chemical Physics Letters* **2001**, *335* (February), 27–33.
(219) Nguyen, C.; Ingram, G.; Lu, Z.-H. Quantifying Interdopant Exciton Processes in Organic Light Emitting Diodes. *The Journal of Physical Chemistry C* **2017**, *121* (6), 3304–3309. https://doi.org/10.1021/acs.jpcc.7b00526.
(220) Förster, Th.; Forster, Th. Transfer Mechanisms of Electronic Excitation Energy. *Radiation Research Supplement* **1960**, *2*, 326. https://doi.org/10.2307/3583604.
(221) Főrster, Th. 10th Spiers Memorial Lecture. Transfer Mechanisms of Electronic Excitation. *Discuss. Faraday Soc.* **1959**, *27* (0), 7–17. https://doi.org/10.1039/DF9592700007.
(222) Jorgensen, W. L.; Tirado-Rives, J. The OPLS Potential Functions for Proteins. Energy Minimizations for Crystals of Cyclic Peptides and Crambin. *Journal of the American Chemical Society* **1988**, *110* (6), 1657–1666. https://doi.org/10.1021/ja00214a001.
(223) Jorgensen, W. L., Tirado-Rives, J. *Abstracts of Papers*; 1998.
(224) Jorgensen, W. L.; Maxwell, D. S.; Tirado-Rives, J. Development and Testing of the OPLS All-Atom Force Field on Conformational Energetics and Properties of Organic Liquids. *Journal of the American Chemical Society* **1996**, *118* (45), 11225–11236. https://doi.org/10.1021/ja9621760.
(225) McDonald, N. A.; Jorgensen, W. L. Development of an All-Atom Force Field for Heterocycles. Properties of Liquid Pyrrole, Furan, Diazoles, and Oxazoles. *The Journal of Physical Chemistry B* **1998**, *102* (41), 8049–8059. https://doi.org/10.1021/jp981200o.
(226) Poelking, C.; Cho, E.; Malafeev, A.; Ivanov, V.; Kremer, K.; Risko, C.; Brédas, J. L.; Andrienko, D. Characterization of Charge-Carrier Transport in Semicrystalline Polymers: Electronic Couplings, Site Energies, and Charge-Carrier Dynamics in Poly(Bithiophene-Alt-Thienothiophene) [PBTTT]. *Journal of Physical Chemistry C* **2013**, *117* (4), 1633–1640. https://doi.org/10.1021/jp311160y.
(227) Breneman, C. M.; Wiberg, K. B. Determining Atom-centered Monopoles from Molecular Electrostatic Potentials. The Need for High Sampling Density in Formamide Conformational Analysis. *Journal of Computational Chemistry* **1990**, *11* (3), 361–373. https://doi.org/10.1002/jcc.540110311.
(228) *Gaussian 16 Revision B.01; 2016*.

(229) Van Der Spoel, D.; Lindahl, E.; Hess, B.; Groenhof, G.; Mark, A. E.; Berendsen, H. J. C. GROMACS: Fast, Flexible, and Free. *Journal of Computational Chemistry* **2005**, *26* (16), 1701–1718. https://doi.org/10.1002/jcc.20291.

(230) Pronk, S.; Páll, S.; Schulz, R.; Larsson, P.; Bjelkmar, P.; Apostolov, R.; Shirts, M. R.; Smith, J. C.; Kasson, P. M.; van der Spoel, D.; Hess, B.; Lindahl, E. GROMACS 4.5: A High-Throughput and Highly Parallel Open Source Molecular Simulation Toolkit. *Bioinformatics* **2013**, *29* (7), 845–854. https://doi.org/10.1093/bioinformatics/btt055.

(231) Singh, S.; Ediger, M. D.; de Pablo, J. J. Ultrastable Glasses from in Silico Vapour Deposition. *Nature Mater* **2013**, *12* (2), 139–144. https://doi.org/10.1038/nmat3521.

(232) Jorgensen, W. L.; Tirado-Rives, J. Potential Energy Functions for Atomic-Level Simulations of Water and Organic and Biomolecular Systems. *Proc Natl Acad Sci USA* **2005**, *102* (19), 6665–6670. https://doi.org/10.1073/pnas.0408037102.

(233) Jorgensen, W. L.; Tirado-Rives, J. The OPLS [Optimized Potentials for Liquid Simulations] Potential Functions for Proteins, Energy Minimizations for Crystals of Cyclic Peptides and Crambin. *J. Am. Chem. Soc.* **1988**, *110* (6), 1657–1666. https://doi.org/10.1021/ja00214a001.

(234) Jorgensen, W. L.; Maxwell, D. S.; Tirado-Rives, J. Development and Testing of the OPLS All-Atom Force Field on Conformational Energetics and Properties of Organic Liquids. *J. Am. Chem. Soc.* **1996**, *118* (45), 11225–11236. https://doi.org/10.1021/ja9621760.

(235) Gallandi, L.; Körzdörfer, T. Long-Range Corrected DFT Meets GW: Vibrationally Resolved Photoelectron Spectra from First Principles. *J. Chem. Theory Comput.* **2015**, *11* (11), 5391–5400. https://doi.org/10.1021/acs.jctc.5b00820.

(236) Frisch, M. J.; Trucks, G. W.; Schlegel, H. B.; Scuseria, G. E.; Robb, M. A.; Cheeseman, J. R.; Scalmani, G.; Barone, V.; Mennucci, B.; al, G. A. P. et. *Gaussian 09 Revision D.01*.

(237) Hess, B.; Kutzner, C.; van der Spoel, D.; Lindahl, E. GROMACS 4: Algorithms for Highly Efficient, Load-Balanced, and Scalable Molecular Simulation. *J. Chem. Theory Comput.* **2008**, *4* (3), 435–447. https://doi.org/10.1021/ct700301q.

(238) Kotadiya, N. B.; Mondal, A.; Xiong, S.; Blom, P. W. M.; Andrienko, D.; Wetzelaer, G. A. H. Rigorous Characterization and Predictive Modeling of Hole Transport in Amorphous Organic Semiconductors. *Adv. Electron. Mater.* **2018**, *4* (12), 1800366. https://doi.org/10.1002/aelm.201800366.

(239) Neumann, T.; Danilov, D.; Lennartz, C.; Wenzel, W. Modeling Disordered Morphologies in Organic Semiconductors. *J. Comput. Chem.* **2013**, *34* (31), 2716–2725. https://doi.org/10.1002/jcc.23445.

(240) Martínez, L.; Andrade, R.; Birgin, E. G.; Martínez, J. M. PACKMOL: A Package for Building Initial Configurations for Molecular Dynamics Simulations. *J. Comput. Chem.* **2009**, *30* (13), 2157–2164. https://doi.org/10.1002/jcc.21224.

(241) Bussi, G.; Donadio, D.; Parrinello, M. Canonical Sampling through Velocity Rescaling. *J. Chem. Phys.* **2007**, *126* (1), 014101. https://doi.org/10.1063/1.2408420.

(242) Valeev, E. F.; Coropceanu, V.; da Silva Filho, D. A.; Salman, S.; Brédas, J.-L. Effect of Electronic Polarization on Charge-Transport Parameters in Molecular Organic Semiconductors. *J. Am. Chem. Soc.* **2006**, *128* (30), 9882–9886. https://doi.org/10.1021/ja061827h.

(243) Tse, S. C.; Kwok, K. C.; So, S. K. Electron Transport in Naphthylamine-Based Organic Compounds. *Applied Physics Letters* **2006**, *89* (26), 262102. https://doi.org/10.1063/1.2420785.

(244) Hill, I. G.; Kahn, A. Organic Semiconductor Heterointerfaces Containing Bathocuproine. *Journal of Applied Physics* **1999**, *86* (8), 4515–4519. https://doi.org/10.1063/1.371395.
(245) Holmes, R. J.; D'Andrade, B. W.; Forrest, S. R.; Ren, X.; Li, J.; Thompson, M. E. Efficient, Deep-Blue Organic Electrophosphorescence by Guest Charge Trapping. *Applied Physics Letters* **2003**, *83* (18), 3818–3820. https://doi.org/10.1063/1.1624639.
(246) White, R. T.; Thibau, E. S.; Lu, Z.-H. Interface Structure of MoO3 on Organic Semiconductors. *Sci Rep* **2016**, *6* (1), 21109. https://doi.org/10.1038/srep21109.
(247) Greiner, M. T.; Helander, M. G.; Tang, W.-M.; Wang, Z.-B.; Qiu, J.; Lu, Z.-H. Universal Energy-Level Alignment of Molecules on Metal Oxides. *Nature Mater* **2012**, *11* (1), 76–81. https://doi.org/10.1038/nmat3159.
(248) Wang, Z. B.; Helander, M. G.; Liu, Z. W.; Greiner, M. T.; Qiu, J.; Lu, Z. H. Controlling Carrier Accumulation and Exciton Formation in Organic Light Emitting Diodes. *Appl. Phys. Lett.* **2010**, *96* (4), 043303. https://doi.org/10.1063/1.3297884.
(249) Salehi, A.; Ho, S.; Chen, Y.; Peng, C.; Yersin, H.; So, F. Highly Efficient Organic Light-Emitting Diode Using A Low Refractive Index Electron Transport Layer. *Advanced Optical Materials* **2017**, *5* (11), 1700197. https://doi.org/10.1002/adom.201700197.
(250) Dänekamp, B.; Droseros, N.; Tsokkou, D.; Brehm, V.; Boix, P. P.; Sessolo, M.; Banerji, N.; Bolink, H. J. Influence of Hole Transport Material Ionization Energy on the Performance of Perovskite Solar Cells. *Journal of Materials Chemistry C* **2019**, *7* (3), 523–527. https://doi.org/10.1039/C8TC05372C.
(251) Poelking, C.; Andrienko, D. Long-Range Embedding of Molecular Ions and Excitations in a Polarizable Molecular Environment. *J. Chem. Theory Comput.* **2016**, *12* (9), 4516–4523. https://doi.org/10.1021/acs.jctc.6b00599.
(252) Pasveer, W. F.; Cottaar, J.; Tanase, C.; Coehoorn, R.; Bobbert, P. A.; Blom, P. W. M.; de Leeuw, D. M.; Michels, M. A. J. Unified Description of Charge-Carrier Mobilities in Disordered Semiconducting Polymers. *Phys. Rev. Lett.* **2005**, *94* (20), 206601. https://doi.org/10.1103/PhysRevLett.94.206601.
(253) Schrader, M.; Fitzner, R.; Hein, M.; Elschner, C.; Baumeier, B.; Leo, K.; Riede, M.; Bäuerle, P.; Andrienko, D. Comparative Study of Microscopic Charge Dynamics in Crystalline Acceptor-Substituted Oligothiophenes. *J. Am. Chem. Soc.* **2012**, *134* (13), 6052–6056. https://doi.org/10.1021/ja300851q.
(254) Kadashchuk, A.; Weiss, D. S.; Borsenberger, P. M.; Nešpùrek, S.; Ostapenko, N.; Zaika, V. The Origin of Thermally Stimulated Luminescence in Neat and Molecularly Doped Charge Transport Polymer Systems. *Chemical Physics* **1999**, *247* (2), 307–319. https://doi.org/10.1016/S0301-0104(99)00169-X.
(255) Kadashchuk, A.; Skryshevski, Yu.; Piryatinski, Yu.; Vakhnin, A.; Emelianova, E. V.; Arkhipov, V. I.; Bässler, H.; Shinar, J. Thermally Stimulated Photoluminescence in Poly(2,5-Dioctoxy *p* -Phenylene Vinylene). *Journal of Applied Physics* **2002**, *91* (8), 5016–5023. https://doi.org/10.1063/1.1464235.
(256) Kadashchuk, A.; Skryshevskii, Yu.; Vakhnin, A.; Ostapenko, N.; Arkhipov, V. I.; Emelianova, E. V.; Bässler, H. Thermally Stimulated Photoluminescence in Disordered Organic Materials. *Phys. Rev. B* **2001**, *63* (11), 115205. https://doi.org/10.1103/PhysRevB.63.115205.
(257) Arkhipov, V. I.; Emelianova, E. V.; Kadashchuk, A.; Bässler, H. Hopping Model of Thermally Stimulated Photoluminescence in Disordered Organic Materials. *Chemical Physics* **2001**, *266* (1), 97–108. https://doi.org/10.1016/S0301-0104(01)00332-9.

(258) Patil, S. A.; Scherf, U.; Kadashchuk, A. New Conjugated Ladder Polymer Containing Carbazole Moieties. *Adv. Funct. Mater.* **2003**, *13* (8), 609–614. https://doi.org/10.1002/adfm.200304344.

(259) Fakharuddin, A.; Qiu, W.; Croes, G.; Devižis, A.; Gegevičius, R.; Vakhnin, A.; Rolin, C.; Genoe, J.; Gehlhaar, R.; Kadashchuk, A.; Gulbinas, V.; Heremans, P. Reduced Efficiency Roll-Off and Improved Stability of Mixed 2D/3D Perovskite Light Emitting Diodes by Balancing Charge Injection. *Adv. Funct. Mater.* **2019**, *29* (37), 1904101. https://doi.org/10.1002/adfm.201904101.

(260) Stankevych, A.; Andrienko, D.; Paterson, L.; Genoe, J.; Fishchuk, I. I.; Bässler, H.; Köhler, A.; Kadashchuk, A. Density of States of OLED Hosts from Thermally Stimulated Luminescence. *Phys. Rev. Appl.* **2020**.

(261) Fishchuk, I. I.; Kadashchuk, A. K.; Bassler, H.; Weiss, D. S. Nondispersive Charge-Carrier Transport in Disordered Organic Materials Containing Traps. *PHYSICAL REVIEW B* **2002**, *66* (20), 205208. https://doi.org/10.1103/PhysRevB.66.205208.

(262) Matsusue, N.; Suzuki, Y.; Naito, H. Charge Carrier Transport in Neat Thin Films of Phosphorescent Iridium Complexes. *Jpn. J. Appl. Phys.* **2005**, *44* (6A), 3691–3694. https://doi.org/10.1143/JJAP.44.3691.

(263) Wu, M.-F.; Yeh, S.-J.; Chen, C.-T.; Murayama, H.; Tsuboi, T.; Li, W.-S.; Chao, I.; Liu, S.-W.; Wang, J.-K. The Quest for High-Performance Host Materials for Electrophosphorescent Blue Dopants. *Advanced Functional Materials* **2007**, *17* (12), 1887–1895. https://doi.org/10.1002/adfm.200600800.

(264) Tse, S. C.; Tsang, S. W.; So, S. K. Nearly Ohmic Injection Contacts from PEDOT:PSS to Phenylamine Compounds with High Ionization Potentials; Kafafi, Z. H., So, F., Eds.; San Diego, California, USA, 2006; p 63331P. https://doi.org/10.1117/12.682442.

(265) Naka, S.; Okada, H.; Onnagawa, H.; Tsutsui, T. High Electron Mobility in Bathophenanthroline. *Applied Physics Letters* **2000**, *76* (2), 197–199. https://doi.org/10.1063/1.125701.

(266) Chu, X. B.; Guan, M.; Niu, L. T.; Zhang, Y.; Li, Y. Y.; Liu, X. F.; Zeng, Y. P. The Utilization of Low-Temperature Evaporable CsN_3-Doped NBphen as an Alternative and Efficient Electron-Injection Layer in OLED: CsN_3 Doped NBphen as an Alternative Electron-Injection Layer in OLED. *physica status solidi (a)* **2014**, *211* (7), 1605–1609. https://doi.org/10.1002/pssa.201431090.

(267) Saragi, T. P. I.; Spehr, T.; Siebert, A.; Fuhrmann-Lieker, T.; Salbeck, J. Spiro Compounds for Organic Optoelectronics. *Chemical Reviews* **2007**, *107* (4), 1011–1065. https://doi.org/10.1021/cr0501341.

(268) Noh, S.; Suman, C. K.; Hong, Y.; Lee, C. Carrier Conduction Mechanism for Phosphorescent Material Doped Organic Semiconductor. *Journal of Applied Physics* **2009**, *105* (3), 033709. https://doi.org/10.1063/1.3072693.

(269) Kang, J.-W.; Lee, S.-H.; Park, H.-D.; Jeong, W.-I.; Yoo, K.-M.; Park, Y.-S.; Kim, J.-J. Low *Roll-off* of Efficiency at High Current Density in Phosphorescent Organic Light Emitting Diodes. *Applied Physics Letters* **2007**, *90* (22), 223508. https://doi.org/10.1063/1.2745224.

(270) Chen, H.-F.; Yang, S.-J.; Tsai, Z.-H.; Hung, W.-Y.; Wang, T.-C.; Wong, K.-T. 1,3,5-Triazine Derivatives as New Electron Transport–Type Host Materials for Highly Efficient Green Phosphorescent OLEDs. *Journal of Materials Chemistry* **2009**, *19* (43), 8112. https://doi.org/10.1039/b913423a.

(271) Rhee, S. H.; Nam, K. b.; Kim, C. S.; Song, M.; Cho, W.; Jin, S.-H.; Ryu, S. Y. Effect of Electron Mobility of the Electron Transport Layer on Fluorescent Organic Light-Emitting Diodes. *ECS Solid State Letters* **2014**, *3* (5), R19–R22. https://doi.org/10.1149/2.011404ssl.

(272) Hung, W.-Y.; Ke, T.-H.; Lin, Y.-T.; Wu, C.-C.; Hung, T.-H.; Chao, T.-C.; Wong, K.-T.; Wu, C.-I. Employing Ambipolar Oligofluorene as the Charge-Generation Layer in Time-of-Flight Mobility Measurements of Organic Thin Films. *Applied Physics Letters* **2006**, *88* (6), 064102. https://doi.org/10.1063/1.2172708.

(273) Faber, C.; Boulanger, P.; Attaccalite, C.; Duchemin, I.; Blase, X. Excited States Properties of Organic Molecules: From Density Functional Theory to the *GW* and Bethe–Salpeter Green's Function Formalisms. *Phil. Trans. R. Soc. A* **2014**, *372* (2011), 20130271. https://doi.org/10.1098/rsta.2013.0271.

(274) Hedin, L.; Lundqvist, S. Effects of Electron-Electron and Electron-Phonon Interactions on the One-Electron States of Solids. *Solid State Physics 23*, 1–181. https://doi.org/10.1016/S0081-1947(08)60615-3.

(275) Bagheri, B.; Baumeier, B.; Karttunen, M. Getting Excited: Challenges in Quantum-Classical Studies of Excitons in Polymeric Systems. *Phys. Chem. Chem. Phys.* **2016**, *18* (44), 30297–30304. https://doi.org/10.1039/C6CP02944B.

(276) Jin, Y.; Yang, W. Excitation Energies from the Single-Particle Green's Function with the *GW* Approximation. *J. Phys. Chem. A* **2019**, *123* (14), 3199–3204. https://doi.org/10.1021/acs.jpca.9b02379.

(277) Stehr, V.; Fink, R. F.; Engels, B.; Pflaum, J.; Deibel, C. Singlet Exciton Diffusion in Organic Crystals Based on Marcus Transfer Rates. *J. Chem. Theory Comput.* **2014**, *10* (3), 1242–1255. https://doi.org/10.1021/ct500014h.

(278) Casalegno, M.; Raos, G.; Po, R. Methodological Assessment of Kinetic Monte Carlo Simulations of Organic Photovoltaic Devices: The Treatment of Electrostatic Interactions. *The Journal of Chemical Physics* **2010**, *132* (9), 094705. https://doi.org/10.1063/1.3337909.

(279) Tyagi, S.; Arnold, A.; Holm, C. ICMMM2D: An Accurate Method to Include Planar Dielectric Interfaces via Image Charge Summation. *The Journal of Chemical Physics* **2007**, *127* (15), 154723. https://doi.org/10.1063/1.2790428.

(280) Tyagi, S.; Arnold, A.; Holm, C. Electrostatic Layer Correction with Image Charges: A Linear Scaling Method to Treat Slab 2D+h Systems with Dielectric Interfaces. *The Journal of Chemical Physics* **2008**, *129* (20), 204102. https://doi.org/10.1063/1.3021064.

(281) Arnold, A.; Holm, C. MMM2D: A Fast and Accurate Summation Method for Electrostatic Interactions in 2D Slab Geometries. *Computer Physics Communications* **2002**, *148* (3), 327–348. https://doi.org/10.1016/S0010-4655(02)00586-6.

(282) Sperb, R. An Alternative to Ewald Sums Part I: Identities for Sums. *Molecular Simulation* **1998**, *20* (3), 179–200. https://doi.org/10.1080/08927029808024176.

(283) Ballenegger, V.; Arnold, A.; Cerdà, J. J. Simulations of Non-Neutral Slab Systems with Long-Range Electrostatic Interactions in Two-Dimensional Periodic Boundary Conditions. *J. Chem. Phys.* **2009**, *131* (9), 094107. https://doi.org/10.1063/1.3216473.

(284) Saunders, W. R.; Grant, J.; Müller, E. H.; Thompson, I. Fast Electrostatic Solvers for Kinetic Monte Carlo Simulations. *Journal of Computational Physics* **2020**, *410*, 109379. https://doi.org/10.1016/j.jcp.2020.109379.

(285) Pippig, M.; Mercuri, F. Efficient Evaluation of Coulomb Interactions in Kinetic Monte Carlo Simulations of Charge Transport. *J. Chem. Phys.* **2020**, *152* (16), 164102. https://doi.org/10.1063/5.0003258.

(286) Bereau, T.; Andrienko, D.; Kremer, K. Research Update: Computational Materials Discovery in Soft Matter. *APL Mater.* **2016**, *4* (5), 053101. https://doi.org/10.1063/1.4943287.

(287) Bereau, T.; Andrienko, D.; von Lilienfeld, O. A. Transferable Atomic Multipole Machine Learning Models for Small Organic Molecules. *J. Chem. Theory Comput.* **2015**, *11* (7), 3225–3233. https://doi.org/10.1021/acs.jctc.5b00301.

(288) Scherer, C.; Scheid, R.; Andrienko, D.; Bereau, T. Kernel-Based Machine Learning for Efficient Simulations of Molecular Liquids. *J. Chem. Theory Comput.* **2020**, *16* (5), 3194–3204. https://doi.org/10.1021/acs.jctc.9b01256.

(289) Yin, S.; Shuai, Z.; Wang, Y. A Quantitative Structure−Property Relationship Study of the Glass Transition Temperature of OLED Materials. *J. Chem. Inf. Comput. Sci.* **2003**, *43* (3), 970–977. https://doi.org/10.1021/ci034011y.

(290) Xu, J.; Chen, B. Prediction of Glass Transition Temperatures of OLED Materials Using Topological Indices. *J Mol Model* **2005**, *12* (1), 24–33. https://doi.org/10.1007/s00894-005-0282-5.

List of included figures

List of included tables